공학석사 학위논문

Extension of the Component Thermal-Hydraulics Analysis code CUPID toward Sub-channel Scale Analysis of PWR Reactor Core

가압경수로 전 노심 부수로 스케일 해석을 위한 열수력 기기해석코드 CUPID 확장

2017년 2월

서울대학교 대학원
에너지시스템공학부
윤 석 중

Abstract

Extension of the Component Thermal-Hydraulics Analysis code CUPID toward Sub-channel Scale Analysis of PWR Reactor Core

Seok-Jong Yoon
Department of Energy System Engineering
The Graduate School
Seoul National University

In order to improve margin management, meet new safety requirements and secure operational flexibility, it is required to apply the latest codes and methods for safety demonstration. In this context, high-fidelity and multi-physics simulation for a full core of a light water reactor with coupled T/H (Thermal-Hydraulics) and neutronics code under steady and transient conditions become a critical issue in the nuclear reactor safety analysis. Considering the computational power necessary for a full core pin-by-pin analysis, a subchannel scale T/H analysis is desired to achieve required accuracy with an endurable computational time. In this study, KAERI (Korea Atomic Energy Research Institute)'s inhouse code CUPID was applied for the subchannel scale T/H analysis for PWR reactor core. The code adopts three-dimensional two-fluid model with various closure models and incorporates a highly parallelized numerical solver. These features of CUPID would be advantageous to extend its applicability for simulation of

accident condition with full core pin-by-pin modeling.

In this paper, implemented models required for a subchannel scale T/H analysis are introduced and the code validation results against various flow conditions are presented. Thereafter, preliminary calculation of simplified OPR1000 reactor core is conducted. From these calculation results, full core simulation capability and performance of parallel solver are evaluated. Finally, subchannel scale analysis for the APR1400 reactor core at cycle 1 hot full power steady state is performed. Specific geometry features of APR1400 including fuel assembly, water gap, shroud and guide tube are considered in the presented demonstration. Whole core pin power distributions from the calculation result of neutronics code nTRACER are applied to CUPID for high fidelity full core T/H simulation. Following the demonstration results, coolant temperature and velocity distributions are properly simulated with CUPID. Thereafter, MDNBR (Minimum Departure from Nucleate Boiling Ratio) analysis capability of CUPID using Biasi correlation is demonstrated.

From this work, CUPID shows its capability of reproducing key phenomena in a reactor core and dealing with subchannel scale whole core T/H analysis.

……...

Keywords: Subchannel scale T/H analysis, Reactor core T/H analysis, CUPID, Validation, APR1400

Student Number: 2015-21325

List of Contents

List of Tables

List of Figures

Chapter 1.

Introduction

1.1 Background

Recently, high-fidelity and multi-physics simulation for a full core of a light water reactor including T/H (Thermal-Hydraulics), neutronics and fuel performance analysis codes become a critical issue to analyze the nuclear fuel behavior more accurately under accident condition such as reactivity induced accident. The coolant temperature and density which affect the neutron behavior are important parameters for nuclear reactor safety analysis. The parameters of T/H and neutronics affect each other to thermal-feedback at both steady and transient analysis for reactor core.

So, it is important to obtain T/H and neutronics information locally at near fuel rod and guide tube for high-fidelity and multi-physics simulation under reactivity induced accident conditions.

The methodologies of the nuclear reactor safety analysis have been developed with the advancement of computing power. High performance computing powers and advanced numerical algorithms allow the coupled multi-physics analysis and 3D full core transient simulation. Coupled 3D analysis methods are the most suitable tools for transient analysis under asymmetric power distribution condition. These methods can assure higher safety margin. Also, these methods can minimize

economic uncertainty by optimizing fuel design and fuel cycle costs (Albin et al., 2012).

Considering the computational power necessary for a full core pin-by-pin analysis, a subchannel scale T/H analysis is desired to achieve required accuracy of the simulation with an endurable computational time. Subchannel means imaginary flow area surrounded by fuel rods as illustrated in Fig. 1.1. In the scale of the analysis, one computational cell represents a subchannel in a horizontal cross cut of the reactor core.

1.2 Literature Reviews

Nowadays, various subchannel analysis codes have been developed and used for reactor core design and evaluation of the safety margin. The previous research activities of subchannel scale analysis for reactor core are presented in this section.

CTF

CTF code originally developed by Pacific Northwest Laboratory and modified by Pennsylvania State University has been used at CASL (Consortium for Advanced Simulation of Light water reactors) project (Blyth, 2014) and NURESAFE (NUclear REactor SAFEty simulation platform) project (Jimenez et al., 2014) for high precision full core subchannel T/H analysis with coupling multiple codes. In CASL project, coupled with neutronics code and chemistry code, CTF code was used for high fidelity full core T/H analysis in accident conditions. Recently, loss-of-flow transient in a 4-loop Westinghouse core was

simulated with coupling CTF code (T/H code) and MPACT code (neutronics code) as shown in Fig. 1.2 (Salko et al., 2015). Also, MSLB (Main Steam Line Break) accident at the HZP (Hot Zero Power) condition was analyzed as shown in Fig. 1.3 with coupled multi-physics approach using CTF and neutronics code (CASL S&T, 2015). In both simulations, information of calculated parameters from CTF code and neutronics code were exchanged each other.

In NURESAFE project, CTF code was used for maintaining high safety standards under normal operation and design basis accident conditions of LWR with coupling pin-by-pin diffusion code COBAYA3 (Jiménez et al., 2009).

COBRA-FLX

COBRA-FLX code which is originally developed by Pacific Northwest Laboratory and modified by AREVA is based on drift flux model (AREVA, 2010). COBRA-FLX code was used for the analysis of space-time effect in PWR coupled with neutronics code at AREVA's reactor dynamics program, PANBOX (Böer et al., 1992). To study local effect at rod ejection accident in PWR, the hot channel analysis was performed using COBRA-FLX. Specifically, DNBR and the location of film boiling were simulated to obtain the high safety margin at PWR (Albin et al., 2012).

Recently, COBRA-FLX code has been used at AREVA's new code system, ARCADIA, for efficient, flexible core design and reliable operation of PWR (AREVA, 2010). The ARCADIA system covers numerous engineering activities from nuclear fuel assembly design to safety analyses. The ARCADIA system consists of the core simulator code, ARTEMIX, core subchannel T/H code, COBRA-FLX and the fuel performance code, GALILEO. Following these

features, ARCADIA system has ability to optimize gadolinia loadings for saving fuel cycle cost.

SUBCHANFLOW

SUBCHANFLOW is an inhouse subchannel T/H analysis code developed by KIT (Karlsruhe Institute of Technology) based on COBRA-IV-I (Wheeler et al., 1976) and COBRA-EN code (Basile et al., 2001). SUBCHANFLOW code has been used at multi-physics homogeneous pin-by-pin reactor simulator, DYNSUB (Sanchez et al., 2010). In DYNSUB simulator, SUBCHANFLOW had been coupled with 3D neutron kinetics code DYN3D (developed by Helmholtz Zentrum Dresden Rossendorf) for providing a cost effective improved description of LWR core behavior at static and transient safety relevant scenarios. Rod ejection scenario at hot zero power condition was analyzed by DYNSUB simulator as shown in Fig. 1.5 (Daeubler et al., 2014).

MATRA

In Korea, subchannel scale T/H analysis code MATRA, which is descended from the COBRA code has been developed by KAERI (Korea Atomic Energy Research Institute) and used widely for reactor core design and evaluating DNBR margin (Hwang et al., 2008). Recently, its numerical solver was improved by adopting parallelization algorithm for an efficient full core pin-by-pin simulation (Kim et al., 2014). MATRA code adopts the HEM (Homogeneous Equilibrium Model) and spatial marching scheme which result in the significant reduction of the computational burden. The code was coupled with neutronics code nTRACER

for high fidelity hot full power state of OPR1000 reactor core analysis as presented in Fig. 1.6 (Jung et al., 2013).

However, these code features are not optimized for accident analyses, for example, the HEM for the two-phase flow and spatial marching scheme to solve the governing equations. The MATRA code adopts the slip model, but it is desired to employ a better model like two-fluid model for high precision simulation involving considerable boiling condition. In case of using spatial marching scheme, it solves the governing equations at a certain plane, and the obtained values will be used as boundary conditions at the upper plane. If there occurs a reverse flow, the boundary conditions for next plane cannot be defined, so there exists limitation of solving reverse flow with spatial marching scheme. Therefore, improved models and numerical solver are required for simulating accident conditions, such as reverse flow and considerable boiling two-phase flow conditions.

1.3 Objective of Study and Scope

In this study, a feasibility test was conducted aiming to show the applicability of the KAERI's inhouse code CUPID for the subchannel scale full core T/H analysis. CUPID is a component scale T/H analysis code devoted to the high fidelity analysis for nuclear reactor component. It adopts three-dimensional two-fluid model with various closure models. It uses collocated mesh and semi-implicit ICE (Implicit Continuous Eulerian) method for numerical scheme (KAERI, 2014). Numerical solver for CUPID was highly parallelized with Message Passing Interface (MPI) domain decomposition method and its performance was tested with various two-phase problems. These features of

CUPID would be advantageous to extend its applicability for simulation of an accident condition with full core pin-by-pin modeling.

It is possible to perform multiscale analysis using CUPID for the primary side of nuclear power plant. A simulation of the coolant mixing was conducted by Park et al using the coupled MARS and CUPID (Park et al., 2012). Following the simulation results, system scale T/H analysis code MARS could be utilized for analyzing the primary side. In the case of T/H analysis at the reactor vessel downcomer and lower plenum, CUPID could be utilized for CFD scale analysis. Recently, CFD scale analysis using CUPID for downcomer and lower plenum were conducted by Cho et al (2016) with ROCOM simulation. Also, in the case of reactor core, CUPID could be utilized for subchannel scale T/H analysis.

Following these features, CUPID is considered as an eligible tool with its flexibility and applicability on reactor core T/H simulation. Also, CUPID uses non-staggered mesh, and it can handle for any type of core geometries like triangular or hexagonal shape of subchannel.

Some previous studies were performed for the reactor core T/H analysis using CUPID. By Cho et al. (2013), CFD scale analysis for open medium model was performed as shown in Fig. 1.7. Also, assembly scale analysis for simulating rod ejection accident with coupling CUPID and MASTER code was performed as presented in Fig. 1.8 (Lee et al., 2010).

The objective of this study is to extend CUPID's capability for high fidelity T/H simulation of subchannel scale reactor core. In this work, implemented models required for subchannel scale T/H analysis are introduced. Thereafter, the validation results of the CUPID code against rod bundle flow mixing experiments under various flow conditions are presented. And then, subchannel scale analysis

result for the APR1400 reactor core at cycle 1 hot full power steady state is demonstrated.

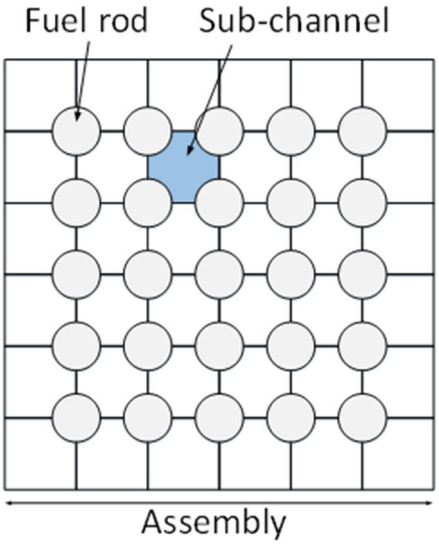

Figure 1.1 Schematic view of subchannel in one assembly

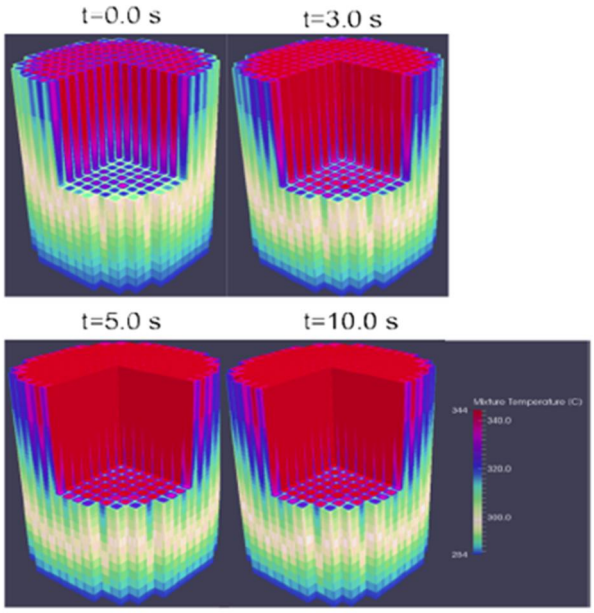

Figure 1.2 Coolant temperature distribution during LOF transient using CTF (CASL, 2015)

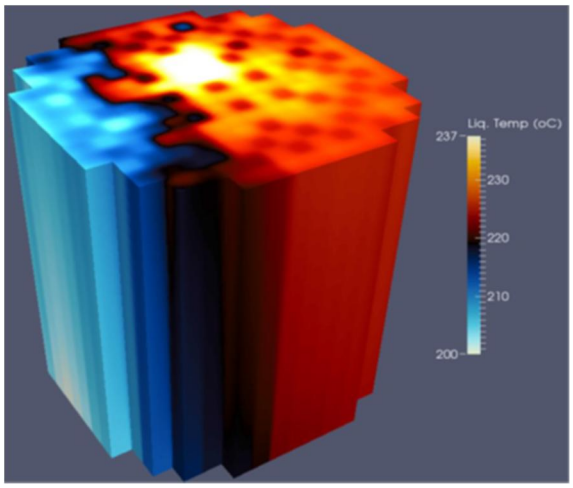

Figure 1.3 Coolant temperature distribution at MSLB accident using CTF (CASL, 2015)

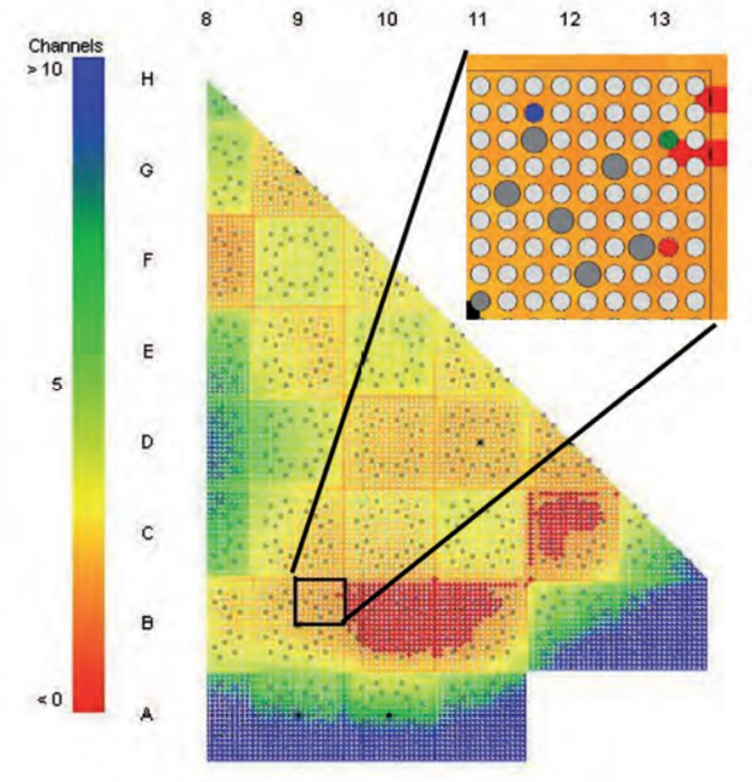

Figure 1.4 DNBR analysis using COBRA-FLX (Red color indicate film boiling) (Albin et al., 2012)

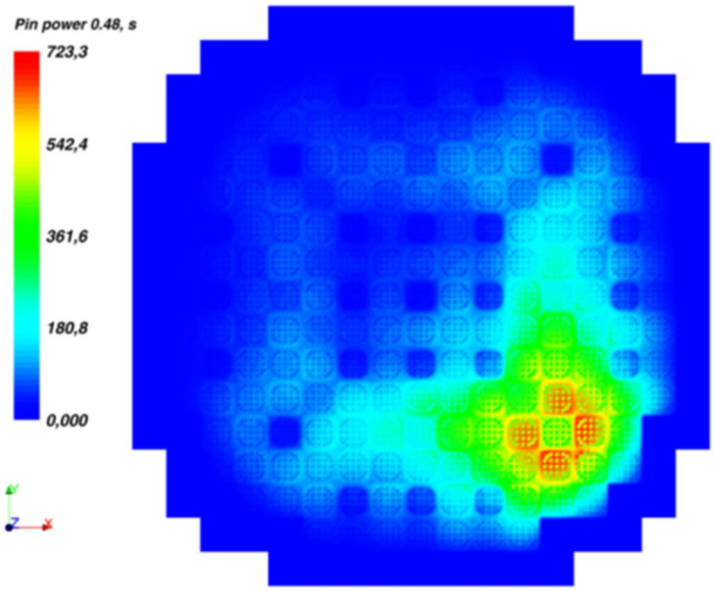

Figure 1.5 Axially cumulated power density distribution computed by DYNSUB (Daeubler et al., 2014)

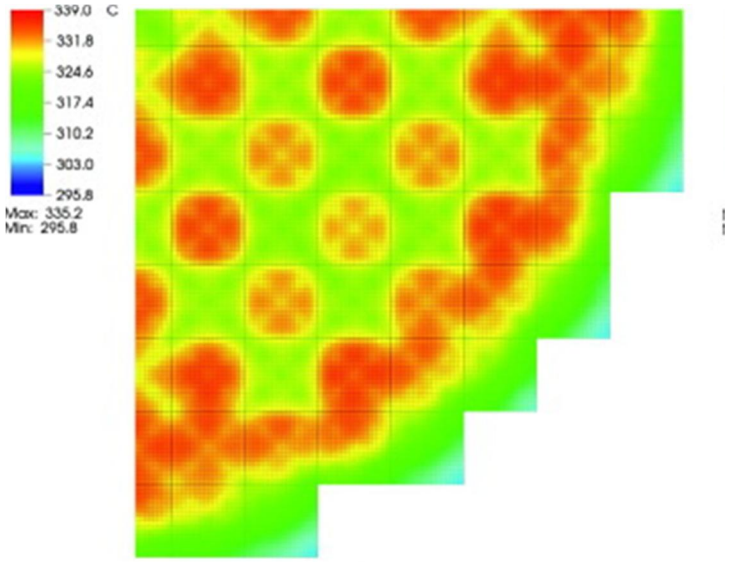

Figure 1.6 Coolant temperature distribution with coupling MATRA/nTRACER (Jung et al., 2013)

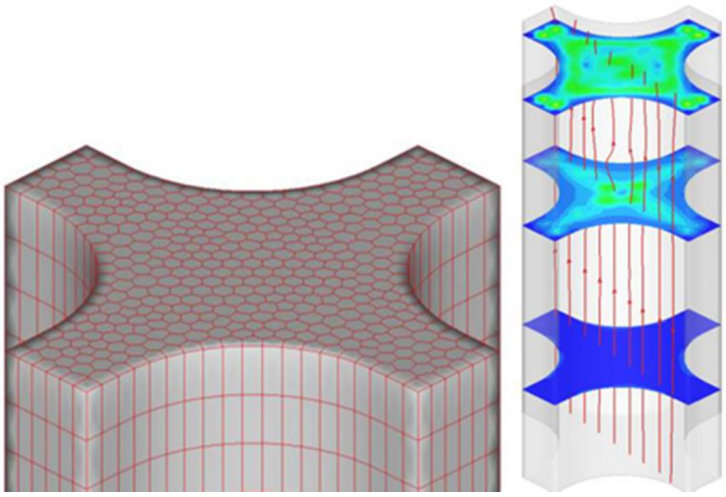

Figure 1.7 CFD scale analysis for open medium model using CUPID
(Cho et al., 2013)

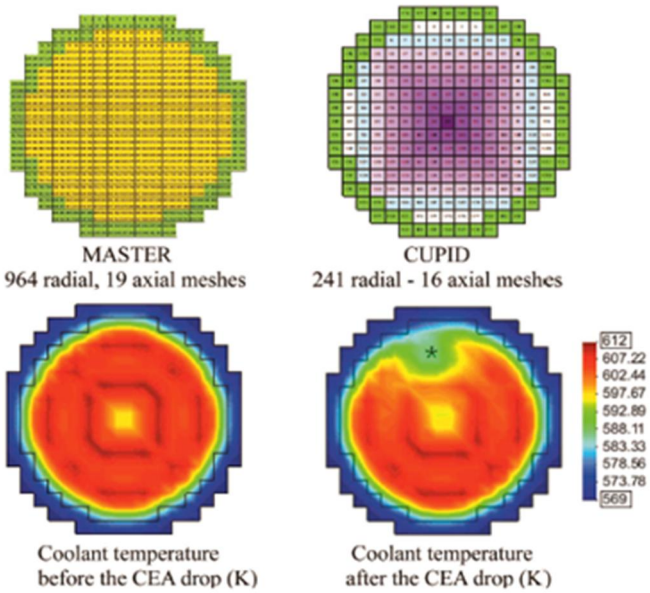

Figure 1.8 Assembly scale analysis for CUPID-MASTER code coupling
(Lee et al., 2010)

Chapter 2.

Implementation of Subchannel T/H Models to CUPID

2.1 Governing Equations

The CUPID code adopts a transient three-dimensional two-fluid models for the analysis of two-phase flows. The two fluid means vapor and liquid. The use of two-fluid model is useful in describing high precision simulation for two-phase flows which could occur at accident conditions.

Porous media approach was used for describing flow field in the reactor core considering fuel rods. Geometries of fuel rods are simplified with a given porosity in control volumes (Fig. 2.1 and Fig. 2.2). Convection and diffusion at each cell face are considered with permeability.

In this chapter, governing equations which use porous media model and two fluid model are presented. When discretizing the governing equations, the Finite Volume Method (FVM) is applied within the control volumes. Porosity and permeability are considered at the volume and surface integral by the FVM, respectively.

Mass conservation equation

$$\int \frac{\partial}{\partial t}(\alpha_k \rho_k) dV + \int \alpha_k \rho_k \overrightarrow{V_k} \cdot d\vec{S} = \int \Gamma_k \, dV + \int \vec{M}_e^T \, dV \quad (2\text{-}1)$$

Here, the subscript k denotes phase. With applying the FVM method to discretize the equation, each parameter is discretized as follows:

$$\int \frac{\partial}{\partial t}(\alpha_k \rho_k) dV = (\alpha_k \delta \rho_k + \rho_k \delta \alpha_k) \gamma V \delta t^{-1} \quad (2\text{-}2)$$

$$\int \alpha_k \rho_k \overrightarrow{V_k}^{n+1} \cdot d\vec{S} = \sum_f \left(\alpha_k \rho_k \overrightarrow{V_k}^{n+1} \right)_f \cdot \overrightarrow{\varepsilon S} \quad (2\text{-}3)$$

where, γ: Porosity, Fraction of fluid volume in the material

ε: Permeability, Fraction of fluid area in the material

Γ_k: Volumetric mass transfer rate

$\vec{M}_e^T$: Mass exchange due to turbulent mixing and void drift

$$\int \Gamma_k \, dV = \Gamma_k \gamma V \quad (2\text{-}4)$$

$$\int \vec{M}_e^T \, dV = \vec{M}_e^T \gamma V \quad (2\text{-}5)$$

Momentum conservation equation

$$\int \frac{\partial}{\partial t}\left(\alpha_k \rho_k \overrightarrow{V_k}\right) dV + \int (\alpha_k \rho_k \overrightarrow{V_k} \overrightarrow{V_k}) \cdot d\vec{S} - \overrightarrow{V_k} \int (\alpha_k \rho_k \overrightarrow{V_k}) \cdot d\vec{S}$$
$$= -\int \alpha_k \nabla P dV + \int \alpha_k \rho_k \vec{g} dV - \int \left(\alpha_k \mu_k \nabla \overrightarrow{V_k}\right) \cdot d\vec{S}$$
$$+ \int S_k dV + \int \vec{M}_{wk} \, dV + \int \vec{M}_k^T \, dV \quad (2\text{-}6)$$

Here, $\overrightarrow{V_k}$ means vector velocity $\left(u_k \vec{\imath} + v_k \vec{\jmath} + w_k \vec{k}\right)$ which considers x, y and z direction at Cartesian coordinate system. Following the definition of vector velocity, momentum conservation equation has three different types considering x, y and z direction. In RHS, S_k indicates momentum source or sink term due to phase change, $\vec{M}_{wk}$ indicates friction factor and form loss and $\vec{M}_k^T$ means

momentum transfer due to the turbulent mixing and void drift. Then, the discretized form of each parameter in momentum conservation equation is given as:

$$\int \frac{\partial}{\partial t}\left(\alpha_k \rho_k \overrightarrow{V_k}\right) dV = \alpha_k \rho_k \left(\overrightarrow{V_k}^{n+1} - \overrightarrow{V_k}^{n}\right) \gamma V \delta t^{-1} \quad (2\text{-}7)$$

$$\int \left(\alpha_k \rho_k \overrightarrow{V_k}\overrightarrow{V_k}\right) \cdot d\vec{S} = \sum_f \left(\alpha_k \rho_k \overrightarrow{V_k}\overrightarrow{V_k}\right)_f \cdot \overrightarrow{\varepsilon S} \quad (2\text{-}8)$$

$$\overrightarrow{V_k} \int \left(\alpha_k \rho_k \overrightarrow{V_k}\right) d\vec{S} = \overrightarrow{V_k} \sum_f \left(\alpha_k \rho_k \overrightarrow{V_k}\right)_f \cdot \overrightarrow{\varepsilon S} \quad (2\text{-}9)$$

$$\int \alpha_k \nabla P dV = \alpha_k \nabla P^{n+1} \gamma V \quad (2\text{-}10)$$

$$\int \alpha_k \rho_k \vec{g} dV = \alpha_k \rho_k \vec{g} \gamma V \quad (2\text{-}11)$$

$$\int \left(\alpha_k \mu_k \nabla \overrightarrow{V_k}\right) \cdot d\vec{S} = \sum_f (\alpha_k \mu_k)_f \frac{\overrightarrow{V_{k,J}} - \overrightarrow{V_{k,\iota}}}{d_{hy}} \cdot \overrightarrow{\varepsilon S} \quad (2\text{-}12)$$

$$\int S_k dV = S_k \gamma V \quad (2\text{-}13)$$

$$\int \vec{M}_{wk}\, dV = \vec{M}_{wk} \gamma V \quad (2\text{-}14)$$

$$\int \vec{M}_k^T\, dV = \vec{M}_k^T\, \gamma V \quad (2\text{-}15)$$

Energy conservation equation

$$\int \frac{\partial}{\partial t} (\alpha_k \rho_k e_k)\, dV + \int \left(\alpha_k \rho_k e_k \overrightarrow{V_k}\right) \cdot d\vec{S}$$

$$= -\int P \frac{\partial \alpha_k}{\partial t} dV - P \int \alpha_k \overrightarrow{V_k} \cdot d\vec{S} + \int \alpha_k k_k \nabla T_k \cdot d\vec{S} + \int E_k dV + \int \vec{M}_h^T\, dV$$

$$+ \int q''_{fluid-solid}\, dA + q''_{fluid-porous} A_{fluid-porous} \quad (2\text{-}16)$$

where, E_k: Energy source or sink term due to phase change, interfacial heat transfer and volumetric heat generation

$\vec{M}_h^T$: Energy exchange due to turbulent mixing and void drift

$q''_{fluid-porous} = h_{fluid-porous}\left(T_{porous} - T_{fluid}\right)$

$h_{fluid-porous}$: Heat transfer coefficient between fluid and conductor in

porous medium

$A_{fluid-porous}$: Heat transfer area between fluid and conductor in porous medium

$q''_{fluid-solid}$: Heat transfer rate between fluid and neighboring conductor in porous medium

The discretized form of each parameter in energy conservation equation can be derived as follows:

$$\int \frac{\partial}{\partial t}(\alpha_k \rho_k e_k)\, dV = \left(\rho_g e_g \delta\alpha_g + \delta\rho_g e_g \alpha_g + \rho_g \delta e_g \alpha_g\right)\gamma V \delta t^{-1} \quad (2\text{-}17)$$

$$\int \left(\alpha_k \rho_k e_k \overrightarrow{V_k}\right) \cdot d\vec{S} = \sum_f \left(\alpha_k \rho_k e_k \overrightarrow{V_k}\right)_f \cdot \overrightarrow{\varepsilon S} \quad (2\text{-}18)$$

$$\int P \frac{\partial \alpha_k}{\partial t} dV = P \delta \alpha_k \gamma V \delta t^{-1} \quad (2\text{-}19)$$

$$P \int \alpha_k \overrightarrow{V_k} \cdot d\vec{S} = P \sum_f \left(\alpha_k \overrightarrow{V_k}\right)_f \cdot \overrightarrow{\varepsilon S} \quad (2\text{-}20)$$

$$\int \alpha_k k_k \nabla T_k \cdot d\vec{S} = \sum_f (\alpha_k k_k)_f \left(\frac{T_{k,j} - T_{k,i}}{d_{hy}}\right) \cdot \overrightarrow{\varepsilon S} \quad (2\text{-}21)$$

$$\int E_k dV = E_k \gamma V \quad (2\text{-}22)$$

$$\int \vec{M}_h^T \, dV = \vec{M}_h^T \gamma V \quad (2\text{-}23)$$

$$\int q''_{fluid-solid} \, dA = \sum_f \left(q''_{fluid-solid}\right)_f \cdot \overrightarrow{\varepsilon S} \quad (2\text{-}24)$$

2.2 Subchannel T/H Models

The fluid transfer between adjacent subchannels can be explained by three mechanisms, i.e. cross flow, turbulent mixing and void drift (Lahey et al., 1993). These mechanisms are modeled as a closure terms to solve the mass, momentum

and energy conservation equations. These subchannel T/H models contribute mass, momentum and energy transfer between adjacent subchannels. These models are presented by Todreas and Kazimi (Todreas et al., 1990), subchannel analysis code CTF (SALKO et al., 2014) manual and MATRA (Hwang et al., 2008) reports. In this chapter, implemented subchannel T/H models are presented.

2.2.1 Cross flow model

Cross flow model is one of the important subchannel T/H models to analyze the fluid transfer between adjacent subchannels. Due to the lateral pressure difference between two neighboring subchannels, a cross flow can occur. The cross flow model consists of the wall friction and form loss models with consideration of flow direction. For axial direction, wall friction model which considers the friction loss on the fluid-rod interface and the form loss by a grid spacer are implemented into the momentum conservation equation of CUPID. These models are added as a type of pressure drop to axial momentum conservation equation as follows:

$$\vec{M}_{wk} = -\frac{1}{2}\left(\frac{f}{d_{hy}} + K\right)\left(\frac{G^2}{\rho}\right)\Phi \tag{2-25}$$

$$f = aRe^b + c$$

where, f: Friction factor

$G = \sum_k \alpha_k \rho_k U_k$, Mass flux

K: Grid spacer form loss coefficient

Φ: Two-phase multiplier

Friction factor f is the function of Reynolds number and it has different values with laminar and turbulent flow conditions as shown in Table 2.1.

Table 2.1 Friction factor coefficient

Flow condition	a	B	C	Effective Region
Laminar	64.0	-1.0	0.0	Re<2,300
Turbulent (Blasius type)	0.316	-0.25	0.0	2,300<Re<30,000
Turbulent (McAdams type)	0.184	-0.20	0.0	3×10^4<Re<10^6

For considering the additional pressure drop at two-phase flow condition, two-phase multiplier proposed by Armand (Armand, 1946) is used. Two-phase multiplier is defined with the void fraction and quality as follows:

$$\Phi = \frac{(1-x)^2}{(1-\alpha)^{1.42}}, \qquad 0 < \alpha \leq 0.6$$

$$\Phi = 0.478\frac{(1-x)^2}{(1-\alpha)^{2.2}}, \quad 0.6 < \alpha \leq 0.9 \tag{2-26}$$

$$\Phi = 1.73\frac{(1-x)^2}{(1-\alpha)^{1.64}}, \qquad 0.9 < \alpha < 1.0$$

For describing the consecutive fuel gap change by fuel rod arrangement in the transverse direction, the form loss model is added to transverse momentum equation as follows:

$$\vec{M}_{wk,L} = -\frac{K_G}{2}\left(\frac{W_{IJ}|W_{IJ}|}{l_{IJ}\rho_{IJ}s_{IJ}}\right) \tag{2-27}$$

where, $W_{IJ} = \sum_k \alpha_k \rho_k V_{IJ,k} \times s_{IJ,}$ Mass flow which flows subchannel *I* to *J*

l_{IJ}: Length between the center of subchannel *I* and *J*

s_{IJ}: Gap size between two fuel rods

K_G: Transverse form loss coefficient, default value is 0.5

2.2.2 Turbulent mixing model (Equal Mass exchange model)

The turbulent mixing between neighboring subchannels can be occurred due to the turbulent fluctuation and the flow disturbance by structures such as grid spacer mixing vane. In adiabatic single-phase flow, no net mass transfer occurs between adjacent subchannels but momentum and energy can be distributed. This fluid exchange mechanism is modeled by Equal Mass exchange model (EM model). EM model acts only in the lateral directions to reduce the velocity difference between adjacent subchannels. EM model applied to momentum conservation equation is given as Eq. 2-27.

$$\vec{M}_k^T = -\sum w'_{IJ}\left(U_I - U_J\right) \quad (2\text{-}28)$$

where, $w'_{IJ} = \beta \times s_{IJ} \times \bar{G}$, Amount of flow mixing between subchannel I and J

β: Turbulent mixing coefficient, determined by experimental results

$\bar{G}$: Averaged axial mass flux between adjacent subchannels [kg/$m^2 sec$]

2.2.3 Turbulent mixing model (Equal Volume exchange and Void Drift model)

In adiabatic two-phase flow and heated flow condition, mass, momentum and energy transfer can occur between adjacent subchannels. Therefore, equal volumes of fluid and void are exchanged between adjacent subchannels, as opposed to mixing equal masses of fluid. These flow mixing mechanisms are modeled as Equal Volume exchange and Void Drift model (EVVD model). The turbulent mixing terms are modeled by simple diffusion approximation using mixing length theory. As stated in Todreas and Kazimi (Todreas et al., 1990), the

net two phase turbulent mixing of mass, energy and momentum between two adjacent subchannels *I* and *J* can be captured as follows:

The turbulent mixing and void drift of mass transfer:

$$\vec{M}_e^T = \varepsilon \frac{s_{IJ}}{z_{IJ}^T}(\rho_f - \rho_g)\theta \left[\alpha_{v,J} - \alpha_{v,I} - \left(\alpha_{v,J} - \alpha_{v,I}\right)_{equil}\right] \quad (2\text{-}29)$$

The turbulent mixing and void drift of energy transfer:

$$\vec{M}_h^T = \varepsilon \frac{s_{IJ}}{z_{IJ}^T}(\rho_f h_f - \rho_g h_g)\theta \left[\alpha_{v,J} - \alpha_{v,I} - \left(\alpha_{v,J} - \alpha_{v,I}\right)_{equil}\right] \quad (2\text{-}30)$$

The turbulent mixing and void drift of momentum transfer:

$$\vec{M}_k^T = \varepsilon \frac{s_{IJ}}{z_{IJ}^T}(\rho_f v_f - \rho_g v_g)\theta \left[\alpha_{v,J} - \alpha_{v,I} - \left(\alpha_{v,J} - \alpha_{v,I}\right)_{equil}\right] \quad (2\text{-}31)$$

where, ε: Eddy diffusivity

z_{IJ}^T: Turbulent mixing length

α: Void fraction

θ: Two phase multiplier term

There are two components in square brackets of the previous three equations. The first component, $\alpha_{v,J} - \alpha_{v,I}$ represents the equal volume exchange turbulent mixing. The second component, $\left(\alpha_{v,J} - \alpha_{v,I}\right)_{equil}$ known as equilibrium void distribution represents the void drift. By equal volume exchange turbulent mixing model, the difference of void fraction between subchannel *I* and *J* acts driving force to derive the liquid mass to the higher void channel and the vapor mass to the lower void subchannel as presented in Fig. 2.3. But in void drift model, directions of liquid and vapor movement are determined to reach the equilibrium void fraction as presented in Fig. 2.4. Equilibrium void distribution is defined from Lahey's derivation of the equilibrium density distribution (Lahey et al., 1977) using mass flux difference between adjacent subchannels *I* and *J* as follows:

$$\left(\alpha_{v,I} - \alpha_{v,J}\right)_{equil} = K_a\left(\alpha_{v,I} + \alpha_{v,J}\right)\frac{G_I - G_J}{G_I + G_J} \quad (2\text{-}32)$$

Where, scaling factor K_a is generally taken to be 1.4. Void drift phenomenon can be explained by lift force exerted on bubbles. According to Tomiyama experiment (Tomiyama et al., 2002), the physical mechanism of void drift varies depending on bubble diameters. In a bubbly flow with relatively small bubble diameters, lift force acting on bubbles is opposite to liquid velocity gradient. In other words, bubbles are pushed toward subchannel with relatively lower liquid velocity. As the bubble size growing up to reach the critical diameter almost 5 mm, however, bubbles are pushed toward subchannel with relatively higher liquid velocity (Tomiyama et al., 2002). With small hydraulic diameter (below 10 mm) in subchannel, bubble diameters are relatively small and lift force acting on bubbles is opposite to liquid velocity gradient. In contrast, large hydraulic diameter (above 32, 25, 16 mm) in subchannel increases the possibilities of growing up bubbles over the critical size due to the coalescence of bubbles. In this case, bubbles are pushed toward center subchannel with relatively higher liquid velocity (Pang, 2014). The difference of bubbles movement can be considered with changing the sign of scaling factor K_a in EVVD model.

To simplify the equation and notation, mixing term $\varepsilon\frac{s_{IJ}}{z_{IJ}^T}$ is condensed to V^T. With this simplification, EVVD model which is implemented to mass, momentum and energy conservation equations is presented in Table 2.2 separating for gas and liquid phases. This model is added as a source term in mass, momentum and energy conservation equations by subtracting equal volume exchange model to void drift model.

Then, it is necessary to define the mixing term. The mixing term is defined

using mixing parameter β and area-averaged axial mass flux and density of the two adjacent subchannels as below:

$$\varepsilon \frac{s_{IJ}}{z_{IJ}^T} = \frac{\beta \bar{G} s_{IJ}}{\bar{\rho}} \tag{2-33}$$

where, $\bar{G}$: Area averaged axial mass flux between adjacent subchannels

$\bar{\rho}$: Area averaged density between adjacent subchannels

Mixing parameter β is defined as a ratio of the transverse mass flux to the axial mass flux. The value of β can be calculated from flow dependent correlation developed by Rogers and Rosehart (Rogers and Rosehart, 1972). However, in most cases β is defined by users' input.

For considering additional two phase pressure drop, two-phase multiplier θ is introduced. The value of θ for single-phase flow is given as 1.0. Beus (Beus, 1971) proposed the correlation for multiplier θ as follows:

$$\theta = 1 + (\theta_M - 1)\left(\frac{x}{x_M}\right) \qquad x < x_M$$

$$\theta = 1 + (\theta_M - 1)\left(\frac{x_M - x_0}{x - x_0}\right) \qquad x > x_M \tag{2-34}$$

Where, x: Quality

θ_M: Two phase mixing coefficient at the transition point

(given 5 by Faya)

x_M: Quality at the slug-annular transition point,

$x_0/x_M = 0.75Re^{0.0417}$

Quality at the slug-annular transition point x_M is defined using Wallis model (Wallis, 1969) as follows:

$$x_M = \frac{\frac{0.4\left[\rho_f(\rho_f - \rho_g) g D_h\right]^{1/2}}{G} + 0.6}{\left(\frac{\rho_f}{\rho_g}\right)^{1/2} + 0.6} \tag{2-35}$$

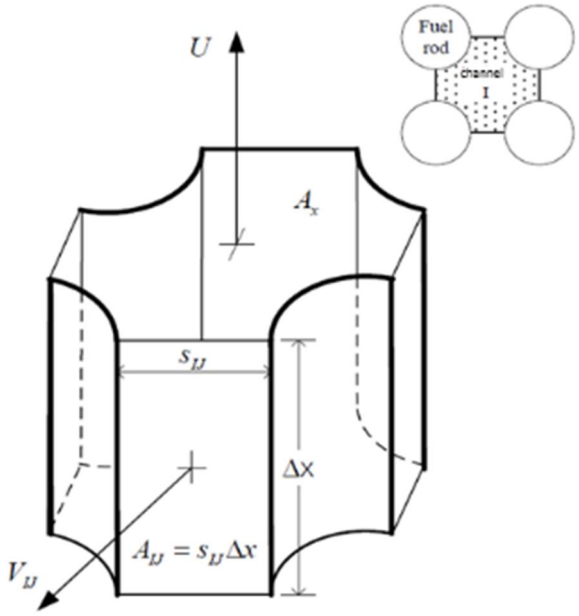

Figure 2.1 Subchannel control volume for axial direction (Kwon et al., 2014)

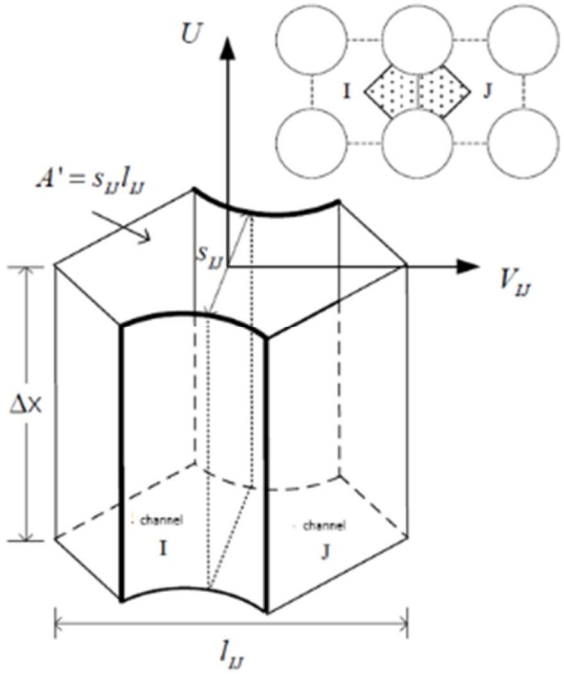

Figure 2.2 Subchannel control volume for transverse direction
(Kwon et al., 2014)

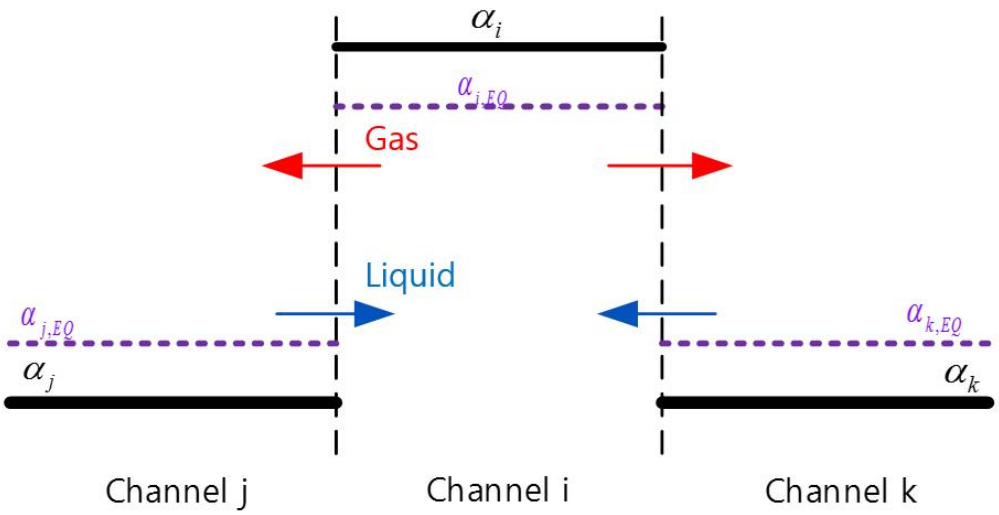

Figure 2.3 Mechanism of equal volume exchange turbulent mixing model

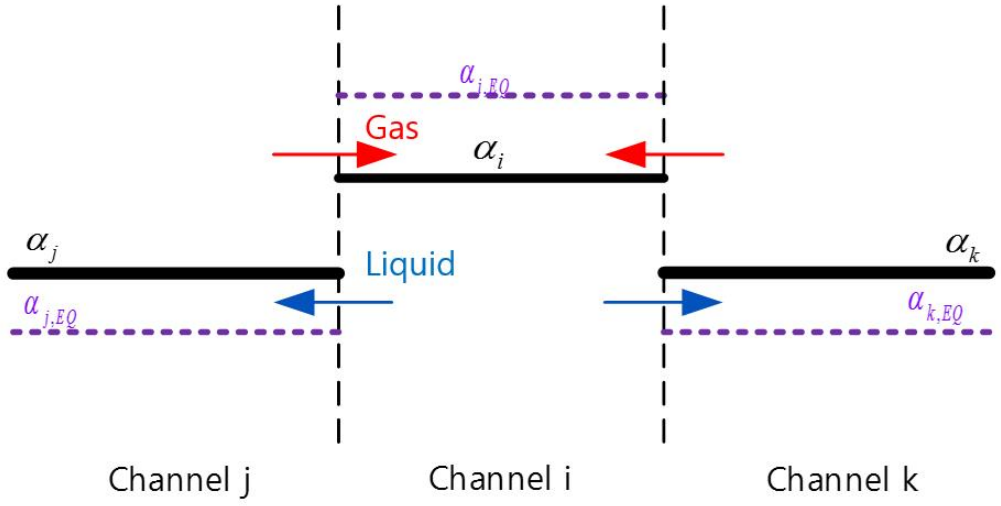

Figure 2.4 Mechanism of void drift model

Table 2.2 Equal volume exchange model and void drift model

	Phase	Equal volume exchange model	Void drift model
Mass	Gas	$\vec{M}_{e,v,TM}^{T} = V^{T}\theta\left[\rho_{v,j}\alpha_{v,j} - \rho_{v,i}\alpha_{v,i}\right]$	$\vec{M}_{e,v,VD}^{T} = -V^{T}\theta\left[K_a\left(\rho_{v,i}\alpha_{v,i} + \rho_{v,j}\alpha_{v,j}\right)\frac{G_i - G_j}{G_i + G_j}\right]$
	Liquid	$\vec{M}_{e,l,TM}^{T} = V^{T}\theta\left[\rho_{l,j}\alpha_{l,j} - \rho_{l,i}\alpha_{l,i}\right]$	$\vec{M}_{e,l,VD}^{T} = V^{T}\theta\left[K_a\left(\rho_{l,i}\alpha_{v,i} + \rho_{l,j}\alpha_{v,j}\right)\frac{G_i - G_j}{G_i + G_j}\right]$
Energy	Gas	$\vec{M}_{h,v,TM}^{T} = V^{T}\theta\left[\rho_{v,j}\alpha_{v,j}h_{v,j} - \rho_{v,i}\alpha_{v,i}h_{v,i}\right]$	$\vec{M}_{h,v,VD}^{T} = -V^{T}\theta\left[K_a\left(\rho_{v,i}\alpha_{v,i}h_{v,i} + \rho_{v,j}\alpha_{v,j}h_{v,j}\right)\frac{G_i - G_j}{G_i + G_j}\right]$
	Liquid	$\vec{M}_{h,l,TM}^{T} = V^{T}\theta\left[\rho_{l,j}\alpha_{l,j}h_{l,j} - \rho_{l,i}\alpha_{l,i}h_{l,i}\right]$	$\vec{M}_{h,l,VD}^{T} = V^{T}\theta\left[K_a\left(\rho_{l,i}\alpha_{v,i}h_{l,i} + \rho_{l,j}\alpha_{v,j}h_{l,j}\right)\frac{G_i - G_j}{G_i + G_j}\right]$
Momentum	Gas	$\vec{M}_{k,v,TM}^{T} = V^{T}\theta\left[\frac{\dot{m}_{v,j}}{A_j} - \frac{\dot{m}_{v,i}}{A_i}\right]$	$\vec{M}_{k,v,VD}^{T} = -V^{T}\theta\left[K_a\left(\frac{\dot{m}_{v,i}}{A_{v,i}}\alpha_{v,i} + \frac{\dot{m}_{v,j}}{A_{v,j}}\alpha_{v,j}\right)\frac{G_i - G_j}{G_i + G_j}\right]$
	Liquid	$\vec{M}_{k,l,TM}^{T} = V^{T}\theta\left[\frac{\dot{m}_{l,j}}{A_j} - \frac{\dot{m}_{l,i}}{A_i}\right]$	$\vec{M}_{k,l,VD}^{T} = V^{T}\theta\left[K_a\left(\frac{\dot{m}_{l,i}}{A_{l,i}}\alpha_{v,i} + \frac{\dot{m}_{l,j}}{A_{l,j}}\alpha_{v,j}\right)\frac{G_i - G_j}{G_i + G_j}\right]$

2.3 Constitutive Models for a Two Phase flow in CUPID

For analyzing two-phase flow and heat transfer in PWR steam generators, CUPID-SG (CUPID code for Steam Generators) subroutine was already built in CUPID code (Kim et al., 2014). In CUPID-SG, physical models from system scale analysis code MARS are implemented to treat the complex thermal-hydraulics phenomena in a shell side of a PWR steam generator. CUPID-SG has a various constitutive models for two-phase flow analysis such as flow regime map for vertical channel, interfacial area concentration, interfacial momentum transfer, interfacial heat and mass transfer and heat partitioning in vertical flows over tube bundle, etc. And the code was validated with FRIGG test by Kim et al (Kim et al., 2014). For two-phase flow analysis in rod bundle, CUPID-SG subroutine is activated. In this section, constitutive models implemented in CUPID-SG subroutine are introduced.

Flow regime map

For analyzing coarse mesh such as subchannel mesh, a flow regime concept used at system scale or component scale code is appropriate. Therefore, 1D flow regime map indicated in Fig. 2.5 which covers bubbly to annular-mist flow regimes is implemented to CUPID-SG. This 1D flow regime map is implemented to system scale analysis code MARS (Multi-dimensional Analysis of Reactor Safety) (KAERI, 2009) and SPACE (Safety and Performance Analysis CodE for nuclear power plants) (KAERI, 2011).

Interfacial area concentration

The interfacial area concentration models of MARS code are implemented to CUPID-SG. Table 2.3 shows the interfacial area concentration models following the interfacial shape.

Interfacial momentum transfer

In momentum conservation equation, the interfacial momentum transfer is calculated using volumetric drag force for bubbles. Drag coefficient and drag force per unit volume are presented in Table. 2.4.

Interfacial heat transfer

Interfacial heat transfer models for bubbly, slug and annular-mist flow are implemented from MARS code to CUPID-SG. These models are used for providing volumetric heat transfer coefficient in energy conservation equation as presented in Table 2.5.

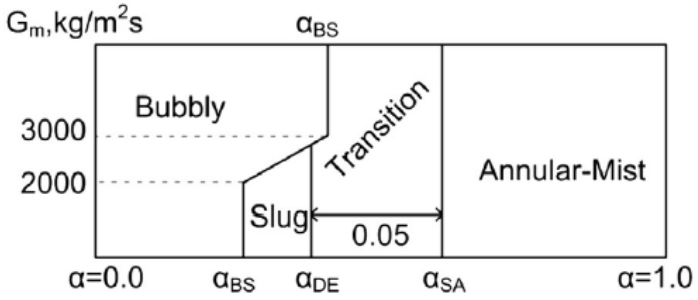

Figure 2.5 Flow regime map in CUPID-SG code (Kim et al., 2014)

Table 2.3 Interfacial area concentration following interfacial shape (Kim et al., 2014)

Interfacial shape	Interfacial area concentration
Small bubbles in bubbly or slug flows	$a_{SB} = \frac{3.6\alpha_{SB}}{d_b}$ where, $d_b = \frac{We_{crit}\sigma}{\rho_l v_{fg}^2}$
Taylor bubbles in slug flow	$a_{TB} = \frac{4.5\alpha_{TB}}{D} \times 2.0$ where, $\alpha_{TB} = \frac{\alpha-\alpha_{gs}}{1.0-\alpha_{gs}}$, $\alpha_{gs} = \alpha_{BS} exp\left(-8\frac{\alpha-\alpha_{BS}}{\alpha_{SA}-\alpha_{BS}}\right)$
Liquid film in annular flow	$a_{ANN} = \frac{4}{D}\left(1-\alpha_{ff}\right)^{1/2} \times 2.5\left(30\alpha_{ff}\right)^{1/8}$

Table 2.4 Drag coefficient and drag force per unit volume (Kim et al., 2014)

	Small bubbles in bubbly or slug flow	Taylor bubbles in slug flow	Annular flow
Drag force per unit volume	$F_{i,SB} = \frac{1}{8}\rho_c \lvert v_R \rvert v_R C_{D,SB} a_{i,SB}$	$F_{i,TB} = \frac{1}{2}\rho_f \lvert v_R \rvert v_R C_{D,TB} \frac{\alpha_{TB}}{L}$	$F_{i,ANN} = \frac{1}{2}\rho_g \lvert v_R \rvert v_R f_{i,ANN} a_{i,ANN}$
Drag coefficient	$C_{D,SB} = \frac{24}{Re_b}\left(1.0 + 0.1 Re_b^{0.75}\right)$ where, $Re_b = \frac{\rho_l d_b \lvert v_R \rvert}{\mu_{mb}}, \mu_{mb} = \frac{\mu_l}{1-\alpha_g}$	$C_{D,TB} = 10.9\alpha_{TB}^{0.5}(1-\alpha_{TB})^3$	$f_{i,ANN}$ is given by Churchill, Fore, Asali for flow regime.

Table 2.5 Heat transfer coefficient per unit volume (Kim et al., 2014)

	Small bubbles in bubbly or slug flow	Taylor bubbles in slug flow	Annular flow
Superheated liquid	Plesset and Zwick(1954) or modified Lee and Ryley(1968)	A large coefficient for liquid	A large coefficient for liquid
Subcooled liquid	Modified (Unal, 1976; Lahey, 1978)	Dittus-Boelter type forced convection (KAERI, 2009)	Modified Theofanous (1979)
Superheated vapor	A large coefficient for vapor	Modified Lee-Ryley (KAERI, 2009)	Modified Dittus and Boelter (1930)
Subcooled vapor	A large coefficient for vapor	A large coefficient for vapor	

Chapter 3.

Verification and Validation of CUPID Subchannel T/H Models

In the present study, CUPID code with implemented subchannel scale models was validated against rod bundle flow mixing experiments under various flow conditions. Following the MATRA's validation matrix, current validation state of CUPID code is shown in the Table 3.1. For unheated single-phase flow, four subchannel tests were simulated for the validation including CNEN 4x4 test for verifying mixing effect between adjacent subchannels, PNL 7x7 test for investigating the velocity redistribution near blockage, CE 15x15 test for verifying the effect of non-uniform inlet velocity on the flow distribution and WH 14x14 test for investigating the flow redistribution between two open 14x14 assemblies when partial or complete blockage occurs at the entrance of one assembly. For heated single-phase flow, PNNL 2x6 test for verifying the buoyancy effect with non-uniform power distribution was validated. RPI air-water test, Tapucu and Van der Ros two-channel tests were validated for predicting the bubble behavior under air-water two-phase flow condition. These validations were performed with CUPID additionally although they are not included in MATRA validation matrix, because deficiency of the turbulent mixing model in predicting bubble behavior between two neighboring subchannels is newly issued in CTF

(Pang, 2014). Finally, GE 3x3 mixing test for investigating void fraction distribution against heated two-phase flow was validated.

In this chapter, calculation results of CUPID are compared with the calculation results of MATRA, CTF and available experimental data.

Table 3.1 Current state of CUPID code validation

Tests			Codes	
			MATRA	CUPID
Single-phase	Unheated	CNEN 4×4 mixing test	O	O
		PNL 7×7 flow blockage test	O	O
		CE 15×15 inlet jetting test	O	O
		WH 14×14 inlet blockage test	O	O
	Heated	WH Zion-1 core exit temperature test	O	
		PNNL 2×6 buoyancy effect test	O	O
Two-phase	Unheated	RPI air-water mixing test		O
		Tapucu two-channel test		O
		Van der Ros two-channel test		O
	Heated	GE 3×3 mixing test	O	O
		CU 4×4 exit flow & enthalpy test	O	
		ISPRA 4×4 mixing test	O	
		FRIGG 36-rod (two-phase ΔP, void)	O	
		BFBT 8×8 void distribution test	O	
		PSBT 5×5 void distribution test	O	

3.1 Unheated Single-Phase Flow

3.1.1 CNEN 4×4

The CNEN 4x4 test (Marinelli et al., 1972) performed at Studsvik laboratory for verifying the flow mixing effect between adjacent subchannels was selected. The test section includes a bundle of 16 unheated rods of 0.015 m diameter, 0.019 m pitch and the width of assembly is 0.08 m, height is 1.4 m. One grid spacer is located at the middle elevation of bundle. Hydraulic diameters at corner, side and center subchannels are 0.007 m, 0.012 m and 0.016 m, respectively. The cross sectional view of test section is shown as Fig. 3.1. Using special probe performing the dual function of pitot tube and thermocouple, outlet liquid velocities were measured at corner, side and center subchannels under various inlet flow conditions (see Table 3.2).

In the code calculation, 1,250 (5x5x50) cuboidal computing cells were used to model the 5x5 subchannels made from 4x4 rod arrays with uniformly divided height of 50 axial meshes. The applied subchannel models for the calculation are written in Table 3.3. With the grid spacer model, pressure drop along the axial direction was calculated at case 1, 3 and 5. The calculation results agreed well with MATRA as shown in Fig. 3.2, and the largest pressure drop was calculated at case 5 which has the fastest liquid velocity.

Fig. 3.3 shows the calculation result of liquid velocity contour at eight different elevations. Following the calculation result, the liquid is concentrated to the center subchannels from the side and corner subchannels as it flows upward. The center subchannels have large hydraulic diameters than others, and due to the

cross flow models, they have low flow resistance than others.

Also, calculations for verifying the effect of EM turbulent mixing model were performed. Without applying the EM turbulent mixing model, the momentum loss at the corner and side subchannels cannot be compensated. So the liquid velocities are underestimated at the corner and side and overestimated at the center channels. In the case of applying EM turbulent mixing model, this phenomenon can be mitigated, so the calculation results of liquid velocities could capture the experimental data. These calculation results clearly show the effect of turbulent mixing for describing a real phenomenon. With applying EM model, CUPID could predict the liquid velocity compared to the experimental data within the error range of -2.6 ~ 0.5 % at the corner and -1.8 ~ 0.8 % at the center subchannel.

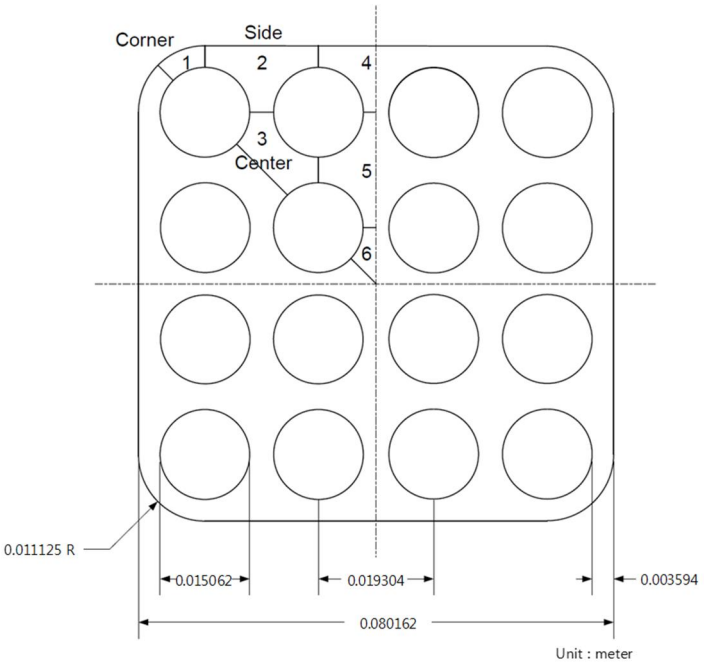

Figure 3.1 Cross sectional view of CNEN 4x4 test section (Unit: m)

Table 3.2 Inlet flow conditions for CNEN 4x4 test

Case	Pressure	T_{in}	Velocity
	MPa	K	m/sec
1	0.102	300	0.64
2	0.102	300	1.32
3	0.102	300	2.61
4	0.102	300	3.83
5	0.102	300	5.18

Table 3.3 Applied subchannel models in CNEN 4x4 test validation

	Lateral	Axial	Note
Wall friction		O	Friction factor coefficient Re<2,300 $f = 64 \times Re^{-1.0}$ 2,300<Re<3×10^4 $f = 0.316 \times Re^{-0.25}$ 3×10^4<Re<10^6 $f = 0.184 \times Re^{-0.20}$
Form loss	O		$K_G = 0.5$
Turbulent mixing		O	EM(Equal Mass exchange) Model β = 0.02
Grid spacer		O	Form loss coefficient(K) = 0.6

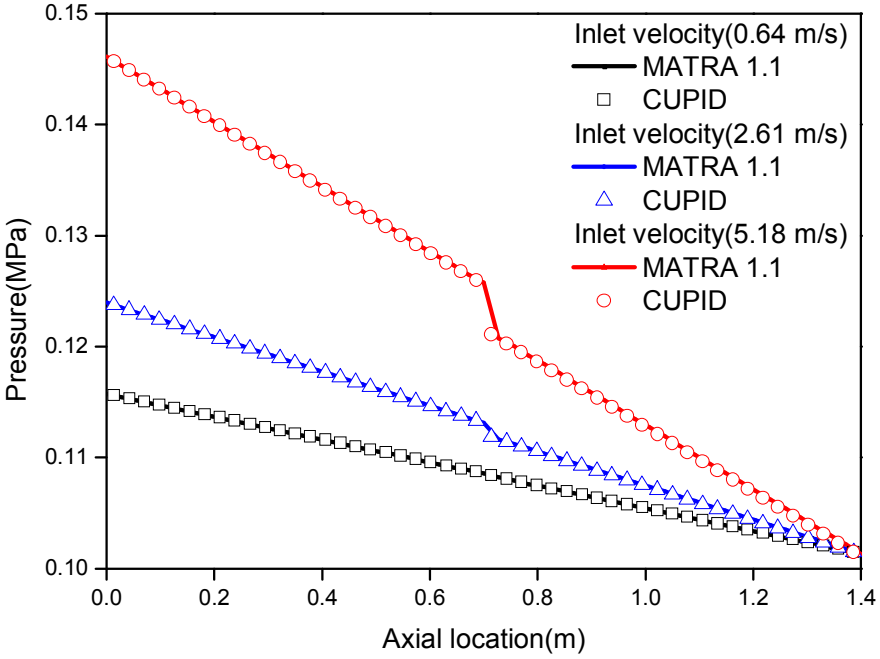

Figure 3.2 Pressure drop along axial direction in CNEN 4x4 test

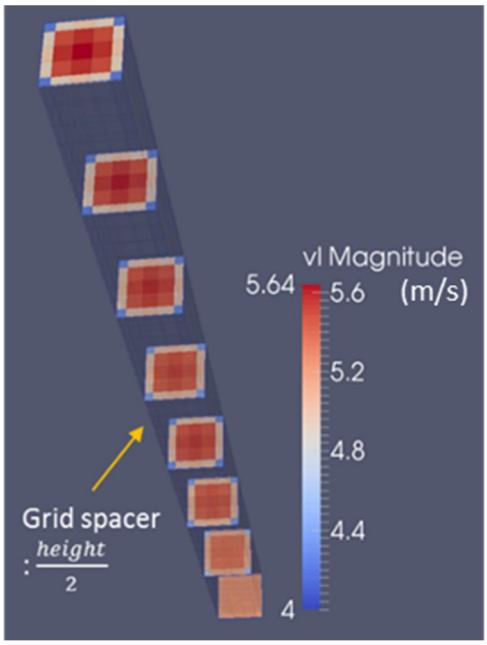

Figure 3.3 Velocity contour along axial direction in CNEN 4x4 test

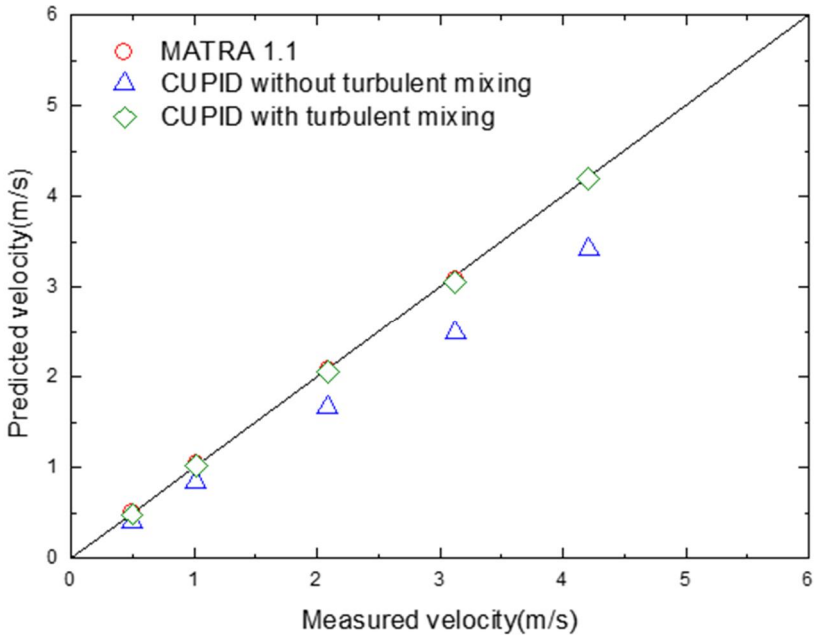

(a) Outlet velocity at corner subchannel

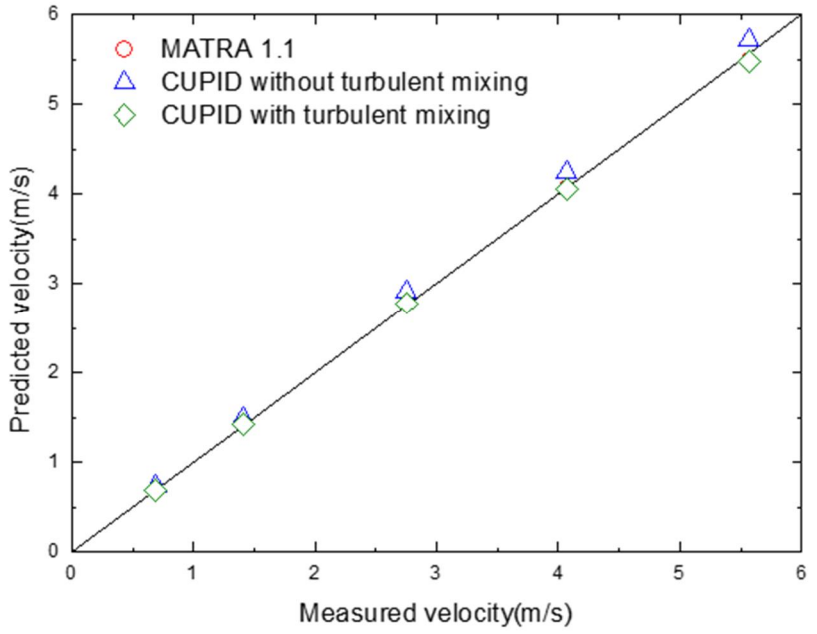

(b) Outlet velocity at center subchannel

Figure 3.4 Outlet velocity at corner (a) and center (b) subchannel in CNEN 4x4 test

3.1.2 PNL 7×7

The PNL 7x7 test (Creer et al., 1976) was performed at Pacific Northwest Laboratory for verifying the flow redistribution near a postulated sleeve blockage. During Loss-Of-Coolant Accident (LOCA) at pressurized water reactors, channel blockage phenomena in rod bundle may occur as a result of swelling or ballooning on the fuel rod. The concept of postulated sleeve blockage at the nine central rods in the bundle was adopted for simulating 70 % area reduction in the four central subchannels between two grid spacer. Test section consists of 7x7 rod bundle of 0.01 m diameter pins with pitches of 0.0137 m and the width of assembly is 0.1033 m. The number of grid spacer is three and cross sectional and longitudinal view of test sections are given at Fig. 3.5 and Fig. 3.6, respectively. The change of each subchannel geometry near the blockage rods was considered in the calculation with different porosity and hydraulic diameter input as summarized in Table 3.4.

The test was performed with the working fluid of water at 0.12 MPa, 302.6 K and inlet Reynolds number was 2.95×10^4. The number of cells used in the calculation was 1,600 (8x8x25) and locally refined meshes were used at the blockage section for high precision simulation near blockage. Implemented subchannel models are given as Table 3.5.

Following the calculation results of stream line (see Fig. 3.7) and axial velocity contour (see Fig. 3.8), bypass flow near the sleeve blockage was properly simulated with CUPID. Normalized liquid velocity along the centerline of subchannel 1 in Fig. 3.5 was extracted and plotted in Fig. 3.9. A sudden increase of velocity, so called jet effect, and flow recovery phenomena by turbulent mixing were reasonably reproduced by CUPID.

For evaluating the capability of CUPID for simulation of a nearly full blockage case, conceptual analysis was carried out with increasing blockage ratio up to 99 %. In this problem case, lateral flows are dominant so there may exist limitation in solving this problem with using spatial marching scheme. However, CUPID code adopts pressure velocity linked scheme to solve the conservation equations and solves the three-dimensional momentum equations for whole computational domain at once by building a system of the pressure correction equations, it is desired to treat the full blockage case where the later velocity becomes dominant. As the blockage ratio increases, the amount of liquid which flows into the subchannel decreases due to high flow resistance and the liquid velocity at subchannel 1 reaches almost zero as presented in Fig. 3.10.

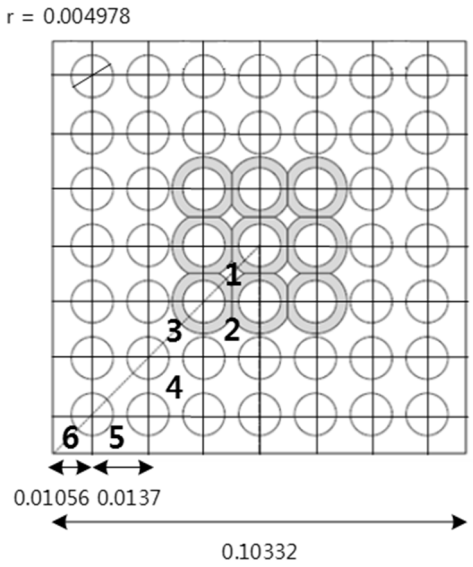

Figure 3.5 Cross sectional view of PNL 7x7 test section (Unit: m)

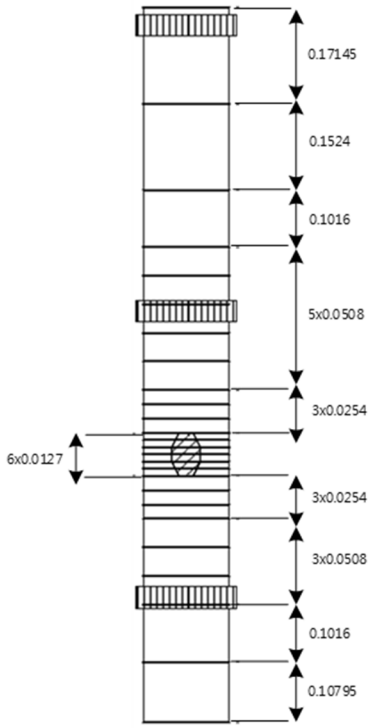

Figure 3.6 Longitudinal view of PNL 7x7 test section (Unit: m)

Table 3.4 Subchannel geometry near blockage

Subchannel number	Porosity	Hydraulic diameter(m)
1	0.1756	0.0043
2	0.3778	0.0083
3	0.4805	0.0104
4	0.5852	0.0140
5	0.7309	0.0144
6	0.8255	0.0127

Table 3.5 Applied subchannel models in PNL 7x7 test validation

	Lateral	Axial	Note
Wall friction		O	Friction factor coefficient $f = 0.34 \times Re^{-0.25}$
Form loss	O		$K_G = 0.5$
Turbulent mixing		O	EM(Equal Mass exchange) Model $\beta = 0.02$
Grid spacer		O	Form loss coefficient(K) = 1.14

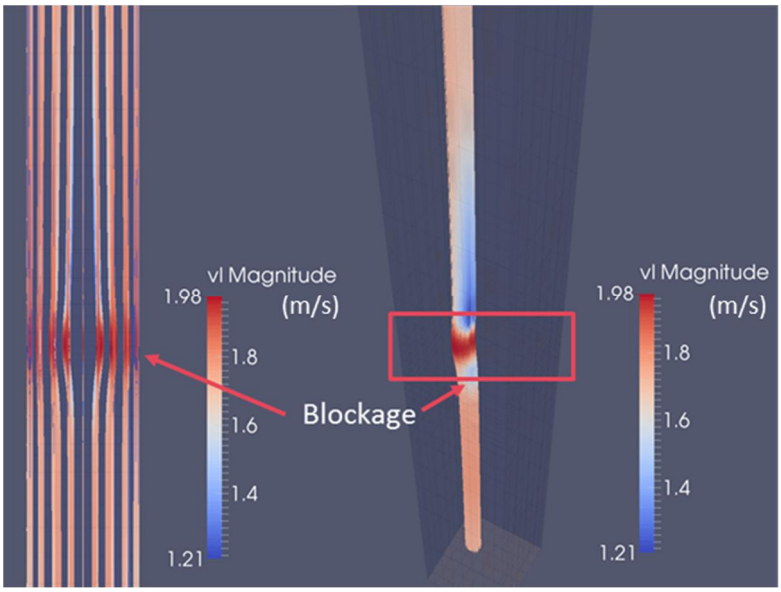

Figure 3.7 Stream line along axial direction at PNL 7x7 test

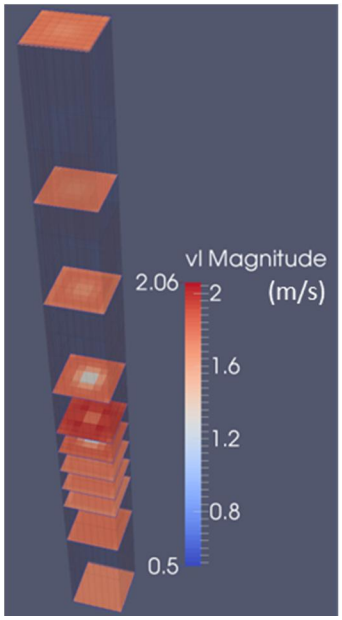

Figure 3.8 Velocity contour along axial elevation at PNL 7x7 test

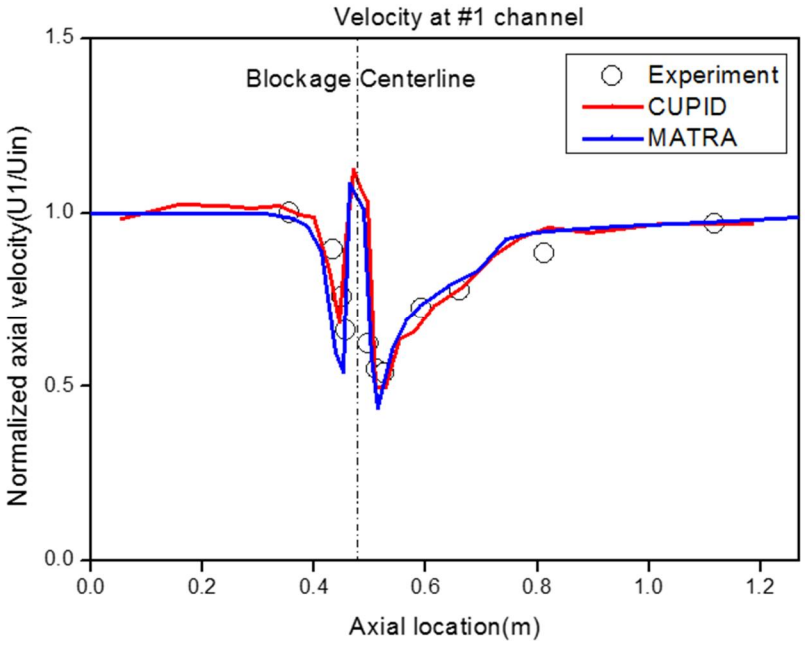

Figure 3.9 Velocity along axial line at channel 1 with 70 % blockage ratio

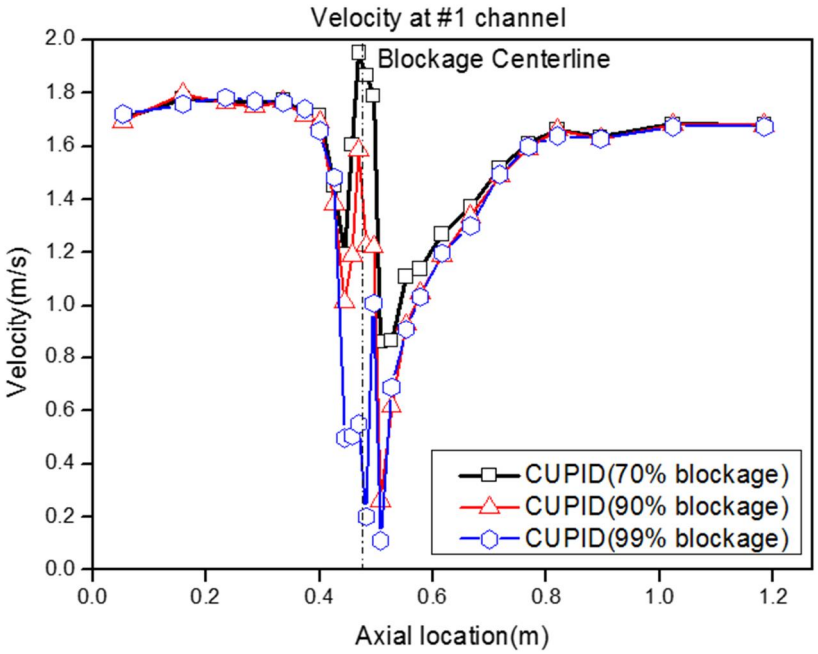

Figure 3.10 Velocity along axial line at channel 1 with increasing blockage ratio (Up to 99 %)

3.1.3 CE 15×15

The CE 15x15 (Marshall et al., 1969) test was performed at nuclear laboratory at combustion engineering for verifying the influence of non-uniform inlet velocity on flow distributions in rod bundle. Non-uniform inlet velocity could be produced by the core support structure and the end fittings. The test was performed at atmospheric pressure of 0.1014 MPa, and room temperature of 298.2 K. Non-uniform inlet flow distributions were produced by inlet jet nozzle with average mass flow rate 2,000 gpm at Reynolds number of 47,000. When the inlet average mass flow rate is converted to velocity in SI unit, the inlet average velocity becomes 2.05 m/s.

The test section consists of 225 unheated rods of 0.0159 m diameter, 0.0213 m pitch, and the assembly width and height are 0.3259 m and 1.1684 m, respectively. One grid spacer is located at the middle of assembly. Hydraulic diameters at corner, side and center subchannels are 0.0147 m, 0.0174 m and 0.0204 m, respectively. The cross sectional and longitudinal view of test section are shown as Fig. 3.11 and Fig. 3.12. In Fig. 3.12, the local velocity was measured by pitot tube at three different axial levels (L/D=0.5, 21, 44). For investigating the change of flow distributions, liquid velocity was measured traversing tangential line which aligned to jet boundary and center line which directly cross the jet centerline. In the calculation, the number of computing cells with 32 non-uniform height meshes was 8,192 (16x16x32). Implemented subchannel models and inlet velocity distributions at each subchannels are indicated in Table 3.6 and Fig. 3.13, respectively.

Following the calculation result of axial velocity contour map at Fig. 3.14, as the liquid flows upward, velocity distributions were flattened due to the influence

of the cross flow and the turbulent mixing models. The calculation results of CUPID at center line and tangent line showed good agreement with the calculation results of MATRA and experimental data as shown in Fig. 3.15 and Fig. 3.16. The maximum error of CUPID at center line is 8.2 % and tangent line is 9 % with compared to the experimental data.

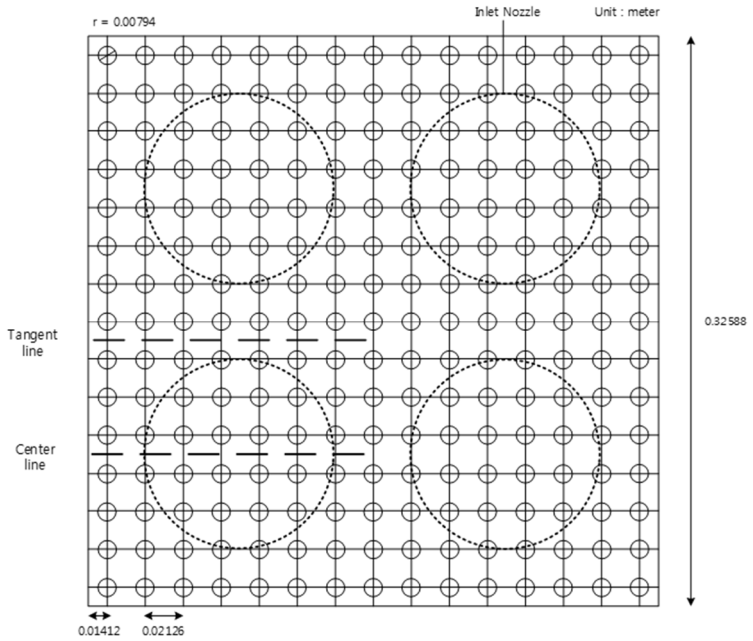

Figure 3.11 Cross sectional view of CE 15x15 test section (Unit: m)

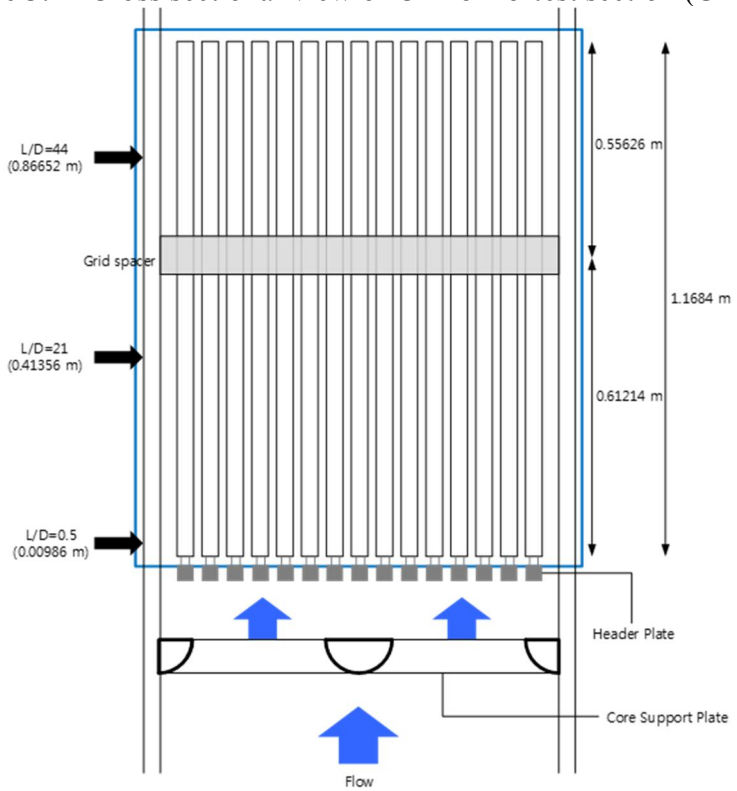

Figure 3.12 Longitudinal view of CE 15x15 test section (Unit: m)

Table 3.6 Applied subchannel models in CE 15x15 test validation

	Lateral	Axial	Note
Wall friction		O	Friction factor coefficient $f = 0.184 \times Re^{-0.2}$
Form loss	O		$K_G = 0.5$
Turbulent mixing		O	EM(Equal Mass exchange) Model $\beta = 0.02$
Grid spacer		O	Form loss coefficient(K) = 1.0

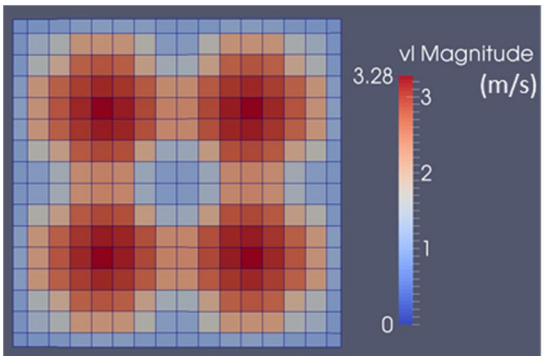

Figure 3.13 Non-uniform inlet velocity distribution at CE 15x15 test

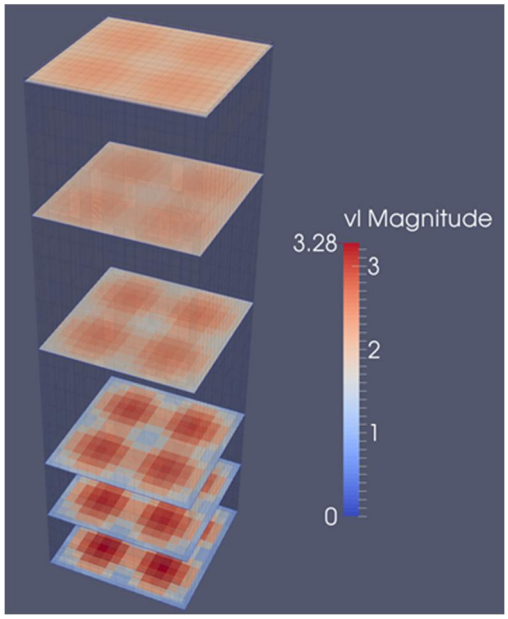

Figure 3.14 Velocity contour along axial elevation at CE 15x15 test

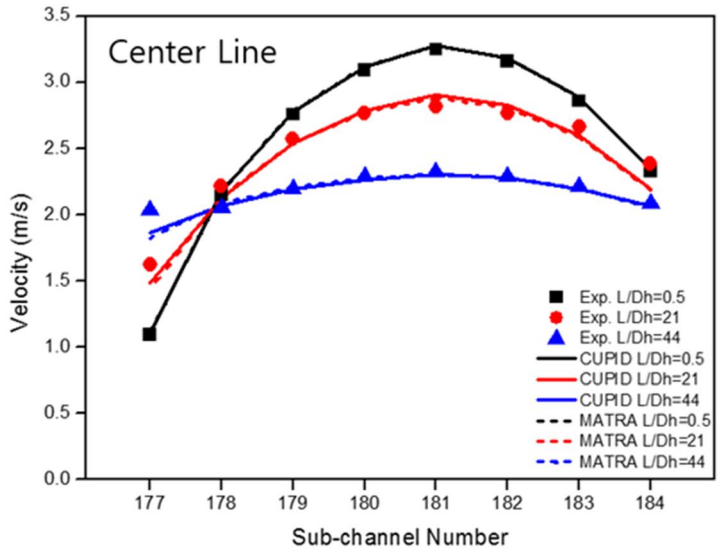

Figure 3.15 Outlet velocity traversing at center line

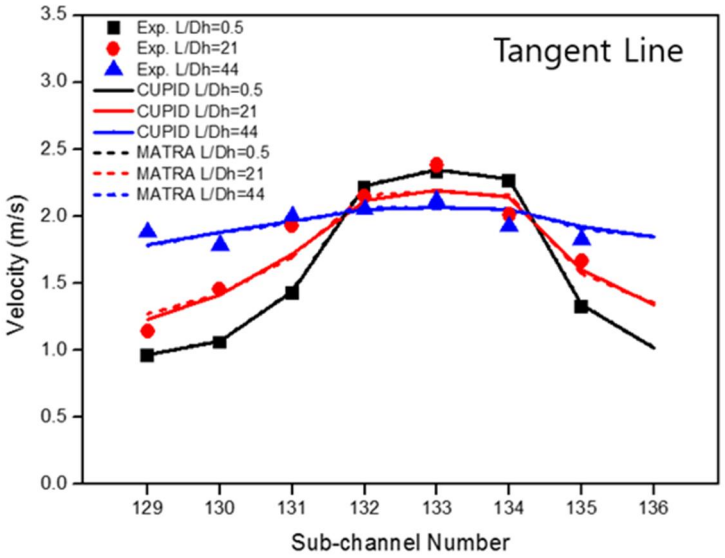

Figure 3.16 Outlet velocity traversing at tangent line

3.1.4 WH 14×14

The WH 14x14 test (Chelemer et al., 1973) had been carried out at Westinghouse in 1968. The test investigated the flow redistribution between two open assemblies caused by partial or full blockage which can occur at the entrance of one assembly. The test section consists of two open 14x14 assemblies with a rod diameter 0.0108 m, a pitch to diameter (pitch/diameter) 1.28 and two assemblies are connected with water gap. A width and height of one assembly are 0.389 m and 0.1938 m, respectively. Hydraulic diameters at corner, side and center subchannels are 0.0044 m, 0.0065 m and 0.0118 m, respectively. The height of rod bundle is 0.9652 m. Local liquid velocity and static pressure were measured by pitot tubes traversing the test section in rows 1, 2 and 3 at seven different axial elevations. The cross sectional and longitudinal view of test section are shown as Fig. 3.17 and Fig. 3.18.

The test was performed at atmospheric pressure of 0.1014 MPa, and room temperature of 299.8 K. To simulate partially blocked or completely blocked at the entrance of one assembly, different inlet mass flows were input to two assemblies. At the case of partial blockage test, inlet mass flow rates at bundle 1 and bundle 2 were set to 1,110 gpm/550 gpm. The inlet average velocities at bundle 1 and bundle 2, which are converted from the inlet mass flow rates, become 3.52 m/s and 1.76 m/s. For the water gap, 2.64 m/s liquid velocity which means averaged velocity between the two assemblies was assigned.

In the calculation, the number of computing cells with uniform height which divides the test section into 38 meshes was 16,530 (15x29x38). In this validation test, turbulent mixing model was disabled, so the cross flow model was the only driving force to determine the flow distributions. Implemented subchannel models

are indicated as Table. 3.7. Following the calculation results of CUPID, mass flows in each bundle were gradually flattened as the liquid flows upward due to the influence of cross flow models as shown in Fig. 3.19. The percent of total flow at bundle 1 and 2 along axial level are presented as Fig. 3.20, and it indicates that the flow mixing phenomena occurs between two different assemblies. Fig 3.21 shows the averaged local velocity in subchannel which traverse row 1, 2 and 3 at seven different axial levels. The velocity peak was observed at water gap which has larger flow area than other channels.

Additionally, the case of complete blockage test was performed with CUPID. In this test, inlet mass flow rates set to 1,100 gpm/0 gpm at each rod bundle, respectively. So, the inlet average velocities at bundle 1 and 2 become 3.52 m/s and 0 m/s. Calculation results of liquid velocity distributions are presented as axial velocity contour map in Fig. 3.22 and velocity vector map in Fig. 3.23. As shown in Fig. 3.23, a reasonable calculation result including the flow recirculation near the inlet of complete blockage assembly could be obtained. Fig. 3.24 shows the averaged local velocity in subchannel which traverse row 1, 2 and 3 at three different axial levels 1, 2 and 7. At axial level 1 and 2 located near the complete blockage region, the negative liquid velocities were detected.

Analyzing this flow recirculation phenomenon depends on numerical schemes used in the code. In spatial marching scheme, it solves the conservation equations at a certain plane, and the obtained solutions are used for the boundary conditions at a next plane. So, it has advantageous for saving computing time in the case when axial flows are dominant, because it handles small subdomains for the calculation. But, if a reverse flow appears, the boundary conditions for the next plane cannot be defined and there exist limitation for calculating reverse flow.

On the other hand, the pressure velocity linked scheme used in CUPID solves the problem with satisfying the conservation equations over the whole calculation domains. Therefore, it takes longer computing time compared to the case of using spatial marching scheme, but reverse flow can be reproduced with this numerical scheme.

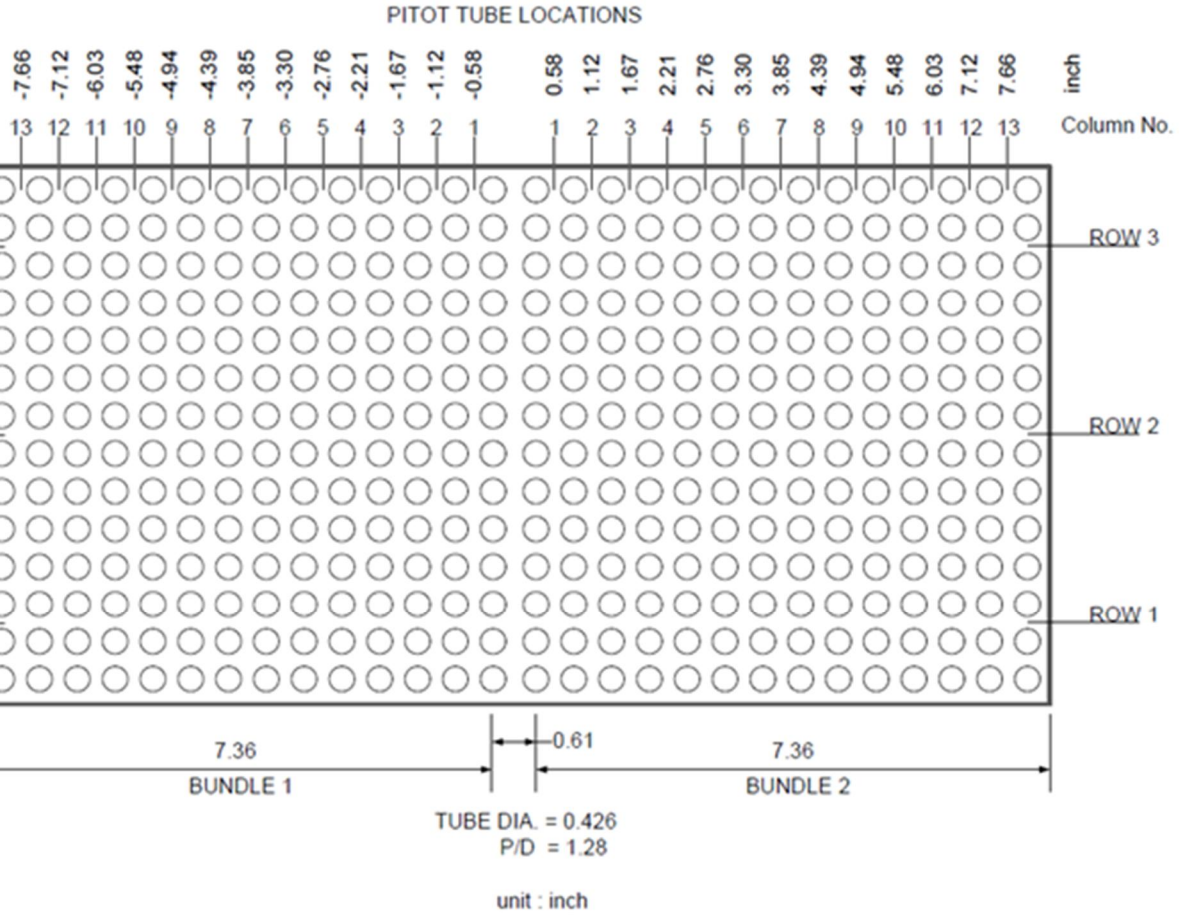

7 Cross sectional view of WH 14x14 test section and pitot tube locations (Unit: inch)

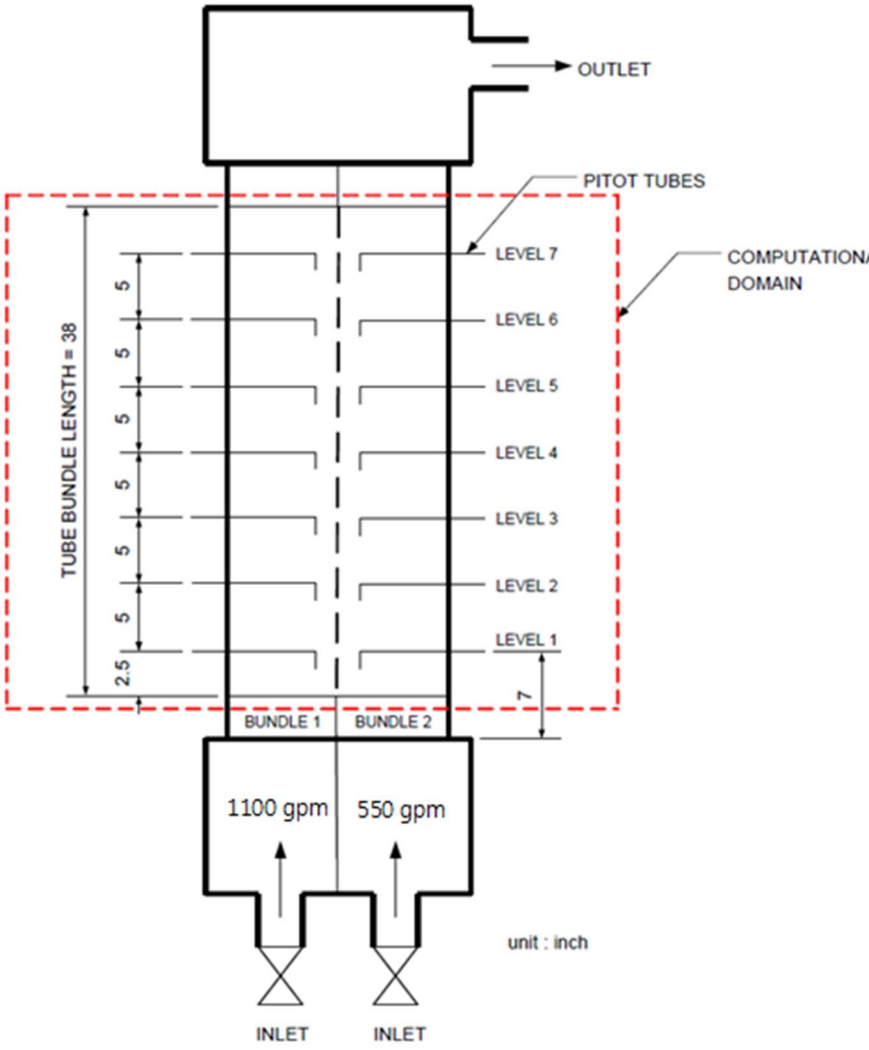

Figure 3.18 Longitudinal view of WH 14x14 test section (Unit: inch) (Chelemer et al., 1973)

Table 3.7 Applied subchannel models in WH 14x14 test validation

	Lateral	Axial	Note
Wall friction		O	Friction factor coefficient $f = \max[\,0.316 \times Re^{-0.25}, 64.0 \times Re^{-1.0}]$
Form loss	O		$K_G = 0.5$
Turbulent mixing		X	
Grid spacer		X	

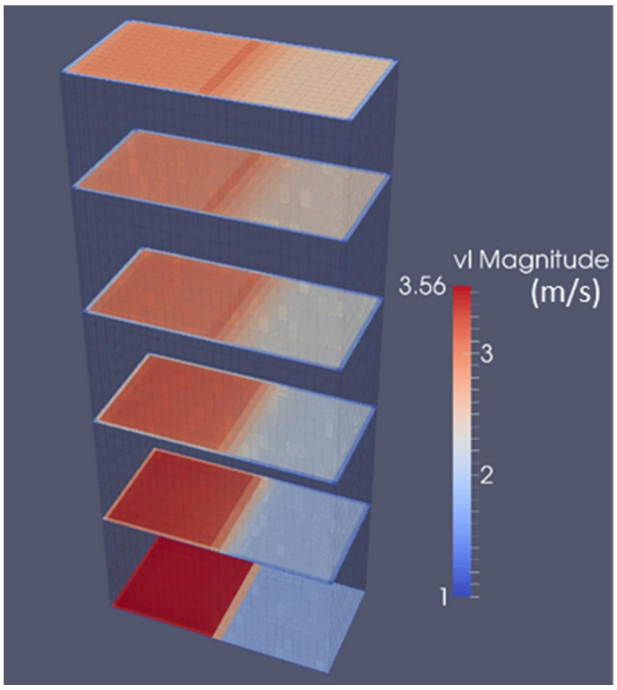

Figure 3.19 Axial velocity contour of WH 14x14 partial blockage case

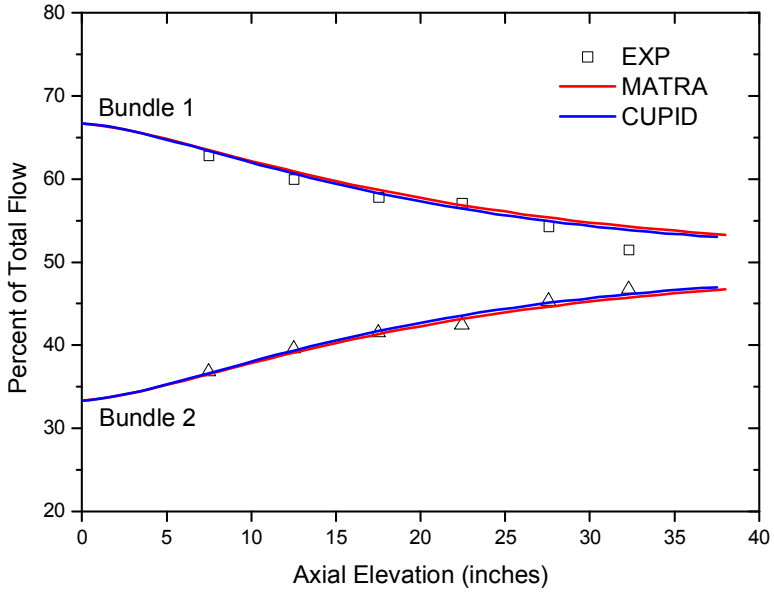

Figure 3.20 Percent of total flow at bundle 1 and bundle 2

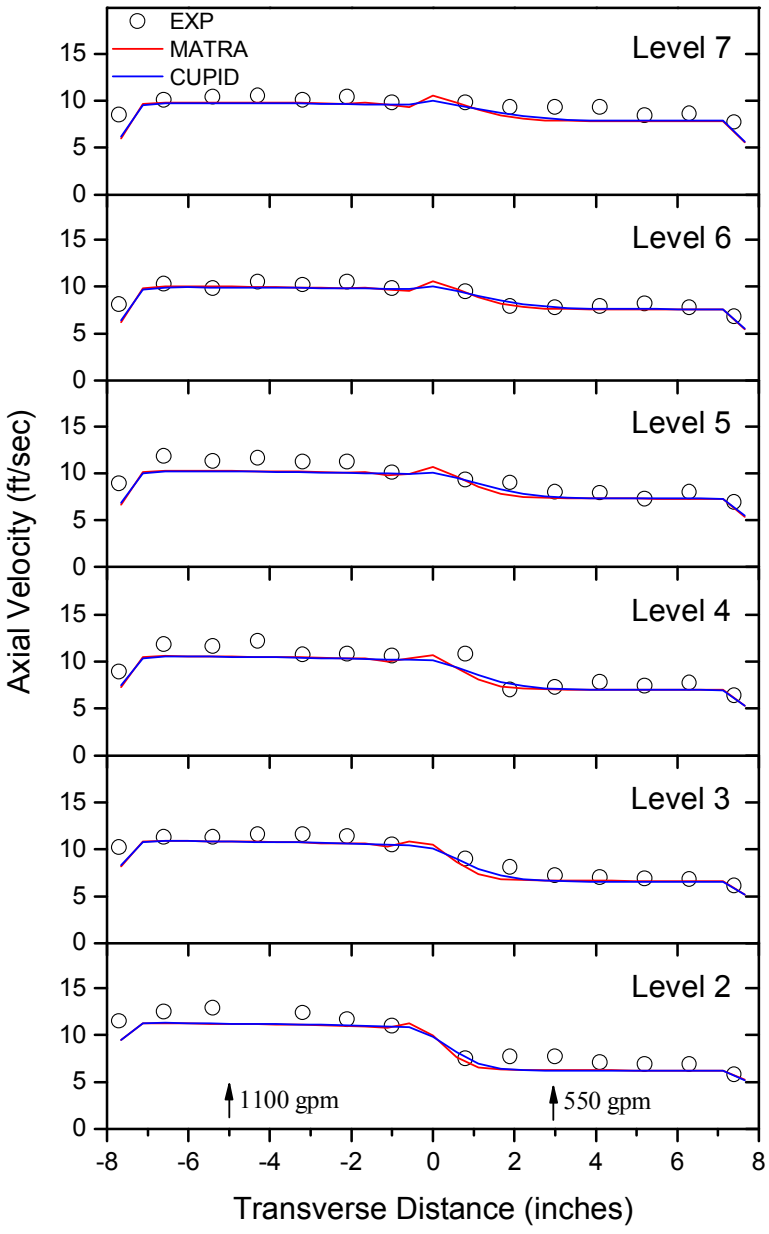

Figure 3.21 Averaged local velocity at different axial levels

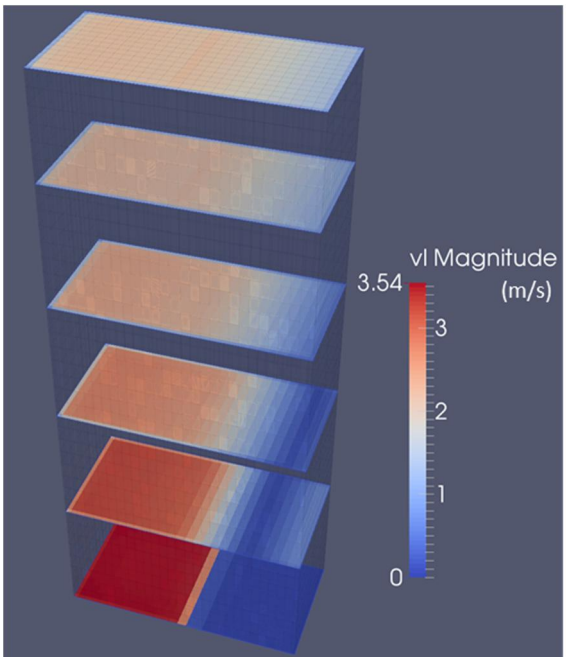

Figure 3.22 Axial velocity contour of WH 14x14 full blockage case

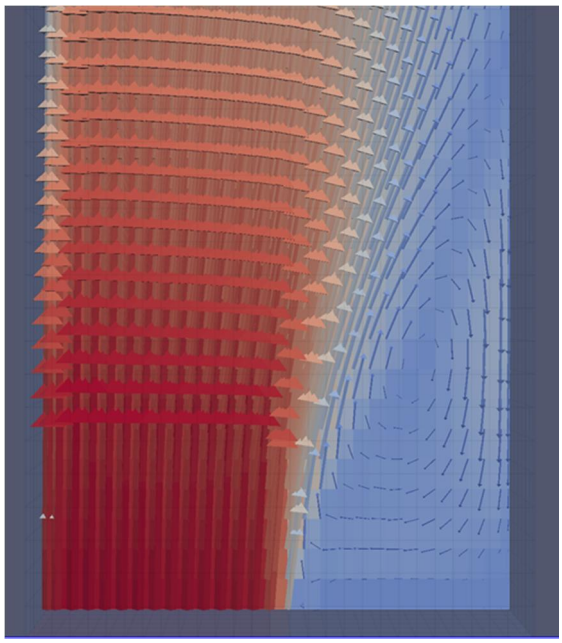

Figure 3.23 Velocity vector near the inlet nozzle of WH 14x14 full blockage case

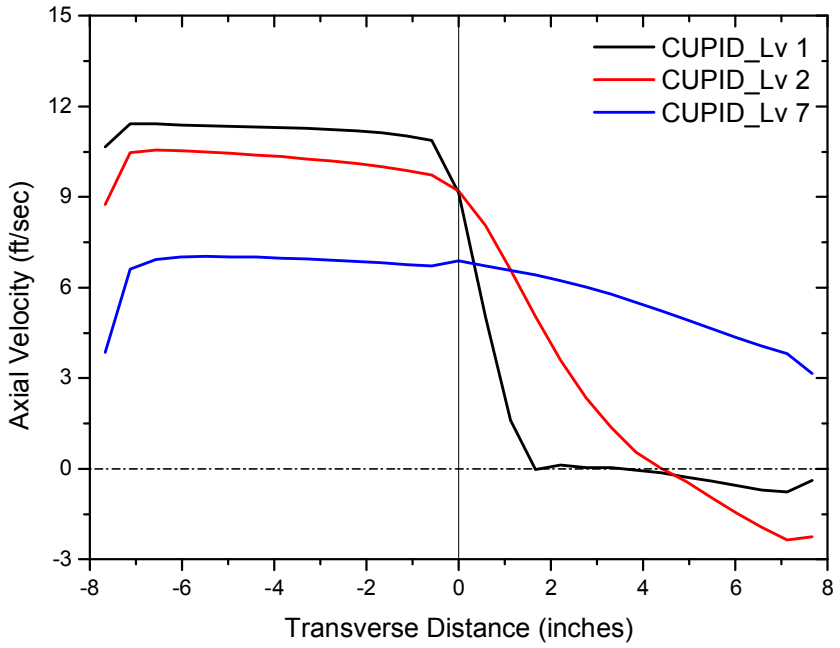

Figure 3.24 Velocity distribution at level 1, 2 and 7 of WH 14x14 full blockage case

3.2 Heated Single-Phase Flow

3.2.1 PNNL 2×6

The PNNL 2x6 test (Bates et al., 1980) was performed at Pacific Northwest National Laboratory in 1977 for investigating the buoyancy effect to flow distributions. In this test, twelve rods had different radial power profile for describing non-uniform power distribution. Velocity and temperature distributions were measured at forced or mixed convection dominant case with changing inlet liquid velocity. Nine windows were positioned at the test section and velocity and temperature data were obtained at window 3 and 7 traversing subchannel 8 to 14. One grid spacer is positioned at the middle of rod bundle. The cross sectional and longitudinal view of test section are presented as Fig.3.25 and Fig. 3.26. Hydraulic diameters at corner, side and center subchannels are 0.0074 m, 0.0086 m and 0.0103 m, respectively. The test was performed at three different cases with changing average inlet velocity, average heat flux and power ratio as indicated in Table 3.8. At the case 1 and 3 are forced convection dominant case, but case 2 is mixed convection dominant case.

In the calculation, the number of computing cells was 504 (3x7x24) with uniform height dividing into 24 meshes. Implemented subchannel models for calculation are given as Table. 3.9. In the non-uniform power distribution conditions, the liquid velocity accelerates at the hot side region by influence of the buoyancy induced flow distribution. There exists no unheated rods in the case 1, and thus, small temperature gradients induce small velocity gradients in rod bundle comparing to other cases. With low inlet velocity in the case 2, the outlet

liquid velocity was calculated almost zero at the cold side region because natural convection was occurred. In this situation, lateral flows are dominant than axial flows, and the velocity calculation results of CUPID at the case 2 show large difference with the calculation results of MATRA which use spatial marching scheme. But in the case 3 with high liquid velocity, forced convection was dominant and there exists relatively small discrepancy between MATRA and CUPID calculation results.

Overall calculation results of CUPID and MATRA show considerable discrepancies with the experimental data. These results might come from the difference of data acquisition methods. Local fluid velocity and temperature were measured at the center of subchannel in the experiment. But codes calculated the cell volume averaged parameters in subchannel. It is hard to evaluate the accuracy of validation results. But, the buoyancy force effect was properly described with CUPID. If there exist higher precision test data under mixed convection, it would be of great use for code validation. The calculated temperature and normalized liquid velocity results at window 3 and 7 in three different test cases are shown as Fig 3.27 to Fig. 3.32.

Table 3.8 Test condition for PNNL 2x6 test

	Pressure (Pa)	Temperature (K)	Average inlet velocity (m/s)	Average heat flux (kW/m^2)	Power ratio (Hot : Cold)
Case 1	101,725	285.15	0.1	18.5	2:1
Case 2	101,725	288.45	0.05	19.7	1:0
Case 3	101,725	289.25	0.1	39.3	1:0

Table 3.9 Applied subchannel models in PNNL 2x6 test validation

	Lateral	Axial	Note
Wall friction		O	Friction factor coefficient Laminar region $f = 64 \times Re^{-1.0}$ Turbulent region $f = 0.184 \times Re^{-0.20}$
Form loss	O		$K_G = 0.5$
Turbulent mixing		O	EV(Equal volume exchange) Model $\beta = 0.005$
Grid spacer		O	Form loss coefficient(K) = 1.0

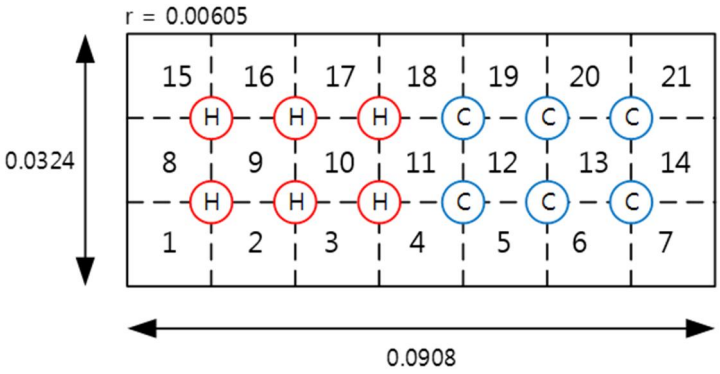

Figure 3.25 Cross sectional view of PNNL 2x6 test section (Unit: m)

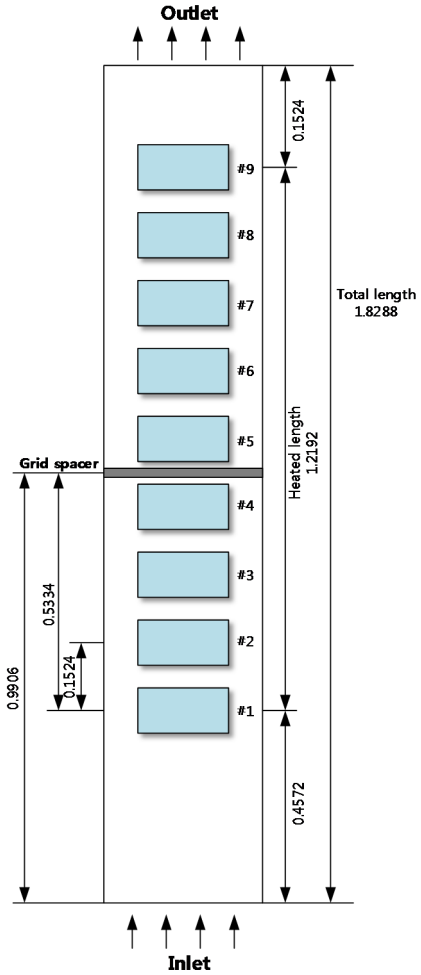

Figure 3.26 Longitudinal view of PNNL 2x6 test section (Unit: m)

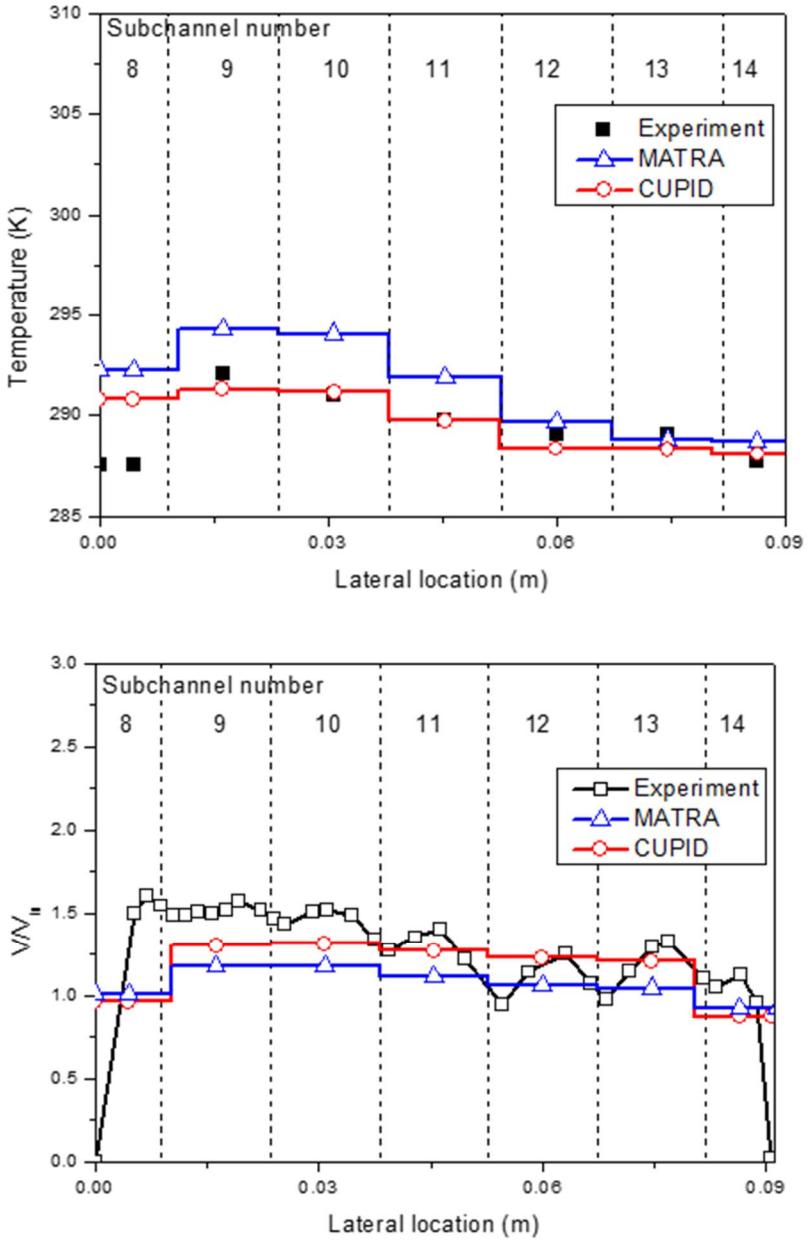

Figure 3.27 Calculated temperature (up) and normalized velocity (down) at window 3 in case 1

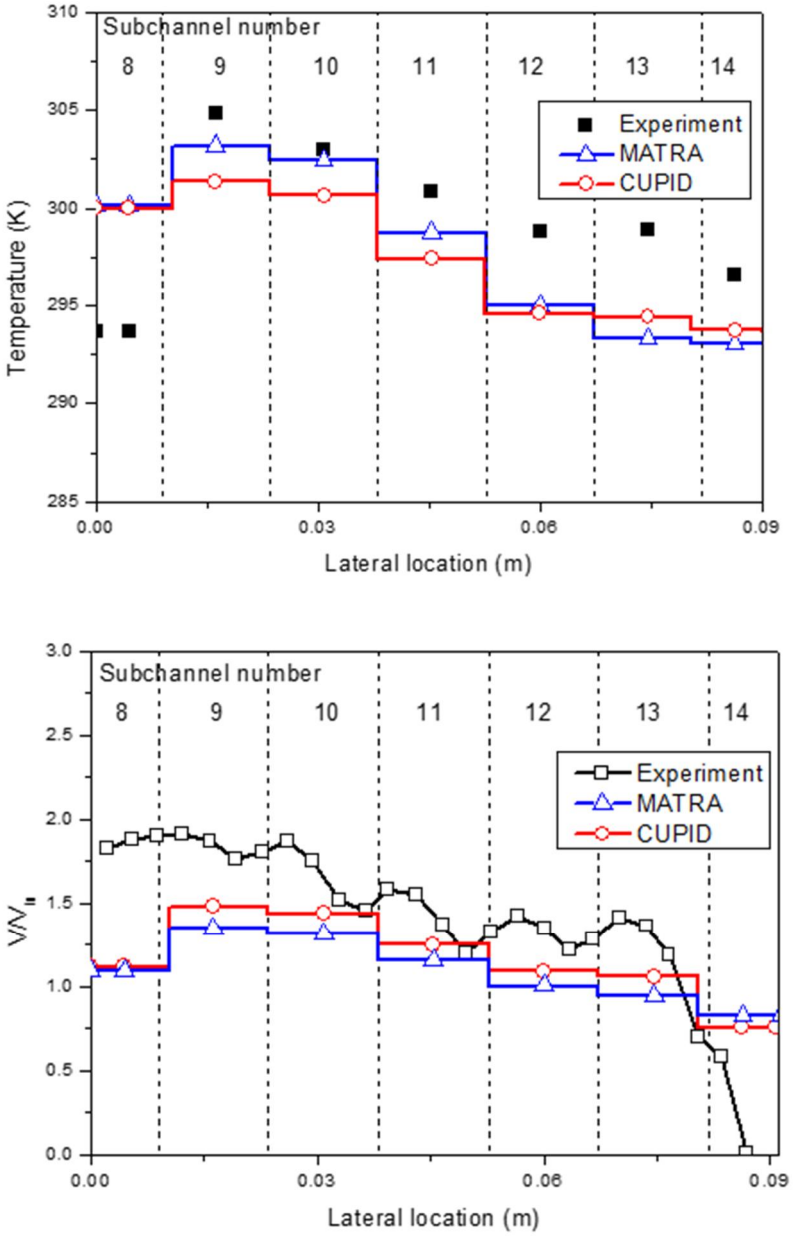

Figure 3.28 Calculated temperature (up) and normalized velocity (down) at window 7 in case 1

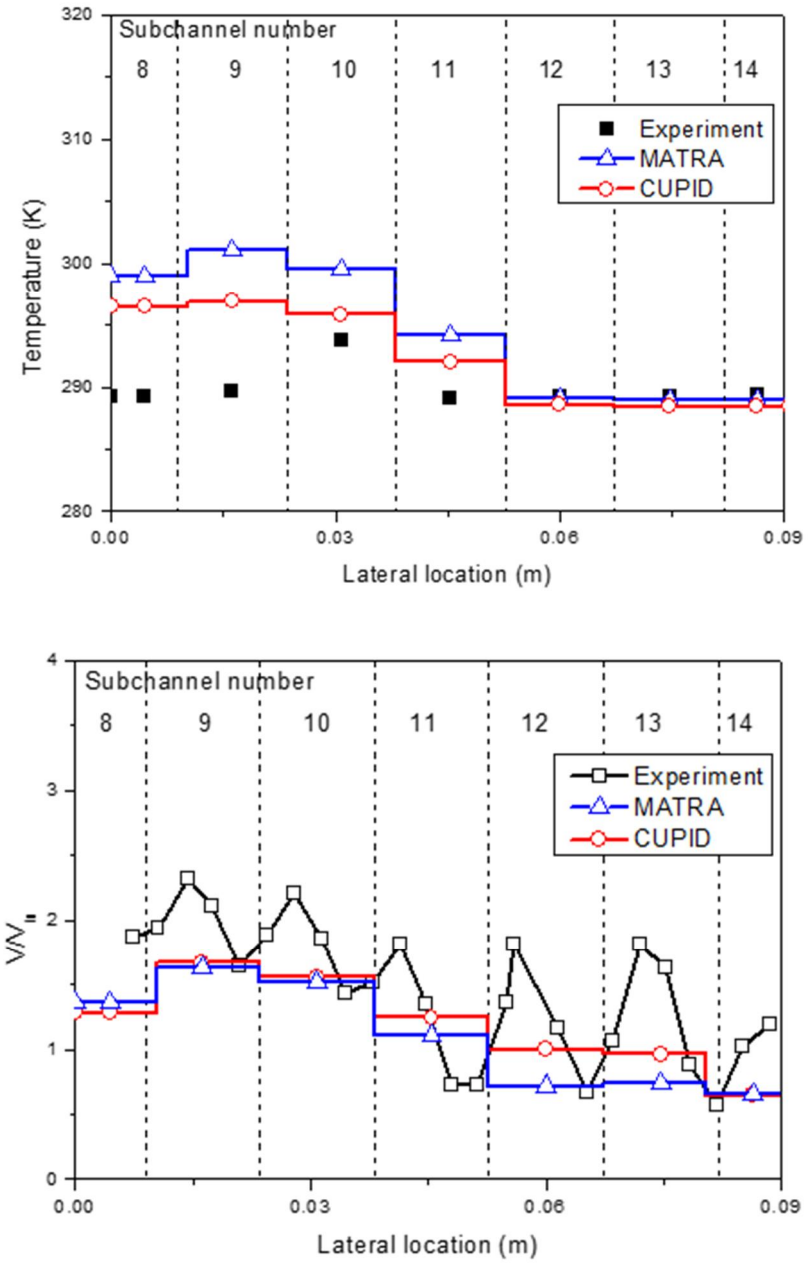

Figure 3.29 Calculated temperature (up) and normalized velocity (down) at window 3 in case 2

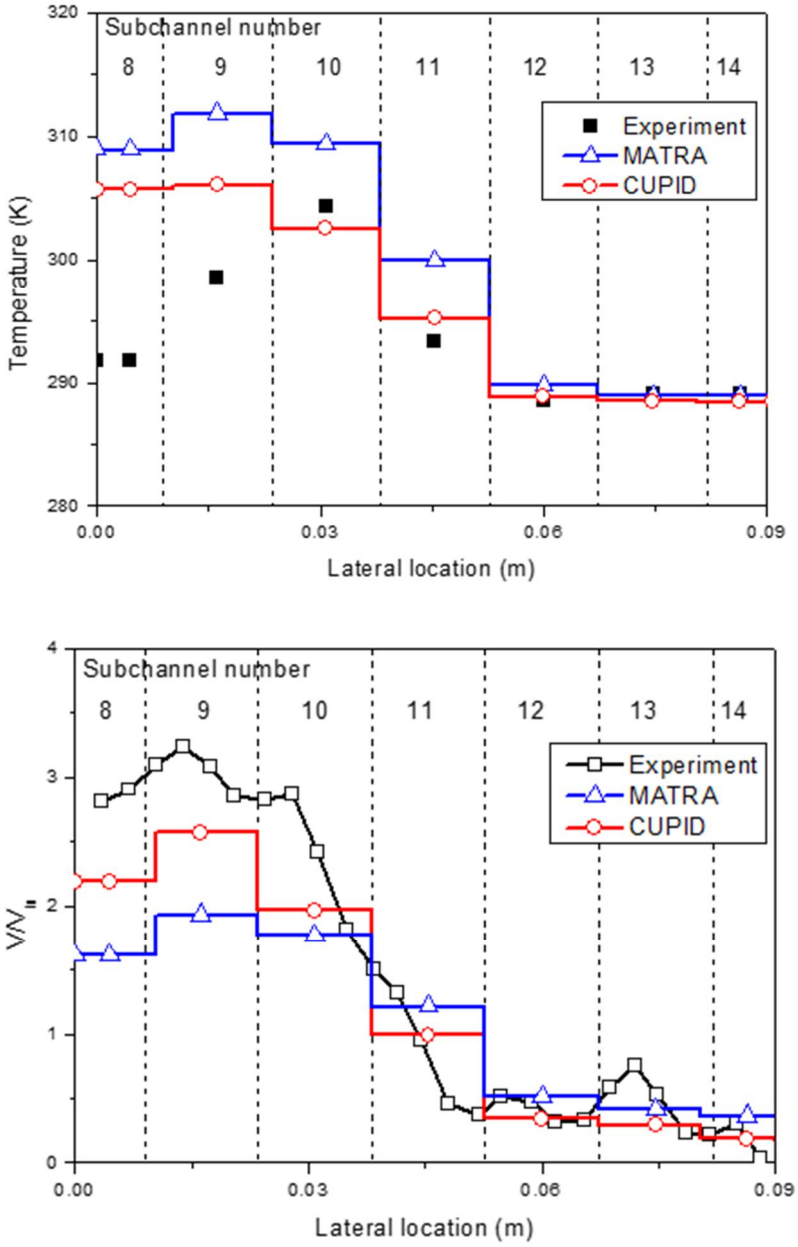

Figure 3.30 Calculated temperature (up) and normalized velocity (down) at window 7 in case 2

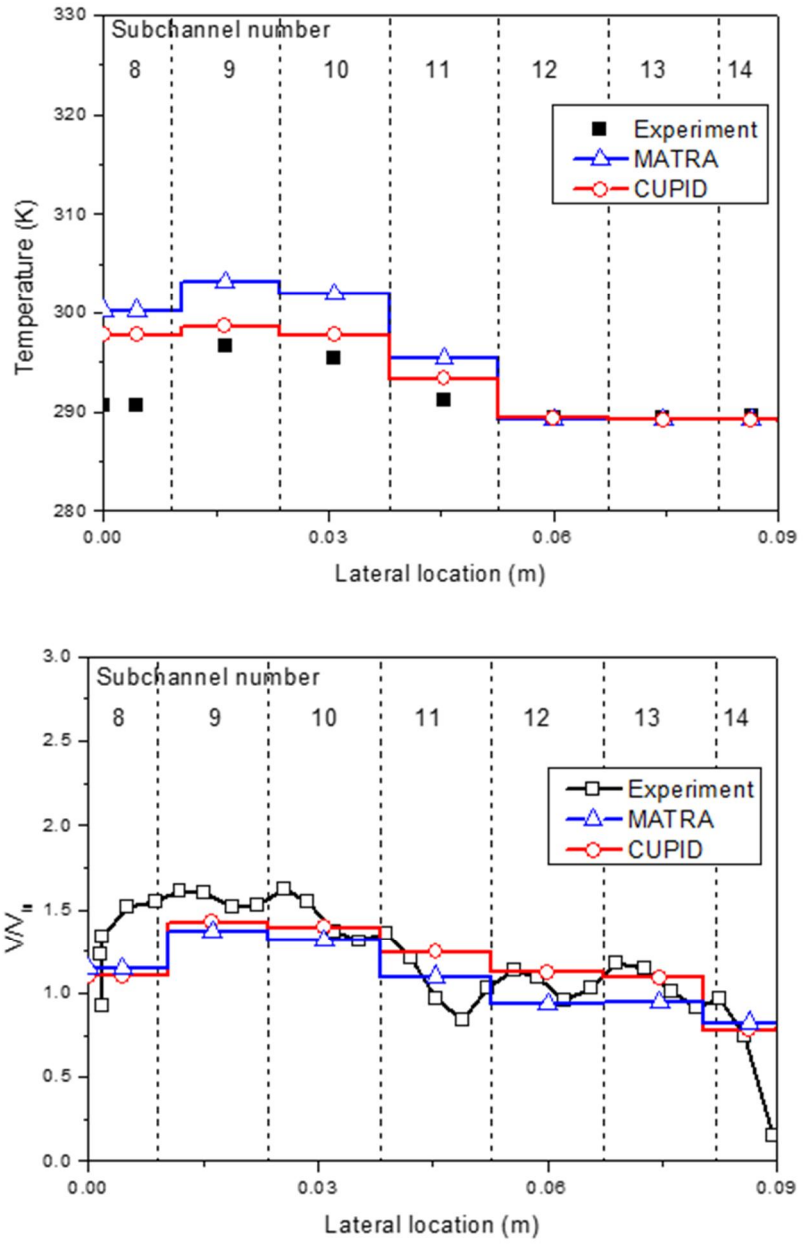

Figure 3.31 Calculated temperature (up) and normalized velocity (down) at window 3 in case 3

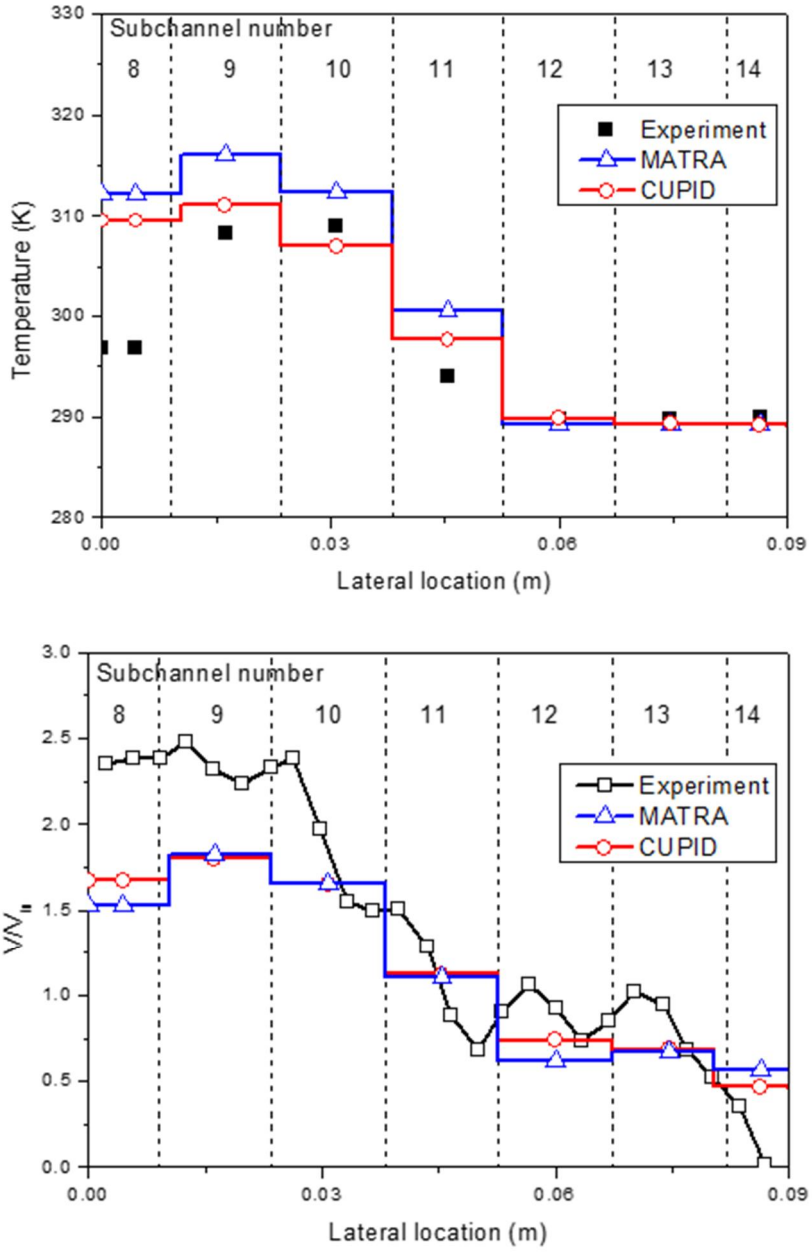

Figure 3.32 Calculated temperature (up) and normalized velocity (down) at window 7 in case 3

3.3 Unheated Two-Phase Flow

In this chapter, validation of CUPID against unheated two-phase flow was performed. This assessment is additionally conducted even if it is not included in the MATRA validation matrix and void drift phenomenon in rod bundle is recently issued by CTF validation. Pang (2014) evaluated the EVVD model in CTF against unheated two-phase flow tests and suggested the new type of Equal Mass exchange turbulent mixing and Void Drift mixing model (EMVD model). For this reason, EVVD model in CUPID was validated against same experiments used in the validation of CTF.

3.3.1 RPI air-water mixing test

The RPI air-water test (Sterner et al., 1983) was issued by NRC (Nuclear Regulatory Commission) and performed at RPI Jonsson engineering center at 1983. The objective of this experiment was to investigate the fully developed two-phase flow distributions at the exit of subchannels. The test section includes a bundle of four unheated rods of 0.0254 m diameter, 0.035 m pitch and the width of assembly is 0.0762 m, height is 0.9144 m. In the test, grid spacer is not positioned in a rod bundle. The mixture of air-water acted as a working fluid and two different methods including sinter section and mixing tee were used to produce two-phase flows. Test loop and cross sectional view of test section were presented in Fig. 3.33 and Fig 3.34, respectively. Hydraulic diameters at corner, side and center subchannels are 0.0158 m, 0.025 m and 0.036 m, respectively.

In the test, void fraction was measured at the outlet of corner, side and center subchannels under various flow conditions; bubbly, slug and churn turbulent flow. Test conditions for each case are presented as Table. 3.10. Bubbly, slug and churn turbulent flow were observed in case 1, 4, case 2, 5, and case 3, 6, respectively.

In the calculation, the number of computing cells was 270 (3x3x30) dividing the channel into 30 meshes with uniform height. The EVVD turbulent mixing model was used for simulating void drift phenomenon. Implemented subchannel models for calculation are given as Table 3.11. For two-phase flow analysis, required constitutive models in CUPID-SG subroutine introduced at chapter 2.3 were activated. For evaluating the effect of the EVVD mixing model, the calculated outlet void fraction distributions with EVVD model and without EVVD model are compared as Fig. 3.35. Without EVVD model, voids were evenly distributed at corner, side and center subchannels and the calculated results of outlet void fraction could not capture a real phenomenon as shown in Fig. 3.37 and Fig. 3.38. But with EVVD model, voids concentrated to the center subchannel which has high mass flux as flows upward. By the effect of EVVD model, the calculation results could capture the experimental data as shown in Fig. 3.39 and Fig. 3.40.

Calculation results of CUPID and CTF show same trend as presented in Fig. 3.41 and Fig. 3.42. The CUPID calculation results with EVVD model could capture the experiment data around 10 % error. From the error comparison results described in Table 3.12, the mixing tee method showed small error than the sinter section method.

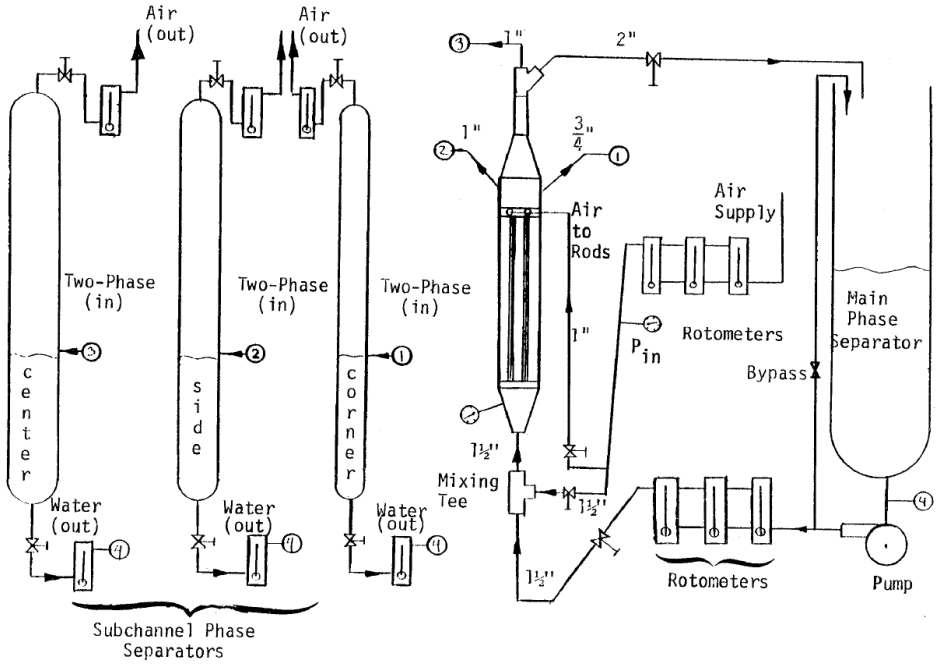

Figure 3.33 Schematic drawing of RPI air-water test loop (Sterner et al., 1983)

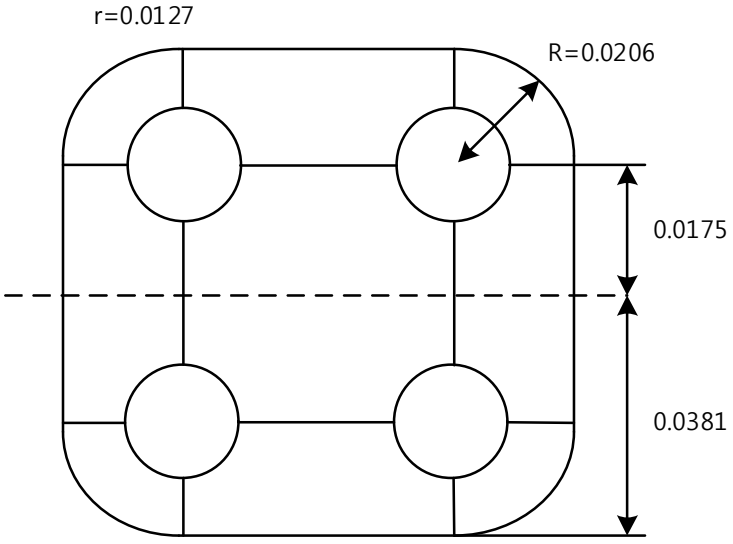

Figure 3.34 Cross section view of RPI air-water test section (Unit: m)

Table 3.10 Test conditions for RPI air-water experiment

Case	Avg. inlet velocity (m/sec)	Quality (%)	Void fraction (%)	Inlet velocity (m/sec)		Pressure in (Pa)	Pressure out (Pa)
				Liquid	Gas		

1	0.451	0.075	20.4	0.569	0.984	142,721.5	135,821.5
2	0.451	0.170	32.8	0.674	1.344	146,168.8	140,598.8
3	0.451	0.359	46.1	0.840	1.906	156,511.0	152,106.0
4	0.903	0.089	23.6	1.185	1.399	208,221.7	200,843.4
5	0.903	0.221	37.5	1.448	1.956	232,353.3	225,936.6
6	0.903	0.539	52.7	1.914	2.780	280,616.6	274,373.2

Table 3.11 Applied subchannel models in RPI air-water test validation

	Lateral	Axial	Note
Wall friction		O	Friction factor coefficient Re<2,300 $f = 64 \times Re^{-1.0}$ 2,300<Re<3×10^4 $f = 0.316 \times Re^{-0.25}$ 3×10^4<Re<10^6 $f = 0.184 \times Re^{-0.20}$
Form loss	O		$K_G = 0.5$
Turbulent mixing		O	EVVD Model $\beta = 0.05,\ K_a = 1.4$
Grid spacer		X	

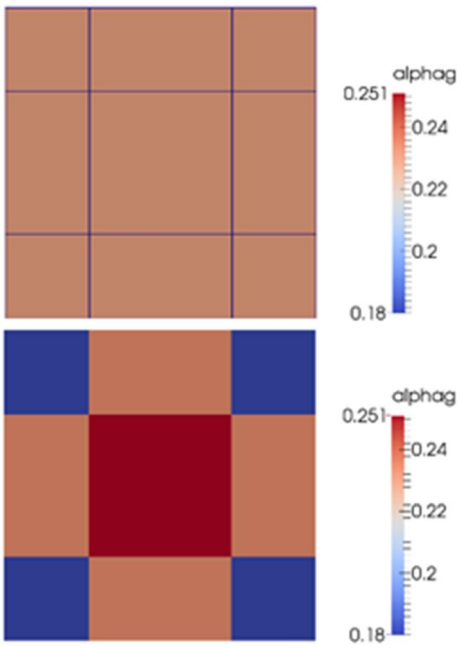

Figure 3.35 Void fraction distribution at the exit of subchannel
(Up: without EVVD model, Down: with EVVD model)

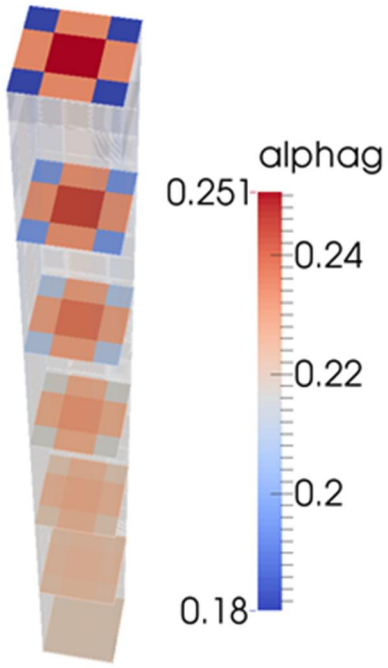

Figure 3.36 Void fraction contour map with EVVD model of RPI air-water test

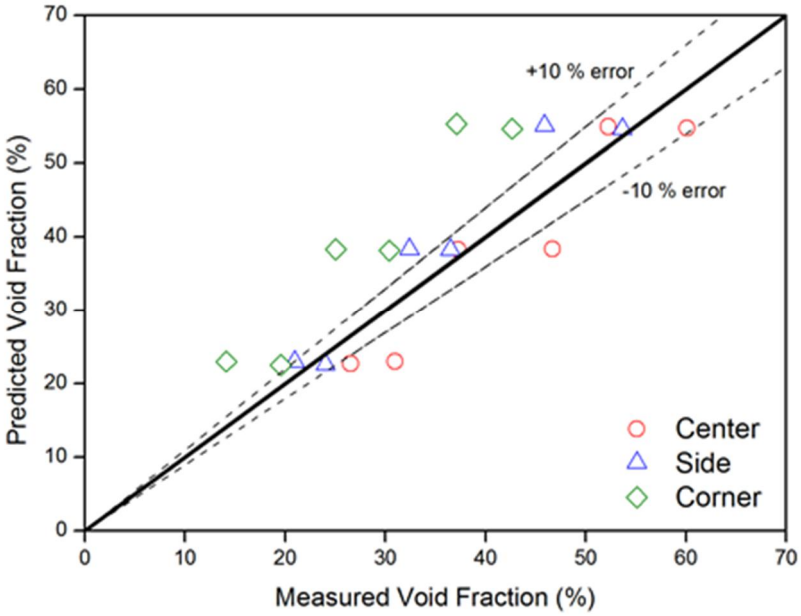

Figure 3.37 Calculated outlet void fraction without EVVD model (Mixing tee)

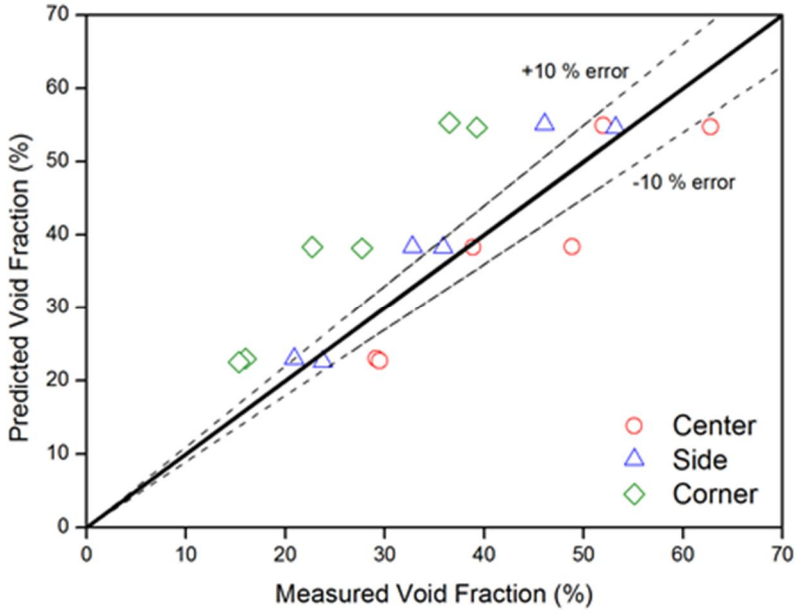

Figure 3.38 Calculated outlet void fraction without EVVD model (Sinter section)

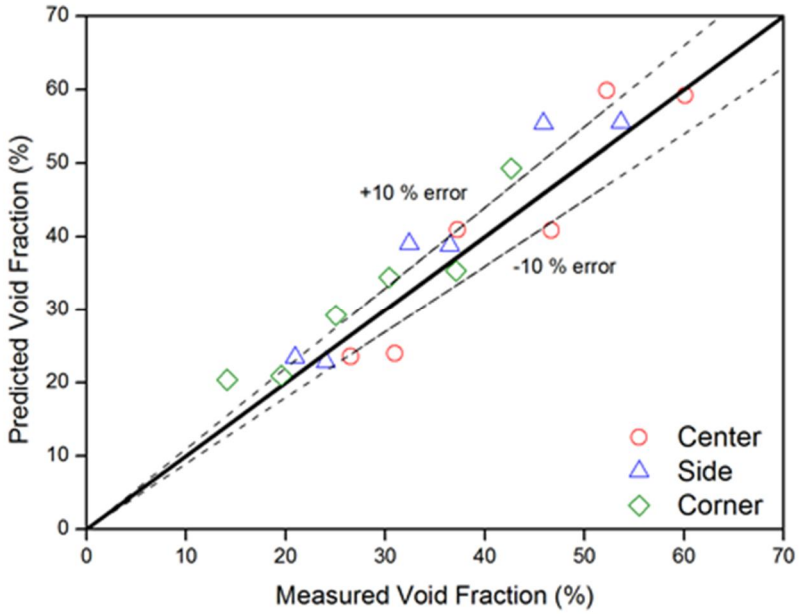

Figure 3.39 Calculated outlet void fraction with EVVD model (Mixing tee)

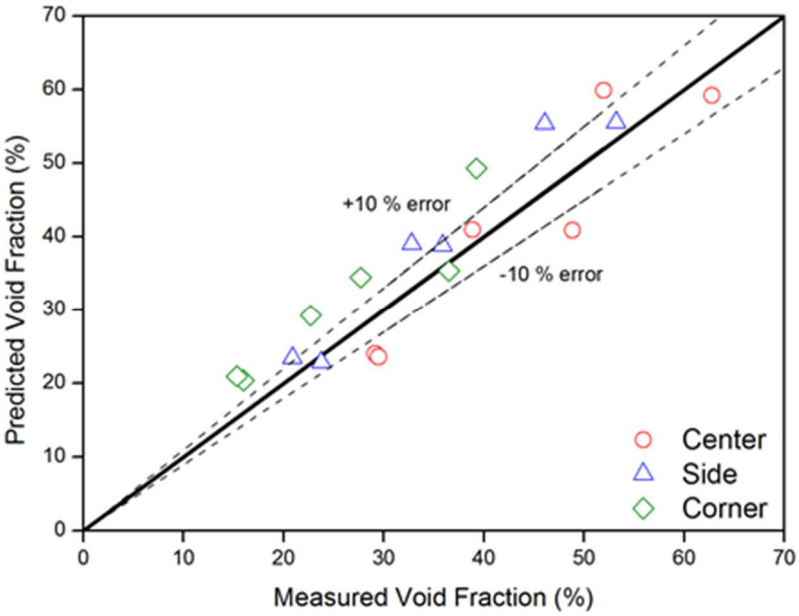

Figure 3.40 Calculated outlet void fraction with EVVD model (Sinter section)

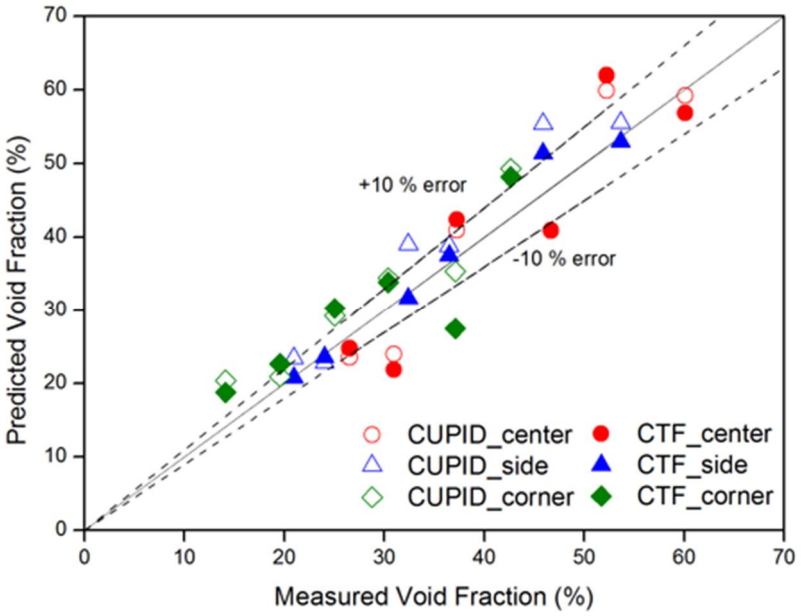

Figure 3.41 Calculated outlet void fraction using CUPID and CTF (Mixing tee)

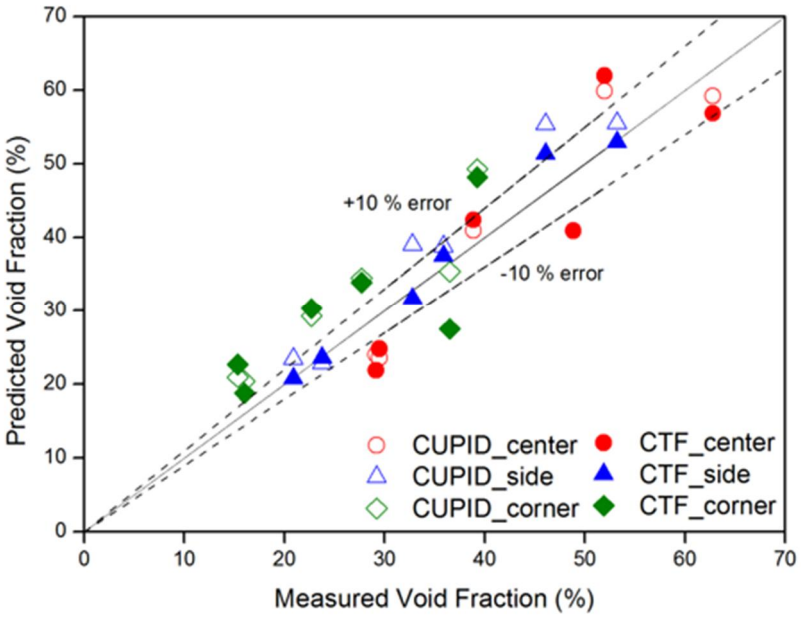

Figure 3.42 Calculated outlet void fraction using CUPID and CTF (Sinter section)

Table 3.12 Relative error of outlet void fraction in RPI air-water test

		CTF-EXP Error (%)	CUPID-EXP Error (%)
Mixing Tee	Bubbly flow	14.6	17
	Slug flow	10.6	13.3
	Churn-turbulent flow	12.7	10.1
Sinter section	Bubbly flow	17.8	19.6
	Slug flow	14.8	17.1
	Churn-turbulent flow	14.7	12.4

3.3.2 Tapucu two-channel test

The Tapucu two-channel test (Tapucu et al., 1994) was performed at Ecole Polytechnique de Montréal in 1988 for investigating the flow mixing effect between two channels at atmospheric pressure and room temperature conditions with asymmetric two phase inlet flow conditions. The height of channel is 1.65 m and the test section height is 1.32 m. The test section consists of two channels of 0.0017 m fuel gap, 0.0072 m hydraulic diameter, and 0.0187 m pitch. The longitudinal and cross sectional views of the test sections are shown in Fig. 3.43 and Fig 3.44, respectively.

In code calculation, 240 (1x2x120) computing cells were used with 120 uniform height meshes. Implemented subchannel models were same with those of the RPI test validation (see Table 3.11) except the value of void drift coefficient K_a set 8. This value was applied based on the calculation results of MARS-vessel in Jeong et al. (2005)'s analysis (Jeong et al., 2005). The test was performed with two cases that have two different asymmetric inlet flow conditions as presented in Table. 3.13.

The void fraction calculation results of CUPID are presented in Fig. 3.45 and Fig 3.46 with comparing the calculation results of MARS-vessel and the experimental data. Following the calculation results, the void drift phenomenon was properly simulated by the effect of EVVD model in annular flow regime. The void fraction at channel 2 increased gradually along axial direction because voids were moved from channel 1 to channel 2 to reduce the gradient of void fraction. The change of void fraction at channel 1 is small because the fluid volume is expanded abruptly by the large pressure drop due to the high mass flux at channel

1. This trend is also observed at the calculation results of MARS-vessel.

Table 3.13 Test conditions for Tapucu two-channel experiment

Case	Void fraction (%)	Inlet velocity (m/s)				Pressure (Pa)
		Ch1, liquid	Ch1, gas	Ch2, liquid	Ch2, gas	
1	58.7	7.2	19.4	3.0	0.0	101,325
2	58.0	7.1	16.4	3.7	6.0	101,325

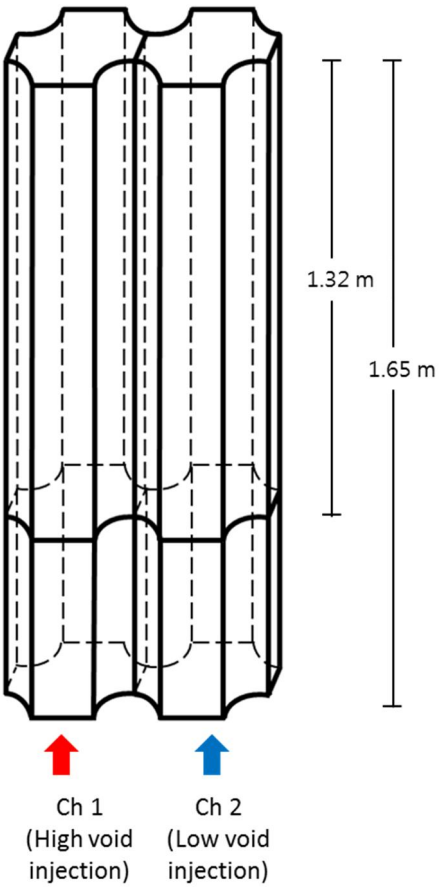

Figure 3.43 Longitudinal view of Tapucu two-channel test section (Unit: m)

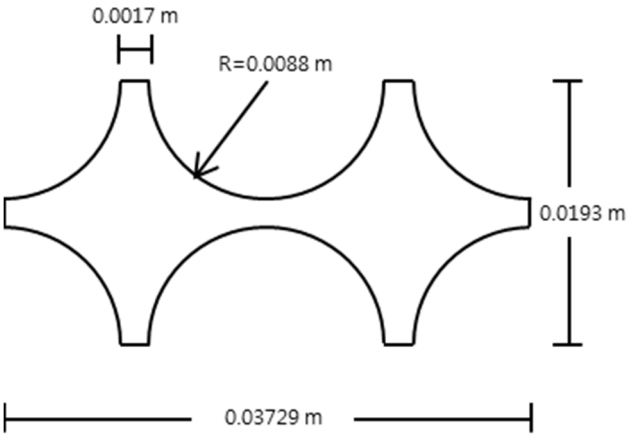

Figure 3.44 Cross section view of Tapucu two-channel test section (Unit: m)

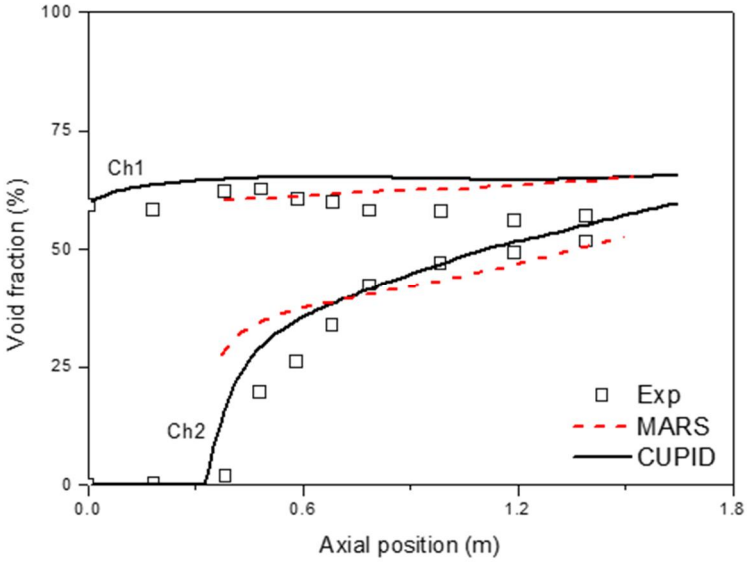

Figure 3.45 Calculated void fraction along axial direction at Tapucu test (Case 1)

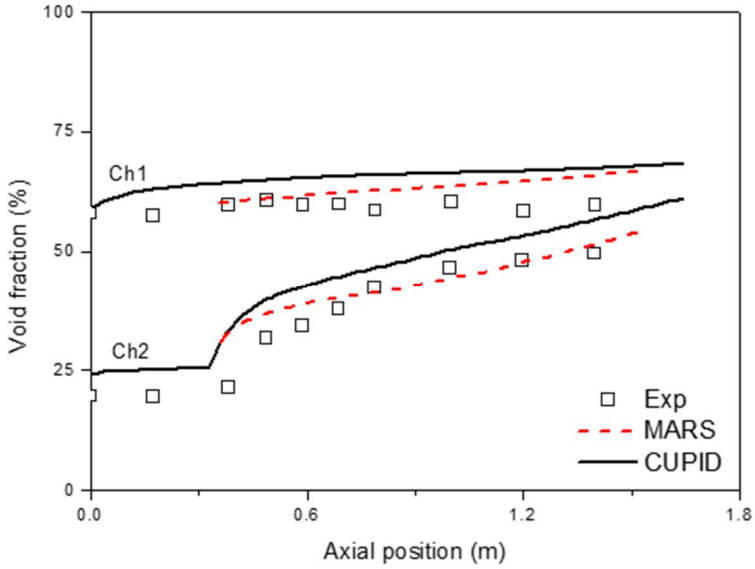

Figure 3.46 Calculated void fraction along axial direction at Tapucu test (Case 2)

3.3.3 Van der Ros two-channel test

The Van der Ros two-channel test (Van der Ros, 1970) was conducted at Technical University Eindhoven in 1970. The objective of this test is same with that of Tapucu two-channel test. The height of test section is 1.85 m and the test section consists of two rectangular channels with hydraulic diameter 0.0099 m. The longitudinal and cross sectional views of the test sections are shown in Fig. 3.47 and Fig 3.48, respectively. In this validation, only the case 1 which shows bubbly flow regime was analyzed with CUPID (note that Tapucu test condition was annular flow regime). The test was performed at atmospheric pressure and room temperature conditions with asymmetric two phase inlet flow condition as shown in Table. 3.14.

In the calculation, the number of computing cells was 58 (1x2x29) with uniform height of 29 meshes. Implemented subchannel models were same with those of the RPI test validation (see Table 3.11) except the sign of void drift coefficient K_a set +1.4 or -1.4 for evaluating the effect of coefficient sign.

Following the calculation result, void drift mechanism explained at chapter 2.2.3 can be confirmed. The lift force acting on bubbles would be opposite to the velocity gradient because the flow condition is bubbly flow regime with small bubble hydraulic diameter, 0.0099 m. Accordingly, bubbles would be forced to move to channel 2 which has smaller mass flux. As a result, as shown in Fig. 3.49, CUPID could capture the experimental data more accurately with negative value of void drift coefficient K_a.

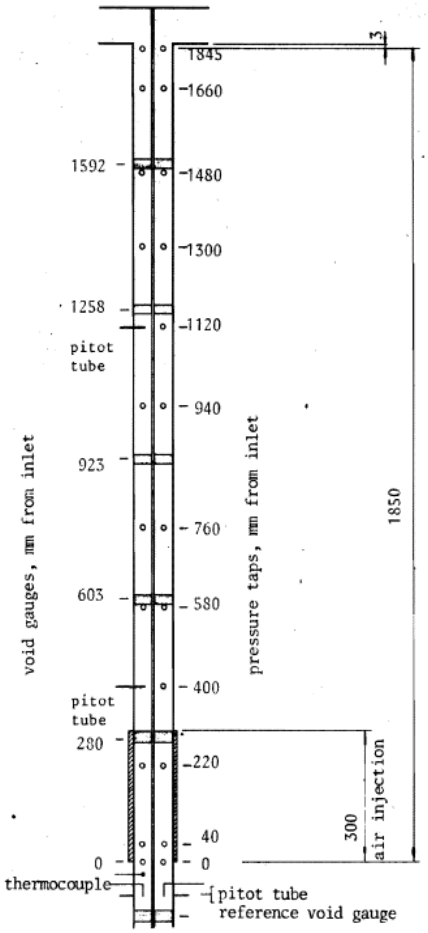

Figure 3.47 Longitudinal view of Van der Ros test section (Unit: mm)
(Van der Ros, 1970)

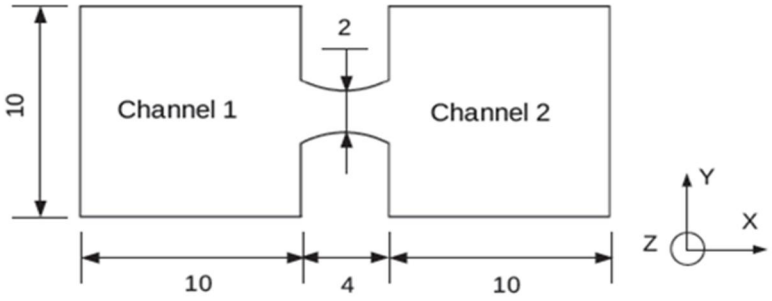

Figure 3.48 Cross section view of Van der Ros test section (Unit: mm)
(Van der Ros, 1970)

Table 3.14 Test conditions for Van der Ros two-channel experiment

Case	Void fraction (%)	Inlet velocity (m/s)				Pressure (Pa)
		Ch1, liquid	Ch1, gas	Ch2, liquid	Ch2, gas	
1	22.0	0.9	1.1	0.7	0.0	101,330

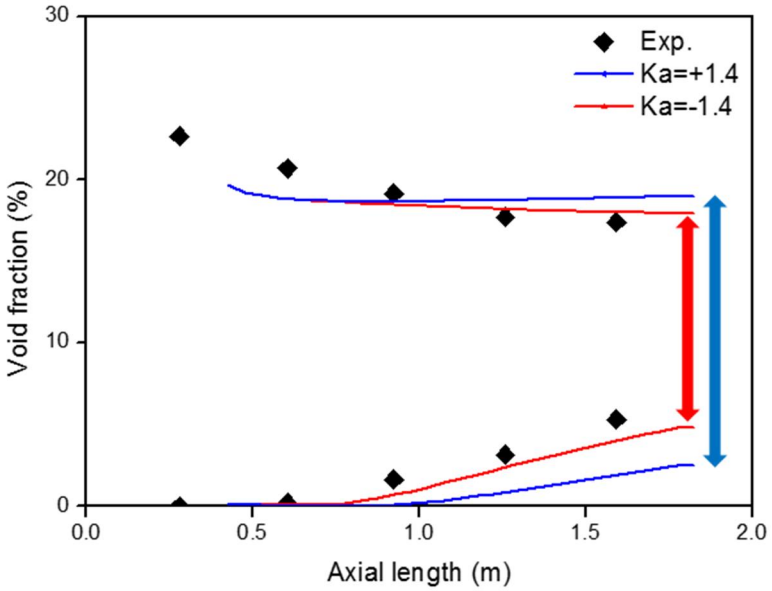

Figure 3.49 Calculated void fraction along axial direction at Van der Ros test

3.4 Heated Two-Phase Flow

3.4.1 GE 3×3

The GE 3x3 test (Lahey et al., 1970) was conducted at General Electric Company in 1970. The quality and mass flux were measured at the outlet of corner, side and center subchannels in two-phase boiling conditions with uniformly heated nine rods. The test section consists of nine heated rods of 0.0145 m diameter, 0.0188 m pitch and the assembly width and height are 0.0588 m and 3.048 m, respectively. Eight grid spacers are positioned in a rod bundle. The longitudinal and cross sectional view of test section are presented in Fig. 3.50 and Fig. 3.51, respectively. The test was performed with uniform radial and axial power profiles, and the length of heated region is 1.828 m at the exit of test section. Hydraulic diameters at corner, side and center subchannels are 0.0069 m, 0.0113 m and 0.0164 m, respectively.

The experiment was conducted against thirteen different test conditions with varying power, temperature and inlet fluid velocity as indicated in Table 3.15. In the calculation, the number of computing cells with 61 uniform height meshes was 976 (4x4x61). The EVVD turbulent mixing model was used for simulating void movement and applied subchannel models are presented in Table. 3.16. Also, required constitutive models for analyzing two-phase flow were used from CUPID-SG subroutine.

In this calculation, the void fraction in the rod bundle was gradually increased by heating rods. CUPID could properly simulate the continuous change of flow regime, from single phase to annular flow. In Fig. 3.52 and Fig. 3.53, the

outlet quality and mass flux calculation results of CUPID are compared with the calculation results of MATRA, CTF and the experimental data. Overall calculation results of CUPID, CTF and MATRA properly described the real phenomenon. However, in the case of mass flux, the calculation results of CUPID and CTF which use two-fluid model for two-phase flow analysis showed better agreement with experimental data than the calculation results of MATRA which uses homogeneous model. These differences were clearly observed in low mass flux region at the corner subchannel than the side or center subchannel. The maximum error of the predicted to measured data ratio (P/M) and the difference between predicted and measured data (P-M) about outlet mass flux and quality are described in Table 3.17 and Table 3.18, respectively. It can be noticed that the maximum error appears at the corner subchannel. In the case of corner mass flux results, CUPID shows 31 % error which has the averaged value of the predicted MATRA and CTF errors.

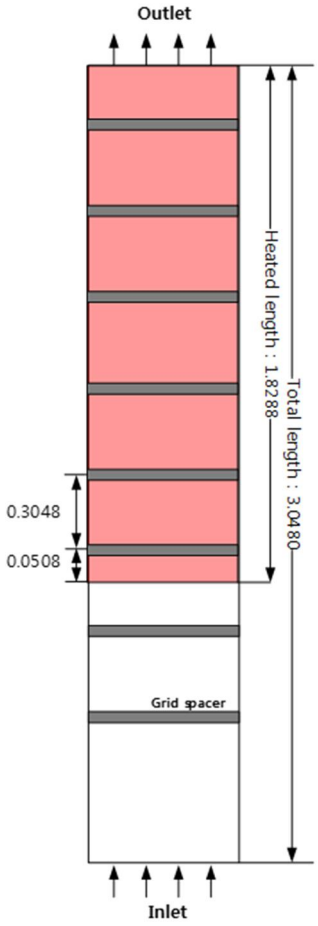

Figure 3.50 Longitudinal view of GE 3x3 test section (Unit: m)

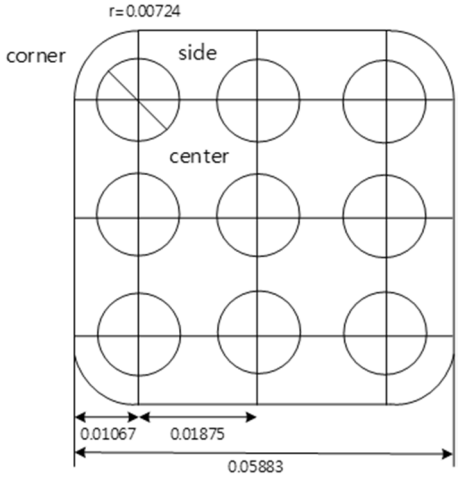

Figure 3.51 Cross section view of GE 3x3 test section (Unit: m)

Table 3.15 Test conditions for GE 3x3 experiment

Case	ID	Power	Temperature	Velocity	Pressure
		kW	K	m/sec	MPa
1	2B2	532	486	0.84	6.90
2	2B3	532	507	0.85	6.90
3	2B4	532	534	0.85	6.90
4	2C1	532	532	1.68	6.90
5	2C2	532	542	1.69	6.90
6	2D1	1064	428	0.86	6.90
7	2D3	1064	499	0.86	6.90
8	2E1	1064	490	1.71	6.90
9	2E2	1064	513	1.71	6.90
10	2E3	1064	545	1.68	6.90
11	2G1	1596	446	1.70	6.90
12	2G2	1596	465	1.71	6.90
13	2G3	1596	488	1.70	6.90

Table 3.16 Applied subchannel models in GE 3x3 test validation

	Lateral	Axial	Note
Wall friction		O	Friction factor coefficient $f = 0.184 \times Re^{-2.0}$
Form loss	O		$K_G = 0.5$
Turbulent mixing		O	EVVD Model $\beta = 0.05,\ K_a = 1.4$
Grid spacer		O	Form loss coefficient(K) = 1.0

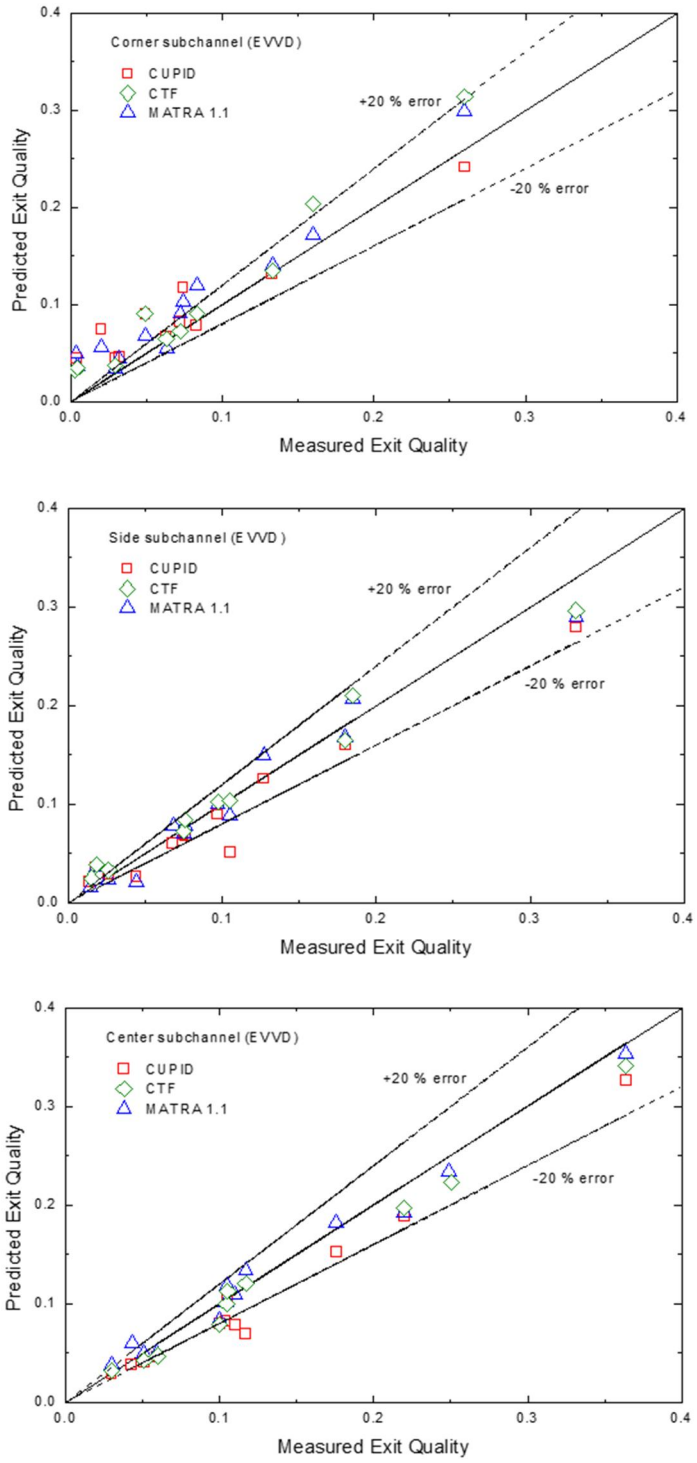

Figure 3.52 Calculated outlet quality (corner, side and center subchannels) at GE 3x3 test

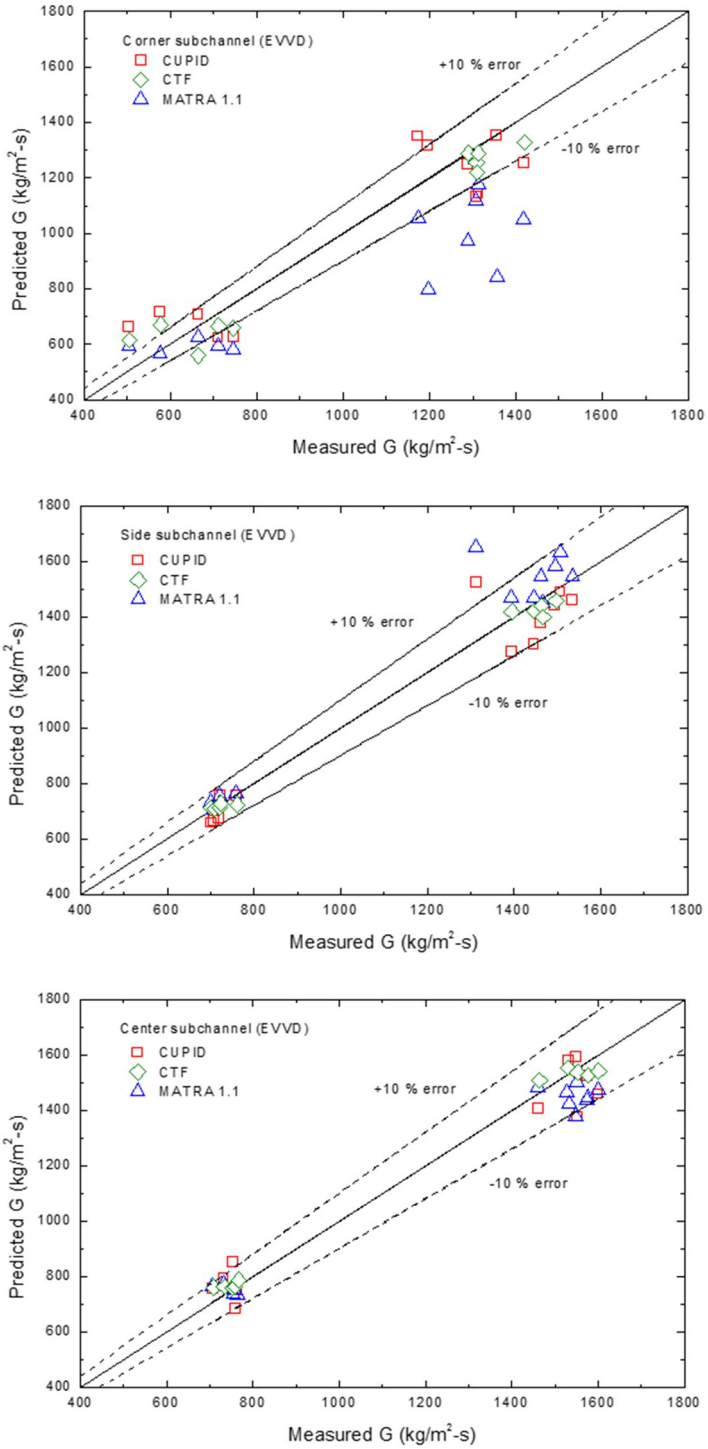

Figure 3.53 Calculated outlet mass flux (corner, side and center subchannels) at GE 3x3 test

Table 3.17 Maximum error of predicted/measured data (P/M, %) about outlet mass flux at GE 3x3 test

		MATRA (P/M)	CTF (P/M)	CUPID (P/M)
Mass flux	Corner	38	22	31
	Side	26	5	16
	Center	11	7	13

Table 3.18 Maximum error of predicted-measured data (P-M) about outlet quality at GE 3x3 test

		MATRA (P-M)	CTF (P-M)	CUPID (P-M)
Quality	Corner	0.047	0.054	0.055
	Side	0.023	0.025	0.018
	Center	0.017	0.007	0.003

Chapter 4.

Subchannel Scale Full Core T/H Analysis

4.1 Parallel Solver Performance Test

Preliminary calculation of subchannel scale full core T/H analysis for the simplified OPR1000 reactor core was performed by CUPID. The objective of calculation is to evaluate the full core simulation capability of CUPID and the performance of its parallel solver. The number of computing cells to each processor is uniformly divided and shared memory for parallel execution. CUPID code is parallelized with Message Passing Interface (MPI) parallel solver for computing heavy calculations like full core scale simulation. The geometry of OPR1000 reactor core was simplified that every fuel assembly consist of 16x16 rod array without consideration of guide tube, water gap, shroud and grid spacer. The number of fuel assemblies in OPR1000 is 177 and total number of fuel rods are 45,312 (16x16x177) with 0.0095 m diameter, 0.0129 m pitch and 3.81 m active height. In the calculation, the number of computing cells was about one million with 20 uniform axial height meshes. The detailed geometry parameters are given as Table 4.1.

The calculation conditions were same with the OPR1000 operating conditions of pressure (15.5 MPa), temperature (569 K), and inlet velocity (5.1

m/s). In this preliminary calculation, asymmetric inlet velocity conditions were applied at the half of the right side core (6.63 m/s) and the other left side core (3.57 m/s), respectively. The calculated pressure drop and flow distributions by the effect of the cross flow and turbulent mixing models were properly simulated with CUPID as shown in Fig. 4.1 and Fig. 4.2.

The CUPID runs were made on a 4 node LINUX clusters each of which uses Dual Intel® Xeon® E5-2600 CPUs which can make use of 20 processors simultaneously. With increasing the number of CPU processors 20 to 100, parallel solver performance in CUPID was tested. The calculation was run for a total of 1 second in the problem time with 0.018 time interval and the steady state reached after 0.3 second of the problem time. With using 100 CPU processors, total wall clock time to complete the calculation was about 38.5 seconds. For evaluating the parallel solver performance, the scalability is defined as follows:

$$Scalability = \frac{Total\ wall\ clock\ time\ with\ one\ processor}{Total\ wall\ clock\ time\ with\ \#\ n\ processor}$$

The ideal scalability and scalability of all cases by the number of processors are drawn at Fig. 4.3. Following the results, improvement and optimization of parallel solver in CUPID are necessary for high performance of parallel computing.

Table 4.1 Main parameters for simplified OPR1000 calculation

Main Parameters	
Number of fuel assemblies	177
Number of fuel rods	45,312 (16×16×177)
Hydraulic diameter	0.0126 m
pitch	0.0129 m
Active height	3.81 m
Number of axial grids	20
Number of total grids	1,023,060 (17×17×177×20)

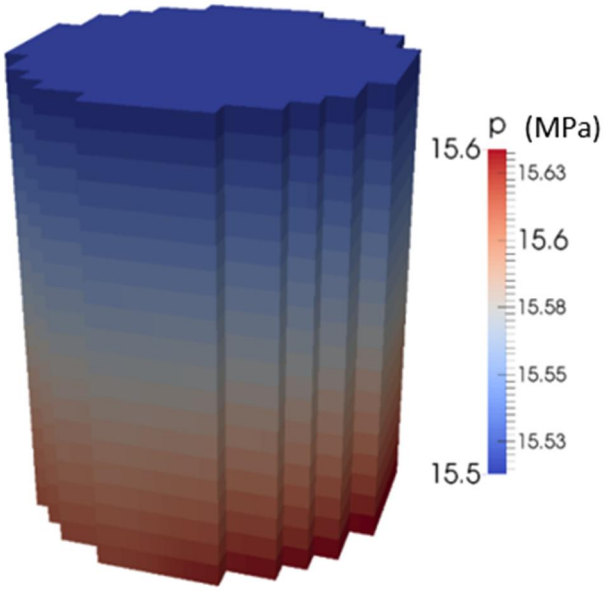

Figure 4.1 Pressure drop calculation results of simplified OPR1000

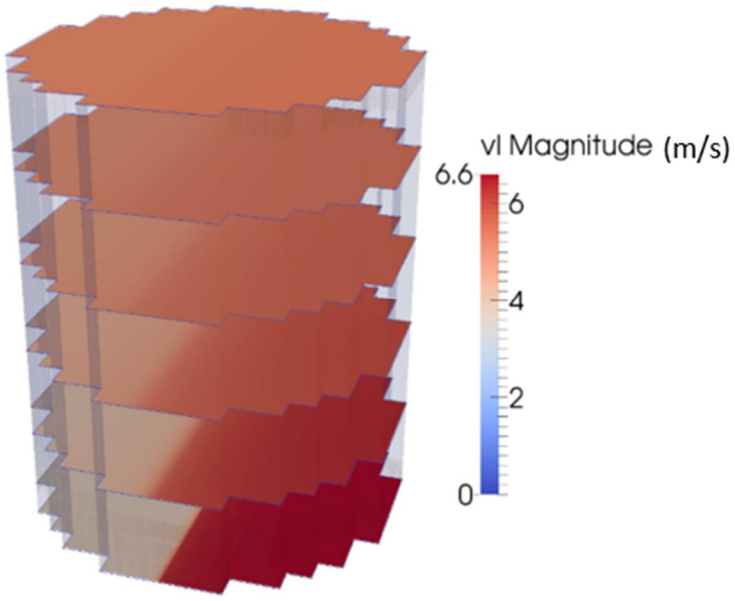

Figure 4.2 Axial velocity contour map of simplified OPR1000

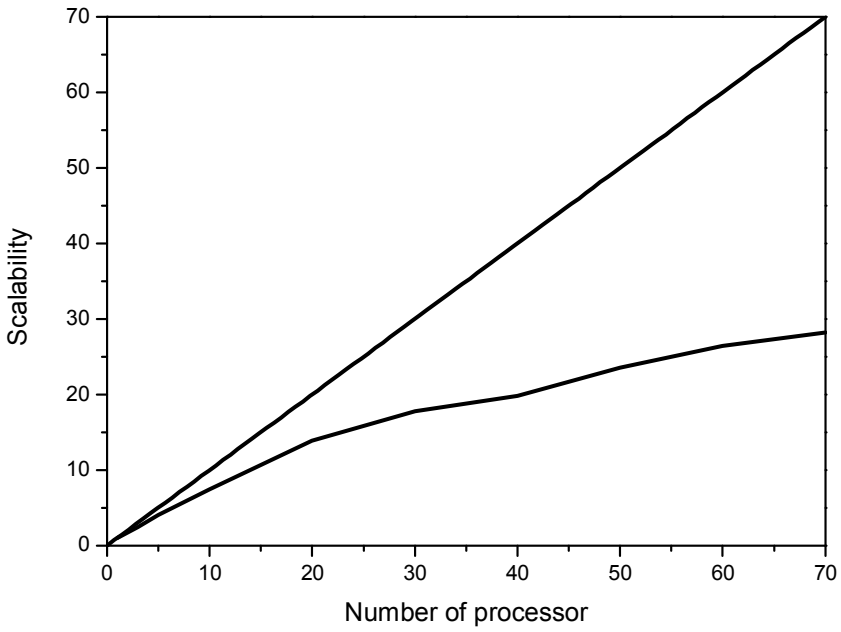

Figure 4.3 Scalability results of simplified OPR1000 calculation

4.2 Demonstration of cycle 1 HFP (Hot Full Power) state of APR1400

The subchannel scale full core T/H analysis target for APR1400 (for Advanced Power Reactor 1400 [MWe]) reactor was performed using CUPID code. The demonstration was performed for cycle 1 hot full power state of Shin Kori unit 3. For high fidelity T/H simulation of APR1400 reactor core, detailed geometry features and individual rod power distributions from the neutronics code, nTRACER (Jung et al., 2013), were considered in this calculation.

4.2.1 Subchannel scale full core modeling

The reactor core of APR1400 consists of 241 fuel assemblies and each of fuel assembly is composed of 16x16 rod array including 236 fuel rods and 5 guide tubes. The inter-assembly water gap and the core shroud were modeled in the calculation for a faithful representation of reactor core as shown in Fig. 4.4. The reactor core includes 56,876 fuel rods which diameter and pitch are 9.5 mm and 12.9 mm and the width and active height of the fuel assembly are 0.2056 m and 3.81 m, respectively. The hydraulic diameter is 12.6 mm and the total flow area is 5.8 m^2. In accordance with the detailed geometry features of reactor core, all computing cells were characterized into 13 different subchannel types as shown in Fig. 4.5. The subchannel types contain assembly, guide tube, shroud and water gap as shown in Table 4.2. The required geometry information such as porosity, permeability, hydraulic diameter and gap size was demonstrated following subchannel types.

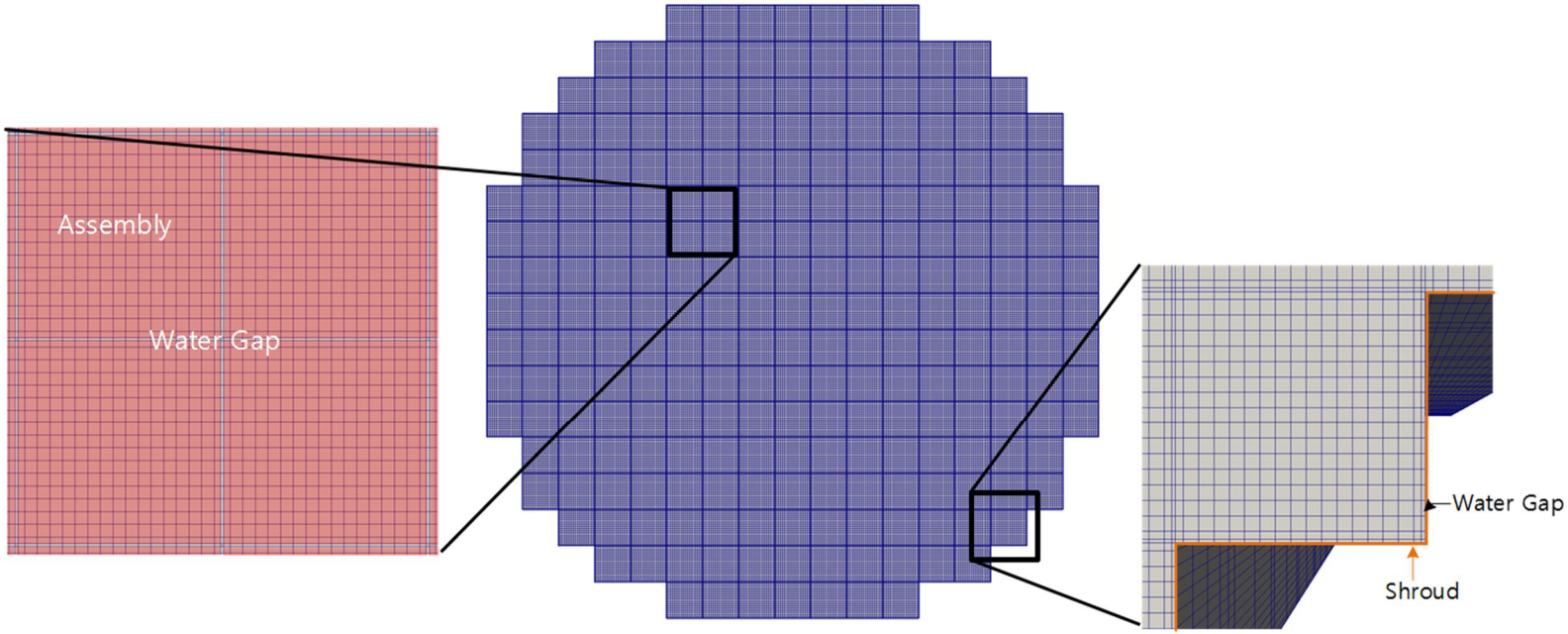

Figure 4.4 Features of APR1400 subchannel scale reactor core

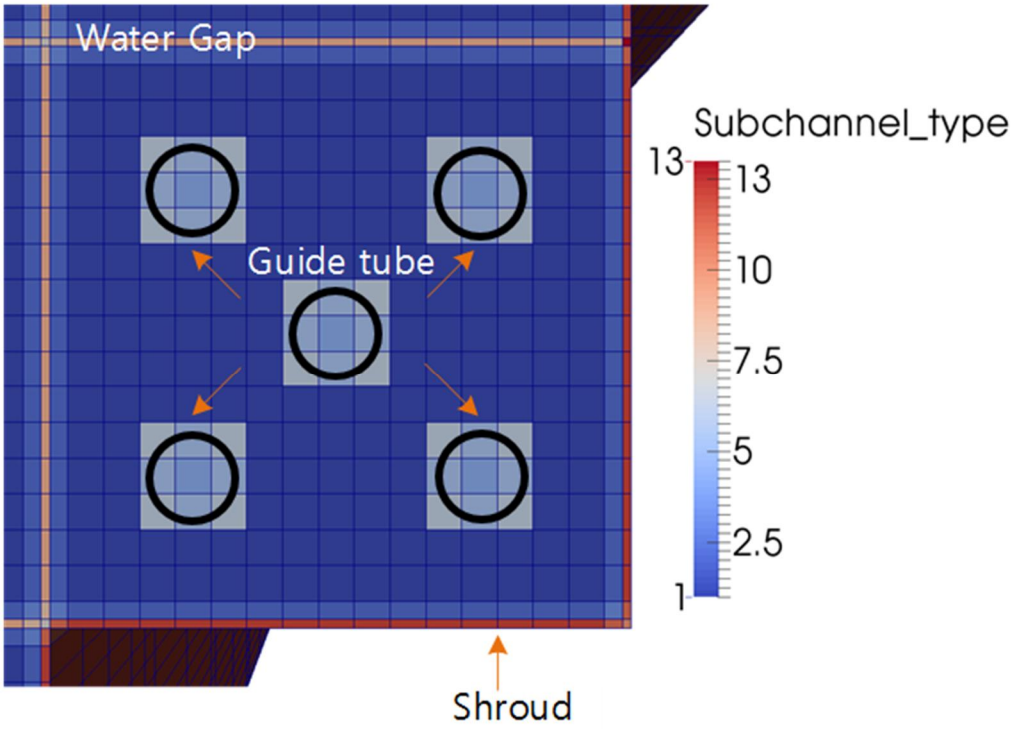

Figure 4.5 APR1400 subchannel type definition

Table 4.2 APR1400 subchannel type definition

Type	Name
1	Assembly (center)
2	Assembly (side)
3	Assembly (corner)
4	Guide tube (center)
5	Guide tube (side)
6	Guide tube (corner)
7	Water gap (center)
8	Water gap (corner)
9	Water gap (side)
10	Shroud (edge)
11	Shroud (near edge)
12	Shroud (side wall)
13	Shroud (between gap)

4.2.2 Implementation of power distribution

For describing the detailed core power distributions, individual rod power distributions from the neutronics code, nTRACER, were applied to the CUPID simulation. The neutronics code calculation was performed for the condition of 1083.76 ppm critical boron concentration at hot full power steady state. The average output power per assembly was 16.53 MW. For axial direction, the calculation was conducted with 33 non-uniform height meshes in consideration of the location of grid spacers.

For applying the individual rod power to each subchannel, it was required to designate the connectivity between subchannels and rods. The indexing process of whole core assembly and subchannel were conducted as shown in Fig. 4.6 and Fig. 4.7, respectively. The numbering of fuel rods loaded in an assembly is presented in Fig. 4.7. The rod power of fuel rods positioned at the location of guide tube (rod number 52, 53, 68 and 69, etc.) set to be zero. Each subchannel contains a quarter of one, two or four fuel rods. Therefore, the loaded power to each subchannel was obtained by the subchannel to rod connectivity and applied to CUPID for a high fidelity calculation.

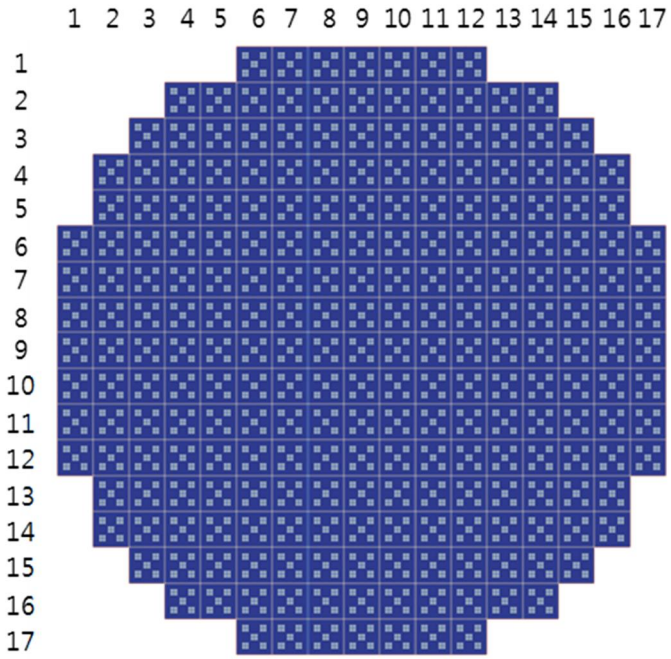

Figure 4.6 Assembly indexing scheme in APR1400

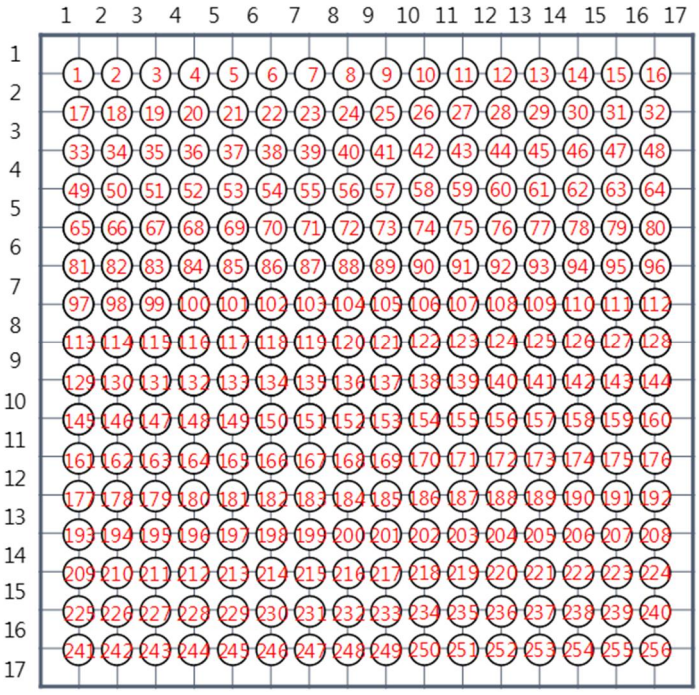

Figure 4.7 Subchannel indexing scheme in APR1400

4.2.3 Full core T/H simulation of APR1400

The demonstration was performed for cycle 1 hot full power steady state of Shin Kori unit 3. The calculation was conducted for Shin Kori unit 3 normal operation conditions as given in Table 4.3. In the calculation, the number of computing cells was 2,675,698 with non-uniform height of 34 meshes (note that one ghost cell was added at the outlet). It was assumed that 99 % area reduction occurred at a center cell of guide tube region composed of nine computing cells. Also, the geometry change of the other eight computing cells which were included in the guide tube region was taken into account with different porosities and hydraulic diameters. For considering the wall friction at the water gap, one imaginary cell which includes a water gap and the neighboring side or corner assembly subchannels was adopted and the value of hydraulic diameter was obtained from one imaginary cell. Therefore, the calculated hydraulic diameters at the side or corner assembly subchannels were different between near water gap and near shroud. Input hydraulic diameters for each subchannel type and subchannel models applied for this simulation are given at Tables. 4.4 and 4.5, respectively.

The number of computing cells to each processor was evenly distributed by METIS (Karypis and Kumar, 1998) program. By this program, it is possible to perform efficient calculation with achieving adequate computational load balancing. The number of computing cells to each processor was about 53,514 with using 50 processors. The 3D view of assigned computing cells to each processor is shown in Fig. 4.8. The CUPID runs were made on a LINUX cluster each of which used Dual Intel® Xeon® E5-2600 CPUs. The calculation was run for a total of 1.5 second in the problem time and the total wall clock time to

complete the calculation was about 1 h 29 min with the 50 processors. In this calculation, the maximum number of available processors was 50 due to the limitation in memory. It is expected to use more processors to improve calculation performance and to reduce the computing time.

The axial contour maps of the implemented core power distributions and the calculation results of coolant temperature distributions are presented in Fig. 4.9 and Fig. 4.10, respectively. Following the result of Fig. 4.9, core power distributions were properly implemented as a cosine shape for axial direction. By influencing of the implemented power, the increased coolant temperature was properly simulated by CUPID as shown in Fig. 4.10. The 3D view of the full core calculation results is presented in Fig. 4.11. In the figure, the left side represents the calculated coolant temperature distributions and the right side represents the implemented power density distributions.

Also, the coolant velocity distributions were calculated and presented in Fig. 4.12. The acceptable calculation results including low velocity at guide tubes which had high fluid resistance and high velocity at water gaps which had low fluid resistance could be obtained. In this calculation, it was possible to calculate the desired parameters at the specific parts because all computing cells were characterized into 13 different subchannel types. For example, the bypass flow fraction to shroud and water gap was calculated about 0.687 %.

Additionally, the calculation result of DNBR at each subchannel is presented in Fig. 4.13. For obtaining minimum value of DNBR, it is required to use the proper CHF correlation which considers the geometry features of APR1400 core. However, the Biasi correlation (Biasi et al., 1967) was used in this work, because the CHF correlation for APR1400 is confidential and not published in open

literature. Therefore, the objective of this calculation is not the estimation of minimum DNBR but demonstration of the capability to predict the MDNBR. At the case of the actual heat flux, the largest heat flux on a rod which loaded in a subchannel was used for conservative calculation. The Biasi correlation consists of two equations, one for low quality CHF and the other for high quality CHF as given below:

$$q''_{B1} = (5.9691 \times 10^6) G^{-1/6} \left(F(P) G^{-1/6} - X\right) {D_H}^{-n}$$

$$q''_{B2} = (11.98 \times 10^6) H(P)(1 - X) {D_H}^{-n} G^{-0.6} \qquad (4\text{-}1)$$

$$F(P) = 0.7249 + 0.099 P exp(-0.032P)$$

$$H(P) = -1.159 + 0.149 P exp(-0.019P) + 8.99 P (10 + P^2)^{-1} \qquad (4\text{-}2)$$

The value of the predicted CHF is defined as the maximum value of the two equations.

$$q''_{CHF} = Maximum\left(q''_{B1}, q''_{B2}\right) \qquad (4\text{-}3)$$

Where, q''= critical heat flux (Btu/hr-ft^2)

G = mass flux (g/cm^2-sec)

P = pressure (bars)

D_H = hydraulic diameter (cm)

X = equilibrium quality

n=0.6, if D_H <1.0 cm: n=0.4, if D_H ≥1.0 cm

The values of DNBR at the center of guide tube, water gap and shroud is given any value, 10. The minimum DNBR was found at the assembly corner subchannel and the value was 2.21. If the proper CHF correlation is implemented to CUPID, it is expected to obtain the high precision calculation result of DNBR for safety analysis.

Table 4.3 Operation conditions for Shin Kori unit 3

Parameters	Values
Total thermal power capacity (MWt)	3,983
Pressure (MPa)	15.5
Inlet coolant temperature (K)	564.2
Average mass flux (million kg/h-m^2)	12.6
Inlet coolant velocity (m/s)	2.6

Table 4.4 Input hydraulic diameters for each subchannel type

Subchannel type	Hydraulic diameter (mm)
1	12.64
2	12.64 (near shroud) 17.98 (near water gap)
3	12.64 (near shroud) 24.62 (near water gap)
4	0.13
5	7.65
6	12.71
7	24.62
8	24.62
9	17.98
10	6.21
11	12.42
12	12.42
13	12.42

Table 4.5 Applied subchannel models for Shin Kori unit 3 T/H analysis

	Lateral	Axial	Note
Wall friction		O	Friction factor coefficient Re<2,300 $f = 64 \times Re^{-1.0}$ 2,300<Re<3×10^4 $f = 0.316 \times Re^{-0.25}$ 3×10^4<Re<10^6 $f = 0.184 \times Re^{-0.20}$
Form loss	O		$K_G = 0.5$
Turbulent mixing		O	EV(Equal Volume exchange) Model β = 0.057
Grid spacer		X	

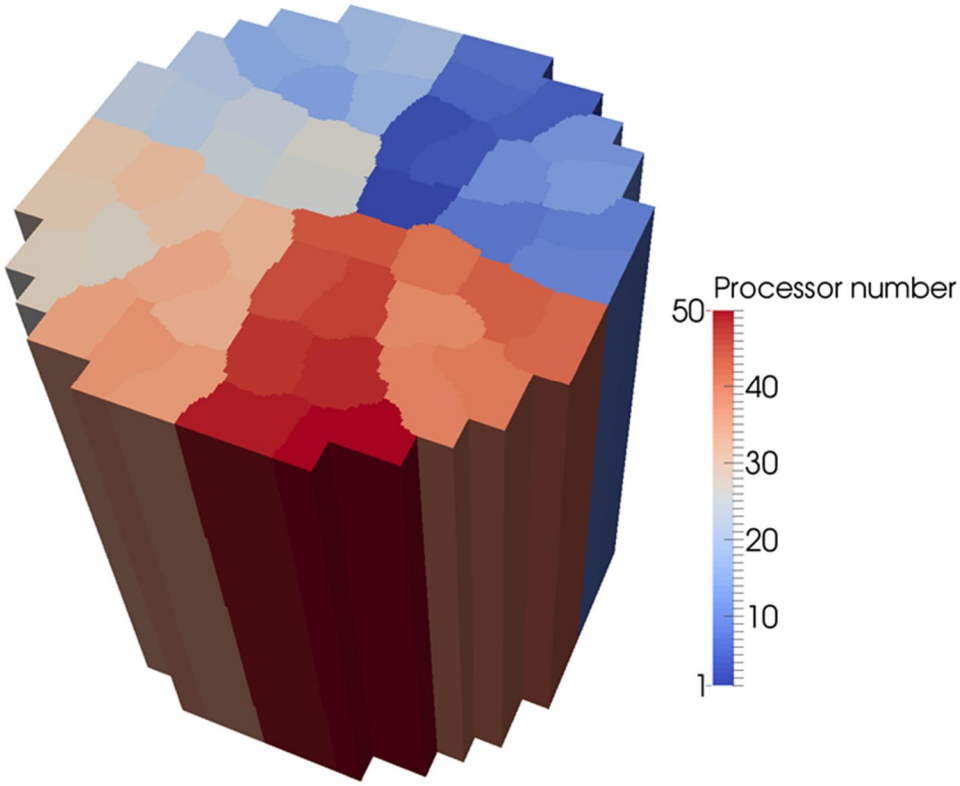

Figure 4.8 Number of computing cells at each processor

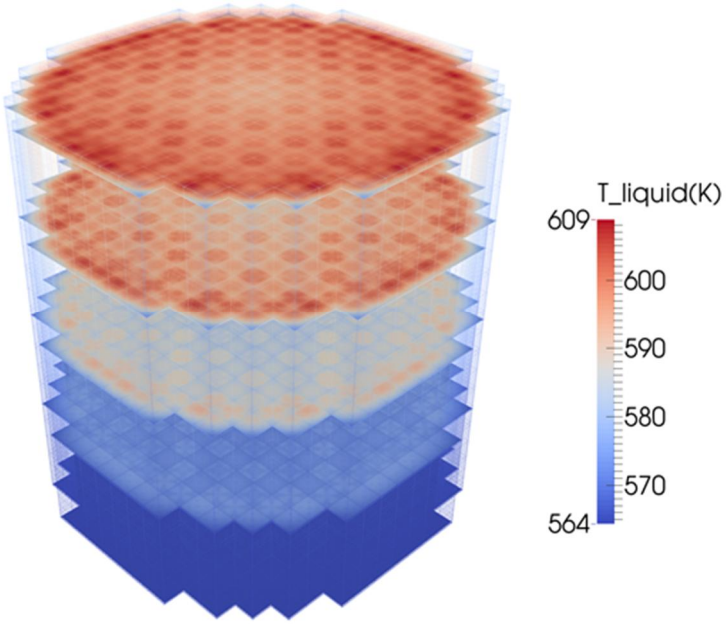

Figure 4.9 Coolant temperature contour map

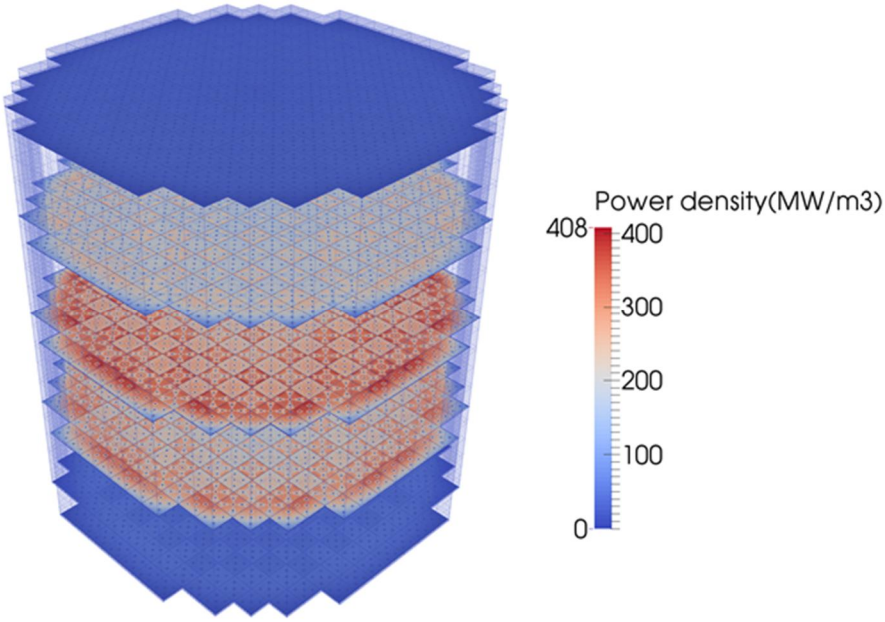

Figure 4.10 Power density contour map

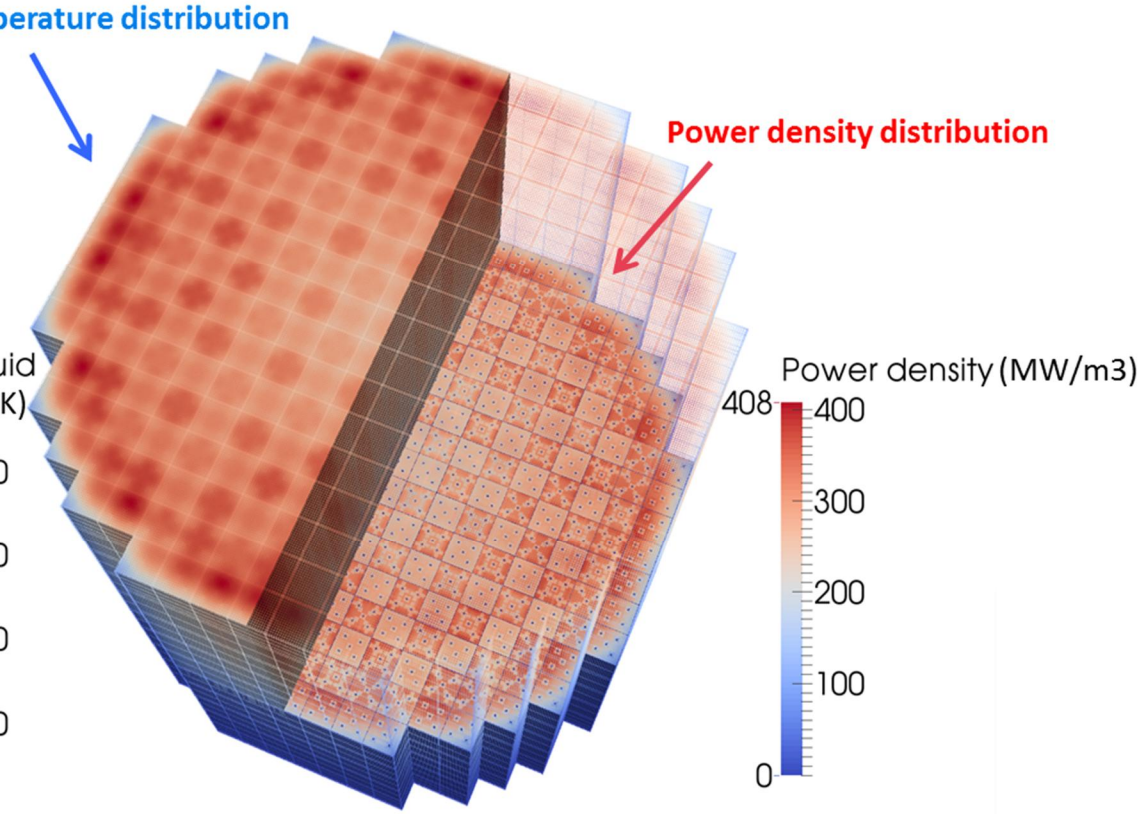

4.11 3D view of coolant temperature (left) and power density distribution (right)

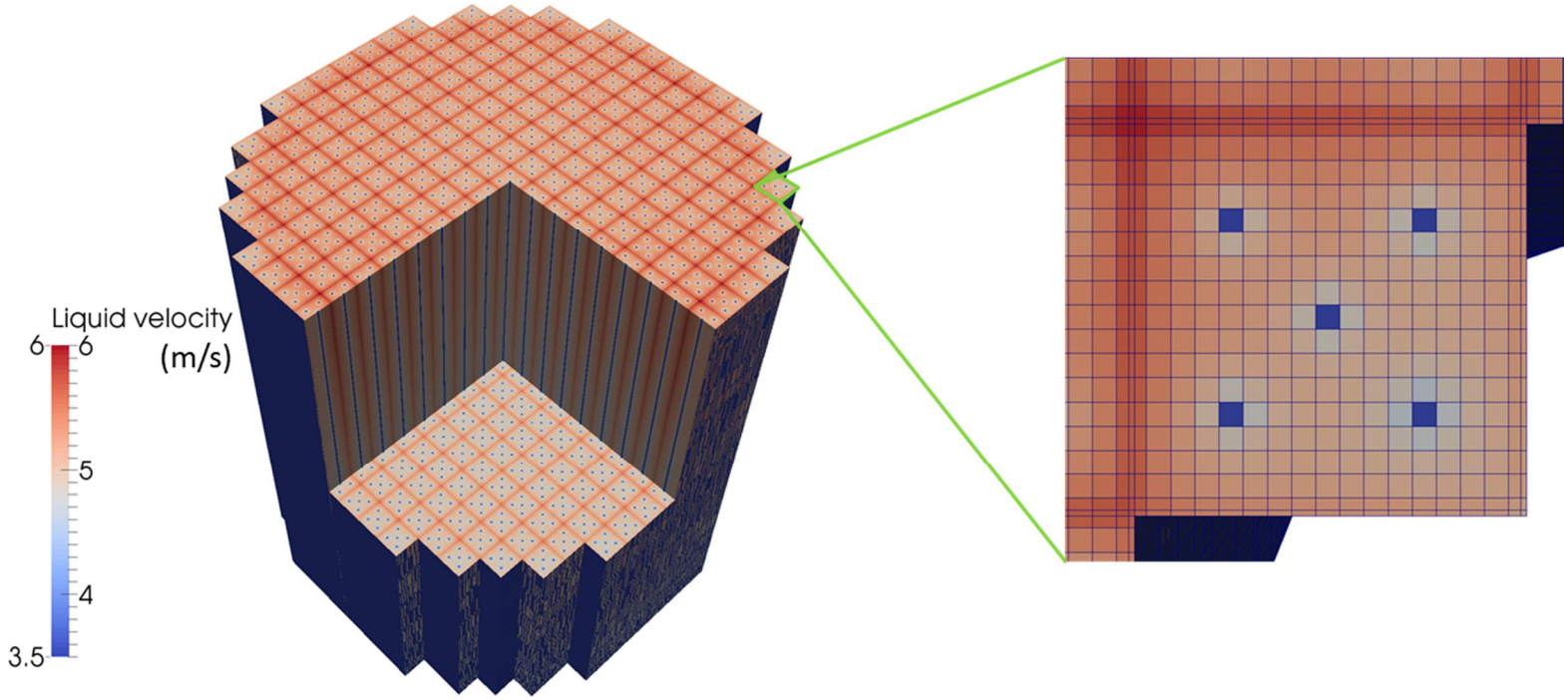

Figure 4.12 3D view of coolant velocity distribution

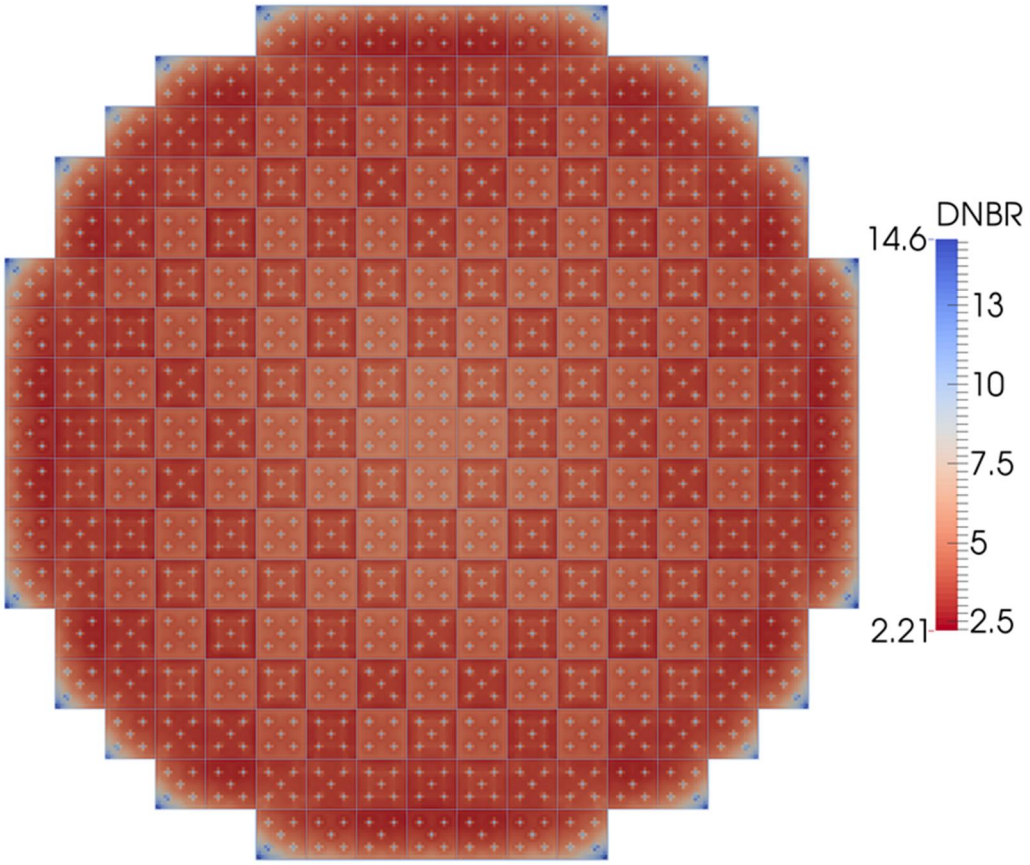

Figure 4.13 DNBR calculation result at middle elevation of full core

Chapter 5.

Conclusions

5.1 Summary

In the present work, the extension of the component thermal hydraulics analysis code CUPID toward subchannel scale analysis of PWR reactor core was introduced. The lists of performed works are summarized as follows:

1. Implementation of subchannel T/H models to CUPID
2. Validation of CUPID subchannel T/H models
3. Subchannel scale full core T/H analysis for APR1400

The convection and pressure drop terms already used in CUPID were considered, but the diffusion terms were neglected and replaced with implemented subchannel models in this calculation. The wall friction and form loss models were added to viscous shear stress term in momentum equation with consideration of flow direction. For the analysis of adiabatic single-phase flow condition, the EM turbulent mixing model was implemented. But, in the case of heated or two-phase flow conditions, the EVVD turbulent mixing model was implemented. The grid spacer was modeled as a form loss considering the flow area change for axial direction.

Thereafter, the CUPID code was validated with nine subchannel tests against various flow conditions. Nine subchannel tests include CNEN 4x4, PNL 7x7, CE 15x15 and WH 14x14 tests against unheated single-phase flow, PNNL 2x6 test against heated single-phase flow, RPI, Van der Ros and Tapuccu tests against unheated two-phase flow and GE 3x3 test against heated two-phase flow. The calculation results of CUPID were compared with the calculation results of MATRA and CTF and the experimental data.

From these validation results, CUPID showed its capability of reproducing key phenomena in a subchannel. In addition, it was revealed that CUPID could handle a reverse flow which cannot be reproduced with spatial marching numerical schemes and simulate the void drift phenomenon properly in two-phase flow condition.

For evaluating a parallel solver performance in CUPID, a preliminary calculation of subchannel scale full core T/H analysis for simplified OPR1000 reactor core was performed. Then, the subchannel scale 3D full core T/H simulation target for APR1400 reactor core was conducted. The core follow demonstration was performed for cycle 1 hot full power steady state of Shin Kori unit 3. For high fidelity T/H simulation of APR1400, all computing cells were characterized into 13 different subchannel types considering the detailed geometry features of assembly, guide tube, shroud and water gap. And then, the required geometry information like porosity, permeability, hydraulic diameter and gap size were input to each of cell following subchannel types. For describing the detailed core power distributions, individual rod power distributions from the calculation results of neutronics code, nTRACER, were applied to CUPID.

The CUPID runs were made on a LINUX cluster each of which uses Dual

Intel® Xeon® E5-2600 CPUs and 50 processors were used for parallel computing. Following the calculation results, the core power distributions, the coolant temperature and velocity distributions were properly simulated with CUPID. In addition, the DNBR was calculated using Biasi correlation and the capability of CUPID to predict the MDNBR was evaluated. From these works, a preliminary calculation for high fidelity full core T/H simulation coupling with CUPID and neutronics code was conducted.

5.2 Recommendations

Even though the subchannel scale simulation capability of CUPID was confirmed, there still exists limitation in high precision calculation for the full core of light water reactor. First of all, it is required to improve or implement the T/H models in the code and more validations against two phase rod bundle tests are needed. Specifically, it is expected to change the flow patterns by influencing of the grid spacer mixing vane, but the grid spacer mixing vane is not yet modeled. Therefore, in the future, it is required to develop the model and implement to the code for high precision T/H calculation. For high fidelity simulation under accident conditions, the implementation of post-CHF model is required, although the pre-CHF model is already implemented to CUPID. Also, the improvement and optimization of parallel solver in CUPID are necessary for high performance of parallel computing.

In this present work, the full core T/H simulation of APR1400 was performed at steady state of normal operation condition. But for evaluating the CUPID code capability of asymmetric power conditions analysis, it is suggested to demonstrate the reactivity induced accidents. In the future, if the calculation is

performed using a coupled CUPID code and neutronics code at the transient of accident conditions, it could deliver higher safety standards and more safety margins for operational needs.

References

Albin G., Schmidt A., Kuhnel K. and Wehle F., “LWR Core Safety Analysis with Areva’s 3-dimensional Methods”, International Journal for Nuclear Power, Vol. 58, pp. 82-87, 2013.

AREVA, The ARCADIA Reactor Analysis System for PWRs Methodology Description and Benchmarking Results, ANP-10297NP, AREVA NP Inc, 2010.

Armand A. A., “The Resistance During the Movement of a Two-phase System in Horizontal Pipes”, translated by V. Beak, AERE Trans 828, 1946.

Basile D., Chierici R., Beghi M., Salina E., Berga E., COBRA-EN, an Updated Version of the COBRA-3C/MIT Code for Thermal-Hydraulic Transient Analysis of Light Water Reactor Fuel Assemblies and Cores, Report 1010/1 (revised 1.9.99), ENEL-CRTN Compartimento di Milano, 2001.

Bates J. M., Khan E. U., Investigation of Combined Free and Forced Convection in a 2x6 Rod Bundle During Controlled Flow Transients, PNL-3135, 1980.

Beus S. G., A Two-Phase Turbulent Mixing Model for Flow in Rod Bundles, Technical Report WAPD-TM-2438, Bettis Atomic Power Laboratory, 1971.

Blyth T. S., Improvement of COBRA-TF Subchannel Thermal-Hydraulics Code (CTF) using Computational Fluid Dynamics, CASL Technical Report, CASL-U-2015-0020-000, 2015.

Biasi L., Clerici G. C., Garribba S., Sala R., Tozzi A., “Studies on Burnout Part 3 - A New

Correlation for Round Ducts and Uniform Heating and Its Comparison with World Data", Energia Nucleare, Vol. 14, pp. 530-536, 1967.

Böer R., Böhm R., Finnemann H., Müller R., "The Coupled Neutronics and Thermal-Hydraulics Code System PANBOX for PWR Safety Analysis", Atomkernenergie (ATKE) 57, pp. 49-54, 1992.

CASL Science & Technology, Departure from Nucleate Boiling (DNB) Multi-Physics Approach & Applications using VERA, www.casl.gov, 2015.

Consortium for Advanced Simulation of Light Water Reactors, www.casl.gov, 2015.

Chelemer H., Chu P. T., Hochreiter L. E., THINC-IV: an Improved Program for Thermal-Hydraulic Analysis of Rod Bundle Cores, WCAP-7956, Westinghouse Electric Corp., 1973.

Creer J. M., Rowe D. S., Bates J. M., Sutey A. M., Effects of Sleeve Blockages on Axial Velocity and Intensity of Turbulence in an Unheated 7x7 Rod Bundle, Pacific Northwest Laboratories, BNWL-1965, 1976.

Daeubler D., Trost N., Jimenez J., Sanchez V., Stieglitz R., Macian J. R., "Static and transient pin-by-pin simulations of a full PWR core with the extended coupled code system DYNSUB", Annals of Nuclear Energy, Vol. 84, pp. 31-44, 2015.

Hwang D. H., Seo K. W., Kwon H., Validation of a Subchannel Analysis Code MATRA Version 1.0, KAERI/TR-3639/2008, KAERI, 2008.

Jeong J. J., Hwang D. H., Bae S. W., Chung B. D., "Assessment of the Inter-channel

Mixing Model of the MARS Code", Transactions of the Korean Nuclear Society Autumn Meeting, 2005.
Jimenez J., Trost N., Sanchez V., KIT activities using CTF within NURESAFE project, 1st CTF User group meeting, 2014.

Jiménez J., Cuervo D., Aragonés J. M., "A domain decomposition methodology for pin by pin coupled neutronic and thermal–hydraulic analyses in COBAYA3", Nuclear Engineering and Design, Vol. 240, pp. 313-320, 2010.

Jung Y. S., Shim C. B., Lim C. H., Joo H. G., "Practical numerical reactor employing direct whole core neutron transport and subchannel thermal/hydraulic solvers", Annals of Nuclear Energy, Vol. 62, pp. 357-374, 2013.

Karypis G., Kumar V., "Multilevel k-way Partitioning Scheme for Irregular Graphs", J. Parallel Distrib. Comput. Vol. 48, pp. 96-129, 1998.

Kim S. J., Hwang D. H., Kwon H., "Parallelization of Subchannel Analysis Code MATRA", Proceedings of the KNS 2014 spring meeting, 2014.

Kim H. R., Kim S. H., Lee S. J., Park I. K., Yoon H. Y., Cho H. K., Jeong J. J., "Development of CUPID-SG for the analysis of two-phase flows in PWR steam generators", Progress in Nuclear Energy, Vol. 77, pp. 132-140, 2014.

Korea Atomic Energy Research Institute, CUPID Code Manuals Vol. 1: Mathematical Models and Solution Methods Version 1.9, 2014.

Korea Atomic Energy Research Institute, MARS code manual. Models and Correlations Vol. 5, 2009.

Korea Atomic Energy Research Institute, SPACE code manual models and correlations, 2011.

Kwon H., Hwang D. H., Seo K. W., Kim S. J., Park J. P., Validation of a Subchannel Analysis Code MATRA Version 1.1, Korea Atomic Energy Research Institute, KAERI/TR-5581/2014, 2014.

Lahey R. T., Moody F. J., The Thermal-Hydraulics of a Boiling Water Nuclear Reactor 2nd edition, American Nuclear Society, La Grange Park, 1993.

Lahey R. T., Moody F. J., The Thermal-Hydraulics of a Boiling Water Nuclear Reactor, Technical report, ANS Monograph, 1977.

Lahey R. T. Jr., Shiralkar B. S., Radcliffe D. W., Two-phase flow and heat transfer in multirod geometries: subchannel and pressure drop measurements in a nine-rod bundle for diabatic and adiabatic conditions, GEAP-13049, General Electric, 1970.

Lee J. R., Cho H. K., Jeong J. J., "Coupled Simulation of Component Thermal Hydraulics and Neutron Kinetics for a Nuclear Reactor Core with CUPID and MASTER", Transactions of the Korean Nuclear Society Autumn Meeting, 2010.

Marinelli V., Pastori L., Kjellen B., "Experimental Investigation of Mass Velocity Distribution and Velocity Profiles in an LWR Rod Bundle", Trans. ANS 15, pp 413-415, 1972.

Marshall R. C., Letendre R. P., "Influence of Inlet Geometry on Flow in the Entrance

Region of a Nuclear Reactor Rod Bundle", ASME, 68-WA/HT-34, pp.1-8, 1969.

Nuclear Reactor Safety simulation platform, www.nuresafe.eu, 2012.

Pang B., Numerical study of void drift in rod bundle with subchannel and CFD codes, Karlsruher Institut für Technologie, KIT-SR 7669, 2014.

Park I. K., Lee J. R., Lee S. W., Yoon H. Y., "A simulation of the coolant mixing using the coupled MARS CUPID", Transactions of the Korean Nuclear Society Autumn Meeting, 2012.

Rogers J. T., Rosehart R. G., "Mixing by Turbulent Interchange in Fuel Bundles. Correlations and Influences", ASME, pp. 1-12, 1972.

Salko R., Lange T., Kucukboyaci V., Sung Y., Palmtag S., Gehin J., Avramova M., Development of COBRA-TF for Modeling Full-core, Reactor Operating Cycles, CASL Technical Report, CASL-U-2015-0133-000, 2015.

Salko R., Avramova M., CTF Theory Manual, Pennsylvania State University, 2014.

Sanchez V., Imke U., Ivanov A., Gomez R., SUBCHANFLOW: a thermal-hydraulic subchannel program to analyse fuel rod bundles and reactor cores, Proceedings of the 17th Pacific Basin Nuclear Conference, 2010.

Sterner R. W., Lahey R. T. Jr., Air-Water Subchannel Measurements of the Equilibrium Quality and Mass Flux Distribution in a Rod Bundle, NUREG/CR-3373, 1983.

Tapucu A., Teyssedou A., Tye P., Troche N., "The effect of turbulent mixing models on

the predictions of subchannel codes", Nuclear Engineering and Design, Vol. 149, pp. 221-231, 1994.

Todreas N. E., Kazimi M. S., Nuclear Systems Ⅱ, Elements of Thermal Hydraulic Design, chap 6, Taylor & Francis, 1990.

Tomiyama A., Tamai H., Zun I., Hosokawa S., "Transverse migration of single bubbles in simple shear flows", Chemical Engineering Science, Vol. 57, pp. 1849-1858, 2002.

Van der Ros T., On two-phase flow exchange between interacting hydraulic channels, PhD thesis, Eindhoven University of Technology, 1970.

Wallis G. B., One-Dimensional Two-Phase Flow, McGraw-Hill, 1969.

Wheeler C. L., Stewart C. W., Cena R. J., Rowe D. S., Sutey A. M., COBRA-IV-I: An Interim Version of COBRA for Thermal Hydraulic Analysis of Rod Bundle Nuclear Fuel Elements and Cores, BNWL-1962, Pacific Northwest Laboratory, 1976.

국문초록

최근, 반응도 유발 사고에 대한 노심 내 정밀한 해석을 위해 열수력 해석 코드와 노물리 해석 코드를 연계한 다물리 해석을 통해 전노심에 대한 고정밀 열수력 해석이 중요한 이슈가 되고 있다. 노심에 대한 해석 방법으로 해의 정확성을 보장하며 합리적인 계산시간을 갖는 부수로 스케일 해석 방법이 요구된다. 본 연구에서는 한국원자력연구원에서 개발 중인 3 차원 2 상유동 기기스케일 열수력 해석 코드 CUPID 의 적용범위를 확장하여 원자로 노심 부수로 스케일 해석에 적용하였다. CUPID 코드는 MPI domain decomposition 방법으로 고효율적으로 병렬화 되어있어 수백만 개의 격자수를 갖는 전 노심에 대한 효율적인 계산이 가능하다.

본 연구에서는 CUPID 의 부수로 스케일 해석을 위해 부수로 열수력 모델인 교차류 모델, 동일 질량 교환 모델, 동일 체적 교환 및 기포 이동 모델, 지지격자 모델을 코드에 대입하였다.

대입된 부수로 모델에 대한 검증을 위해 비가열 단상 유동 조건의 실험 4 개, 가열 단상 유동 조건의 실험 1 개, 비가열 2 상 유동 조건의 실험 3 개, 가열 2 상 유동 조건의 실험 1 개에 대하여 코드 검증을 수행하였다. 검증은 실험 결과 및 부수로 해석코드 MATRA, CTF 계산 결과와 비교 검증 하였다. 검증 결과, 집합체 부수로 내에서 발생하는 핵심 현상들에 대해 코드가 적절하게 예측할 수 있었다.

단순화된 OPR1000 원자로에 대한 개념문제 해석을 통해 CUPID 코드의 병렬처리성능을 확인하였고 차세대 한국형 원전인 APR1400 의 부수로 스케일 전 노심 열수력 해석을 수행하였다. 구체적인 노심 형상 정보를 고려하였고 노물리 해석코드 nTRACER 의 봉별 출력 분포를 코드에 대입하여 신고리

3 호기 1 주기 초기노심에 대한 해석을 수행하였다. 해석 결과, 코사인 함수 형태의 출력 분포가 코드에 적절히 반영되었고 이에 따른 노심 내 온도 분포 및 속도 분포 형상을 합리적으로 계산하였다. 또한, Biasi 상관식을 통한 DNBR 계산을 수행하였고 전 노심에 대한 DNBR 값이 CUPID 코드를 통해 계산 가능하다는 것을 확인하였다.

주요어:
부수로 스케일 열수력 해석, 노심 열수력 해석, CUPID, 코드 검증, APR1400

학번: 2015-21325